University of Zurich[UZH]

Determining the englacial temperature evolution of very small glaciers in the Swiss Alps: An enthalpy-based modelling approach

ESS 510 Master's Thesis

Author
Janosch Philip Beer
21-738-166

Supervised by
Prof. Dr. Andreas Vieli
Dr. Mylène Jacquemart (jacquemart@vaw.baug.ethz.ch)
Dr. Matthias Huss (huss@vaw.baug.ethz.ch)

Faculty representative
Prof. Dr. Andreas Vieli

22.12.2023
Department of Geography, University of Zurich

Acknowledgements

First, I would like to express my sincere gratitude to my supervisor Dr. Mylène Jacquemart for her guidance through each stage of the process of writing and preparing this thesis. She demonstrated remarkable flexibility and understanding, despite being on maternity leave after recently becoming a mother. I am very grateful for that. Furthermore, she consistently allowed this thesis to be my own work, but steered me in the right direction whenever she thought I needed it. In addition, I would like to thank Prof. Andreas Vieli for his invaluable guidance throughout this study and his extensive expertise in various glaciological processes crucial to be considered in glacier modeling. Additionally, I extend my gratitude to Dr. Ivan Utkin, whose substantial contributions were integral to the development of the model. Without his expertise and assistance, the creation of this new ice temperature model, especially in addressing Julia-related inquiries, would not have been achievable. Furthermore, I would like to thank Dr. Matthias Huss, whose profound expertise in glacier modeling was invaluable throughout the entire model development process. Finally, I extend my heartfelt thanks to my girlfriend, Dominika Teluchová, for her unwavering support throughout the duration of this year-long thesis.

Abstract

Despite constituting 80% of the total number of glaciers in mid- to low-mountain range catchments, the attention paid to very small glaciers (< 0.5 km^2) in glacier research remains relatively low. However, glaciers of this size category are expected to undergo dramatic changes. Within Switzerland, more than half are predicted to disappear within the next two decades. As these glaciers shrink, they lose their firn cover, a crucial latent heat source through refreezing meltwater. Simultaneously, reduced glacier dynamics result in less ice deformation and decreased frictional heating at the base. Various studies suggest that such conditions can promote cooling, possibly enabling a transition from temperate to polythermal or cold states (Gilbert et al. 2012; Signer 2014; Huss and Fischer 2016). Polythermal glaciers, especially those with partly frozen glacier beds, have been found to accumulate excessive meltwater, resulting in glacier instabilities (Pralong and Funk 2006; Irvine-Fynn et al. 2011) or glacier lake outburst floods (GLOFS) (Huggel et al. 2004; Vincent et al. 2012). This calls for a reevaluation of the thermal state of very small glaciers within Switzerland. In this study a new enthalpy-based englacial temperature model (IceT) is presented and used to investigate the potential transition of very small Swiss glaciers from temperate to polythermal or cold conditions. The study focuses on identifying key parameters influencing glacier thermal transitions through a sensitivity analysis. Furthermore, a reassessment of the thermal state of Swiss glaciers takes place using IceT and previously generated model results of the Glacier Evolution Runoff Model (GERM). The mass balance and the englacial water content emerged as the most crucial factors for predicting glacier thermal states. The influence of mass balance works in two ways: (1) Highly negative mass balances hinder the development of a polythermal structure by allowing surface melt to surpass the propagation of the cold-temperate transition surface (CTS). (2) Less negative mass balances combined with limited snowfall induce a transition to polythermal conditions by enabling the CTS propagation to outpace surface melt. Ultimately, the englacial water content (ϕ) appears as the most critical parameter in predicting ice temperatures. A mere increase of ϕ by 1% could reduce the maximum CTS depth by 165.07 m and lower the annual CTS propagation rate by 13.85 m a^{-1}. Significant differences emerge between GERM and IceT findings. GERM suggests that over 75% of all very small Swiss glaciers exhibit polythermal conditions, while in the subset of 20 glaciers modeled with IceT, only 15% show indications of polythermal conditions in their ice temperature distribution. However, the considerable impact of englacial water on predicting ice temperatures, coupled with the incomplete knowledge regarding its distribution within glaciers, leads to substantial uncertainties in the presented model outcomes.

Keywords— Very small glaciers, ice temperatures, glacier thermal regime, glacial hazards, glacier instabilities, climate change

Contents

1 Introduction **1**

2 Methods & Data **3**

2.1 IceT, a new 1-dimensional ice temperature model . . . 3

2.1.1 An enthalpy formulation to model englacial temperatures . . . 3

2.1.2 Surface energy balance model . . . 6

2.1.3 Mass balance . . . 11

2.1.4 CTS tracking . . . 12

2.1.5 Numerical methods & model mesh . . . 12

2.2 GERM . . . 13

2.2.1 Mass balance . . . 14

2.2.2 Glacier geometry . . . 15

2.2.3 Englacial temperatures . . . 15

2.3 Model calibration . . . 16

2.4 Parametric study . . . 20

2.4.1 Surface energy budget . . . 21

2.4.2 Snowfall . . . 24

2.4.3 Water volume fraction (ϕ) . . . 26

2.4.4 Tested output variables . . . 27

2.5 Applications on very small Swiss glaciers . . . 27

2.5.1 GERM geostatistical reanalysis . . . 28

2.5.2 IceT . . . 28

3 Results **30**

3.1 Parametric study . . . 30

3.1.1 Full parametric analysis . . . 30

3.1.2 Parameter space slicing . . . 34

3.2 Applications on very small Swiss glaciers . . . 40

3.2.1 GERM geostatistical reanalysis . . . 41

3.2.2 IceT . . . 44

3.2.3 Comparison to measured borehole temperatures . . . 50

4 Discussion **52**

4.1 Model uncertainties . . . 52

4.2 Sensitivities of very small Alpine glaciers to thermal regime changes . . . 54

4.2.1 Surface energy budget . . . 54

4.2.2 Snow & mass balance . . . 55

4.2.3 Water content (ϕ) . . . 55

4.3 The thermal evolution of very small Swiss glaciers 56
4.3.1 Model comparison 56
4.3.2 Spatio-temporal scales of glacier thermal regime transitions 57

5 Conclusion & Outlook **58**

List of Figures

1 Schematic overview of IceT (A) as well as the thermodynamic look-up table used to invert ice temperatures (B) as well as the water volume fraction (C) from internal energy (D). 3

2 Annual cycle of the 3 shortwave radiation model components (A) cos(Z), (B) ψ, (C) δ and the resulting incoming shortwave radiation (D) $E_S\downarrow$ given the parametric setting in table (2). 8

3 Modeled annual shortwave radiation cycle. The gray line depicts the per-timestep computed radiation, containing daily fluctuations. The dashed black line depicts the averaged daily radiation. 9

4 Mean annual climatological irradiance for several sites in Switzerland (reference period 1993-2013), used for approximation of the transmissivity parameter ψ_0 within IceT's shortwave radiation model. The blue dots depict daily average values for the year 2014, the red line the monthly averages for 2014, whereas the black line depicts the monthly climatological average (MeteoSwiss 2023). 10

5 Framework used to model the insulation of the snow cover within GERM. $th0$ represents the lower threshold and $th1$ the upper threshold, while asc abbreviates the actual snow cover. (a) Scenario where asc > th0, (b) scenario where th0 < asc < th1 and linear interpolation between the air temperature and 0 Illustration drawn from Signer (2014). 16

6 Mass balance comparison of GERM (dashed) against IceT (solid) for Glacier du Sex Rouge. (A) Winter and summer mass balance. (B) Net annual mass balance. 18

7 Mass balance comparison of GERM (dashed) against IceT (solid) for Vadret dal Corvatsch. (A) Winter and summer mass balance. (B) Net annual mass balance. 19

8 Least-squares sine fitting results based on 9 year air temperature records (2014-2022) for (A) Les Diablerets, (B) Piz Martegnas (2670 MASL), (C) Gornergrat (2950 MASL), (D) Titlis (3040 MASL), (E) Jungfraujoch (3571 MASL) and (F) Piz Corvatsch (3294 MASL). 22

9 (A) Lapse-rate approximation for the Swiss Alps based on linear fitting of mean annual air temperatures (Reference period 2014-2022) for several Swiss weather stations. Jungfraujoch (JUN), Piz Corvatsch (COV), Titlis (TIT), Gornergrat (SLFGOR), Eggishorn (EGH), Les Attelas (ATT), Weissfluhjoch (WFJ), Piz Martegnas (PMA), Gütsch (GUE), Buffalora (BUF), Matro (MTR), Samedan (SAM), Le Moléson (MLS), Zermatt (ZER), Blatten, Lötschental (BLA). (B) MAAT at discrete elevation levels resulting from the linear model. 23

10 Default annual air temperature curve based on sinusoidal model, applying a MAAT of -5.5°C and an amplitude of A = 16°C. 24

11 Switzerland's mean annual snow water equivalent (1961-2017) based on MeteoSwiss gridded precipitation and air temperature data (MeteoSwiss 2014a; MeteoSwiss 2014b). Precipitation was counted as snow only when air temperatures dropped below 0°C. 25
12 Annual snowfall resulting from the default parametric settings with a total snow accumulation volume of 0.5 m SWE and assuming a total number of 250 snowfall days. 26
13 Correlation matrix depicting all cross correlations between the 7 parameters, the net annual mass balance, as well as the 3 output variables CTS_{max},CTS_{prop} and $T_{10m,min}$. The parameters are structured according their type: $MAAT$ and α_s (Surface Energy Budget), P_s,σ,$t_{0,s}$,f_z (Snow),ϕ_0 (Water volume fraction). 31
14 Modeled glacier profile evolution plotted against time using the default parametric setting as prescribed in table 4. (A) Ice temperature evolution, (B) Water volume fraction ϕ together with the approximate location of the CTS, (C) Glacier state. . . . 35
15 Modeled glacier profile evolution plotted against time using the default parametric setting as prescribed in table 4. (A) Ice temperature evolution, (B) Water volume fraction ϕ together with the approximate location of the CTS, (C) Glacier state. The profile further represents scenario 3 depcited in figure 16. 36
16 Heatmaps colored according to the maximum depth of the CTS as well as the annual CTS propagation rate for the parameter range of the total annual snowfall (P_s) against the water volume fraction ϕ_0. Each square represents the results for one individual model run applying the given parametric combination, while all other parameters are drawn from the default parametric setting (Tab. 4). S1-S3 mark exemplary selected scenarios to further illustrate their ice temperature evolution and can be seen in figure 17,18. S1 represents the parametric combination of the default scenario plotted in 14. 37
17 Modeled ice temperature evolution for the parametric settings S1 depicted in figure 16, with high snowfall (2.0 m w.e. a^{-1}) and low water content (1%). 38
18 Modeled ice temperature evolution for the parametric settings S2 depicted in figure 16, with high snowfall (2.0 m w.e. a^{-1}) and high water content (5%). Note the evident mitigation of cooling within the glacier owing to the increased englacial water content. 39
19 Heatmaps colored according to the maximum depth of the CTS as well as the annual CTS propagation rate for the two parameters controlling the surface energy budget, the mean annual air temperature (A,B) and snow albedo (C,D). Each square represents the results for one individual model run applying the given parametric combination, while all other parameters are drawn from the default parametric setting (Tab. 4). Displayed are the results for 40

20 (A) Swiss map displaying the locations of all very small glaciers (< 0.5 km^2) as small blue dots. (B) Pie charts displaying the results of the geostatistical analysis of all glaciers clustered for aspect, slope and elevation. Displayed are the relative percentage as well as the number of glaciers contained within each cluster. The analysis is based on the 2016 Swiss glacier inventory (Linsbauer et al. 2021). 41
21 Modeled 10 meter ice temperatures with GERM from 1961-2014. Time series represents averages of (A) all very small glaciers (< 0.5 km^2) within the Swiss Alps for the ablation, ELA and accumulation point, (B) averages plotted for different glacier orientations, (C) averages for different glacier slopes and (D) averages for different glacier elevations. 43
22 Modeled 10 m ice temperature with GERM. Box-plots display snapshots in time for 1980, 1990 and 2000 in the ablation area and at the ELA. 44
23 The maximum CTS depth, CTS_{max}, derived from ice temperature modeling for a subset of 20 very small glaciers (< 0.5 km^2). The glaciers have been categorized into three groups (high,medium,low) using k-means clustering and are sorted based on their CTS_{max} values to demonstrate their ranking. 45
24 Swiss map displaying IceT model outcomes for a subset of 20 very small glaciers (< 0.5 km^2) utilizing the meteorological dataset of Huss and Fischer (2016). The map displays the locations of all very small glaciers (small blue dots) and the modeled glaciers (larger dots), shaded in turquoise to represent the maximum CTS depth achieved during the modeling process. Additionally, the names of the modeled glaciers, their respective maximum CTS depth values (turquoise), and the normalized CTS value $n(CTS)$ (grey) are provided. 46
25 Modeled ice temperatures at different depths for Vadret dal Corvatsch. Modelling results of IceT (A), Model results of GERM for the ELA point (B), modeled snow depth using IceT (C), cummulative mass balances of the two models plotted against each other (D). Please note the distinct y-axis limits between IceT and GERM. 47
26 Modeled ice temperatures at different depths for Vadret da l'alp Ota. Modelling results of IceT (A), Model results of GERM for the ELA point (B), modeled snow depth using IceT (C), cummulative mass balances of the two models plotted against each other (D). Please note the distinct y-axis limits between IceT and GERM. 48
27 Modeled ice temperatures at different depths for Chessjengletscher SE. Modelling results of IceT (A), Model results of GERM for the ELA point (B), modeled snow depth using IceT (C), cummulative mass balances of the two models plotted against each other (D). Please note the distinct y-axis limits between IceT and GERM. 49
28 Correlation analysis of glacier characteristics and their influence on the maximum depth of the CTS: Mean annual snowfall (A), Average number of snowfall days (B), Mean annual air temperature (C), Elevation above sea level (D). 50

29 Locations of borehole measurements for (A) Vadret dal Corvatsch by Hager (2002) as well as (B) Glacier du Sex Rouge and (C) St.Annafirn conducted by Signer (2014). . . 51
30 Results of borehole ice temperature measurements for different times for (A) Vadret dal Corvatsch (borehole 5) , (B) Glacier du Sex Rouge (borehole 1 in blue, borehole 2 in green) and (C) St.Annafirn (borehole 6 in red and borehole 9 in blue). 51
31 IceT model results for (A) Vadret dal Corvatsch , (B) Glacier du Sex Rouge and (C) St.Annafirn. All three glaciers depict clear temperate conditions. The bending of the temperature curve towards slightly negative temperatures can be interpreted as a remnant of the last cooling period. 52

List of Tables

1 Physical constants for ice and water used as basis for the englacial temperature model. 6
2 Physical constants used within the radiation model. 11
3 Default model dimensions 13
4 Parametric settings used within the parameter study. Depicted are the default values as well as the ranges applied. The different parameters are subdivided into three groups, those affecting the surface energy budget, the snowfall and the water volume fraction. 27
5 Overview of modeled glaciers with IceT. The hazardous record for the individual glaciers is based on the inventory of dangerous glaciers (Raymond et al. 2003). . . . 29
6 Regression Coefficients and Statistics for the prediction of the maximum CTS depth CTS_{max} for $MAAT$, α, P_s, f_z,ϕ and mb. 33
7 Regression Coefficients and Statistics for the prediction of the annual CTS propagation rate CTS_{prop} for $MAAT$, α, P_s, ϕ and mb 34

1 Introduction

Glaciological research within the Alps focuses predominantly on medium to large valley glaciers. However, very small glaciers (here defined as < 0.5 km^2 after Huss and Fischer 2016) account for more than 80% of the total number of glaciers of mid- to low mountain range catchments (Paul et al. 2004; Maussion et al. 2022). Moreover, the accelerated global glacier mass loss observed in the 21st century (Hugonnet et al. 2021) has led to the fragmentation of numerous large valley glaciers, resulting in a net increase in the number of small glaciers. Using a lower area cut-off of 0.01 km^2 a total number of 1573 glaciers of this size category can be counted using the current Swiss glacier inventory (Linsbauer et al. 2021). In contrast to large valley glaciers, small glaciers undergo a much more rapid response to climatic warming. As a consequence, it is estimated that within Switzerland more than half of these dwarf glaciers may completely disappear within the next two decades (Huss and Fischer 2016).

Many of these very small glaciers feature equilibrium line altitudes significantly higher than the glacier's elevation, resulting in the absence of an intact accumulation area. Consequently, they lose their firn cover along with the associated latent heat source generated by refreezing meltwater. Furthermore, the reduction in size is accompanied by a loss of glacier dynamics, which represents an additional source of heat. Several studies have demonstrated that such a setting can result in a cooling of the glacier, eventually inducing a transition from temperate to polythermal conditions (Gilbert et al. 2012; Signer 2014; Huss and Fischer 2016). Polythermal glaciers, particularly those characterised by an ablation area that is frozen to its bed, have been found to accumulate meltwater volumes in excess of the drainage capacity of the hydrological system (Kavanaugh and Clarke 2001; Irvine-Fynn et al. 2011). Such settings have been found to substantially increase the hazard potential of these glaciers, leading to glacier instabilities (Pralong and Funk 2006; Irvine-Fynn et al. 2011) or triggering glacier lake outburst floods (GLOFS) (Röthlisberger 1981; Huggel et al. 2004; Vincent et al. 2012). The tragic occurrence of an ice avalanche at the Marmolada glacier in the Dolomites with 11 casualties, has recently renewed attention to this subject (Bondesan and Francese 2023). Switzerland has a long history of natural disasters caused by glaciers (Huggel et al. 2004; Pralong and Funk 2006; Faillettaz et al. 2015). The mechanisms behind these glacier instabilities are numerous. For avalanching glaciers such as Marmolada, Faillettaz et al. 2015 have proposed a categorisation into three distinct types, all originating from differences in the basal properties: (1) Glaciers with an entirely frozen bed, with instabilities resulting from progressive increase of internal damage due to changes in the glacier geometry. (2) Glaciers exhibiting partial thawing at their base and featuring a temperate zone. In such scenarios, the eventual rupture occurs directly on the bedrock within the temperate region. (3) Steep glacier tongues in temperate conditions prone to sliding along their bedrock. In this scenario, the ultimate rupture takes place directly at the bedrock. All three mechanisms are related to the glacier thermal regime with type 1 and 2 depending on the emergence of a distinct polythermal structure. Moreover, even in the context of large valley glaciers, ice temperatures have been found to be an important factor in explaining glacier collapses (Gilbert

et al. 2015; Kääb et al. 2021). The most notable incident was the twin glacier collapse within the Aru Range in Tibet. This event was characterized by a cold-based plug situated in front of a temperate zone, which caused an elevation in pore water pressure within the subglacial drainage system, triggering an ice avalanche estimated at 83 $\times 10^6$ m^3 (Gilbert et al. 2015). In case of Tête Rousse glacier, a similar polythermal structure has caused an increase of the hydrostatic pressure in excess of the ice pressure at the glacier base (Vincent et al. 2012). Although Tête Rousse could undergo artificial drainage, this subglacial overpressure is believed to have triggered the collapse of the Marmolada glacier in July 2022 (Bondesan and Francese 2023). However, it is important to note that unlike Tête Rousse and Marmolada, which are directly situated on bedrock, the two Aru glaciers are located on softer sedimentary beds. Failure occurred within these sedimentary layers (Gilbert et al. 2018), whereas for Marmolada the precise mechanisms are not yet known. Even though glacial hazards resulting from polythermal settings are still rare, the rapid climatic changes induced on very small Swiss glaciers may elevate the count of previously presumed temperate glaciers transitioning to polythermal conditions. With a total of 1131 very small Swiss glaciers and their numbers steadily rising, statistically, Switzerland stands as the most susceptible alpine country to such glacial hazards. This underscores the significance of reevaluating the thermal status of very small glaciers within the Swiss Alps.

This study examines the englacial temperature evolution of very small glaciers within Switzerland and thereby aims on answering the following 2 research questions:

1. Under which conditions do very small alpine glaciers transition from temperate to polythermal or cold conditions?
   (a) Which parameters determine these thermal transitions?
   (b) At what speed and at what spatial scales do these thermal transitions occur?
2. Which very small glaciers (< 0.5 km^2) within the Swiss Alps exhibit transitions from temperate to polythermal or cold states, and how can these transitions be identified?

To achieve this, a novel enthalpy-based model (IceT) is created, allowing for the concurrent tracking of ice, air, and water within the glacier. This capability is crucial in capturing the intricate thermodynamic processes governing the ice temperature evolution. Two distinct approaches are outlined to assess the transition of small glaciers from temperate to polythermal or cold conditions. The first approach aims to identify the parameters influencing thermal regime transitions and evaluates the spatio-temporal scales of these transitions. The second approach focuses on realistically assessing the thermal state of small glaciers in the Swiss Alps, utilizing previously generated model results from GERM (Huss and Fischer 2016) and implementing the new enthalpy-based model. This study deliberately concentrates on small glaciers due to their heightened susceptibility to exhibit thermal regime changes, driven by the loss in glacier dynamics and the reduced firn cover thickness.

2 Methods & Data

2.1 IceT, a new 1-dimensional ice temperature model

This study presents a new 1-dimensional enthalpy-based ice temperature model (IceT), which allows for the simultaneous tracking of ice, water and air within each grid cell. On the basis of fundamental thermodynamic principles, ice temperatures and liquid water content are inverted from internal energy. The model is composed of several components, including (1) a fully coupled surface energy balance model that resolves surface energy exchange, (2) a mass balance component to track both accumulation and ablation at the glacier surface, and (3) continuous monitoring of the cold-temperate transition surface (CTS) to assess the thermal state of the ice column. A schematic representation of the model has been crafted (refer to figure 1), showcasing the various factors influencing the surface energy flux. The graphic features the delineation of the CTS and elaborates on the coexistence of ice, water and air within each model grid cell. Furthermore, the figure provides an overview of the thermodynamic look-up table employed to invert englacial temperatures and water volume fraction from internal energy.

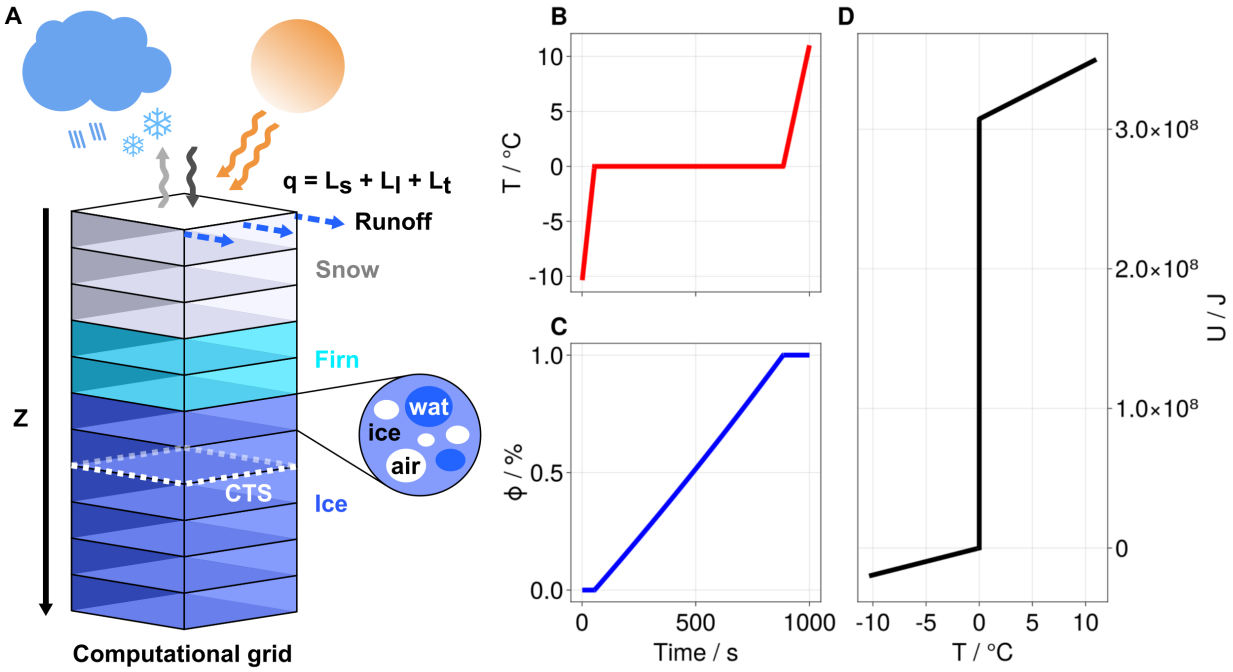

Figure 1: Schematic overview of IceT (A) as well as the thermodynamic look-up table used to invert ice temperatures (B) as well as the water volume fraction (C) from internal energy (D).

The various components of the model will be further elaborated on within the following sections.

2.1.1 An enthalpy formulation to model englacial temperatures

Polythermal glaciers are characterised by a mixed thermal regime, containing both cold ice (temperature below the pressure-melting point PMP) and temperate ice (temperature at the PMP) (Benn and Evans 2014). As geophysical phase-transitions are inevitable, this leads to a thermal

problem. While the cold domain is expected to be solid, the temperate domain is characterised by a solid/liquid mixture. Englacial temperatures, as well as the relative fraction of liquid water, define physical properties such as e.g. the viscosity of the ice. This results in a thermomechanically coupled and polythermal flow problem (Aschwanden et al. 2012). Conventional so-called "cold-ice" models use differential equations for temperature to ensure energy balance (Payne et al. 2000; Bueler et al. 2007). However, Aschwanden et al. (2012) stressed the disadvantages of such models as they do not account for the full energy content of temperate ice where phase transitions between solid and liquid fractions occur. The englacial temperature model developed in the framework of this thesis is based on an enthalpy formulation proposed by Aschwanden et al. (2012), derived from the fundamental principles of conservation of energy and conservation of mass. In the following, the different steps to derive the enthalpy for solid/liquid water mixtures will be described.

Assuming a mixture of ice and water with partial densities ρ_i and ρ_w (mass per unit volume of the mixture). The mixture density is the sum

$$\rho = \rho_i + \rho_w \tag{1}$$

The liquid water fraction or water content, is the ratio

$$\phi = \frac{\rho_w}{\rho} \tag{2}$$

The barycentric (mixture) velocity, v, is defined by

$$\rho v = \rho_i v_i + \rho_w v_w \tag{3}$$

There are significant differences in the bulk densitites of ice ($\hat{\rho_i} = 920$ kg m^{-3}) and water ($\hat{\rho_w} = 1000$ kg m^{-3}). However, liquid water fractions within temperate ice are expected to be in the order of ≤ 5 % and thus changes in mixture density which correspond to changes in liquid water fraction are in the order of ≤ 0.5 %. For this reason, the mixture of solid and liquid water is treated as incompressible ($\rho \approx \hat{\rho_i}$). Furthermore, thermodynamic equilibrium is assumed within the given modelling framework, thus the absolute temperature and internal energy of the solid/liquid mixture are well defined (Aschwanden et al. 2012).

Specific enthalpy is generally defined as $H = U + p/\rho$ (Moran et al. 2010) where U is the specific internal energy and p is the pressure, however in this model "enthalpy" equates to "internal energy" $H = U$. Thereby volume work (p/ρ) is not accounted for. In the case of cold ice where T is below the PMP, $T_m(p)$, the specific enthalpy, H_i is defined as

$$H_i = \int_{T_0}^{T} C_i(\tilde{T}) d\tilde{T} \tag{4}$$

where $C_i(T)$ is the heat capacity of ice. The specific enthalpy of liquid water H_w is defined as

$$H_w = \int_{T_0}^{T_m(P)} C_i(\tilde{T})\,d\tilde{T} + L + \int_{T_m(P)}^{T_0} C_w(\tilde{T})\,d\tilde{T} \tag{5}$$

where $C_w(T)$ is the heat capacity of water and L is the latent heat of fusion. The heat capacity of ice, $C_i(T)$, is considered to be a linear function of temperature (Petrenko and Whitworth 1999; Aschwanden et al. 2012). However, as Aschwanden et al. (2012) pointed out, for most modelling purposes it is sufficient to approximate $C_i(T)$ using a constant value independent of temperature. The heat capacity of water, C_w, is also assumed to be constant. For the mixture, the enthalpy density, ρH (volumetric enthalpy) is given by

$$\rho H = \rho_i H_i + \rho_w H_w \tag{6}$$

From equations (1), (2), (3), (4), (5), (6) one derives,

$$H = H(T, \phi, p) = (1-\phi) H_i(T) + \phi H_w(T, p) \tag{7}$$

giving the specific enthalpy of mixtures, containing both cold and temperate ice as well as liquid water. As opposed to cold ice where $T < T_m(p)$ and $\phi = 0$, temperate ice is a mixture where $T = T_m(p)$ and $0 \leq \phi < 1$. The enthalpy of $\phi > 0$, ice at the PMP is defined by

$$H = \begin{cases} H_i(T), & \text{if } T < T_m(p). \\ H_s(p) + \phi L, & T = T_m(p) \text{ and } 0 \leq \phi < 1. \end{cases} \tag{8}$$

To finally derive ice temperatures, an inverse function to $H_i(T)$ exists based on the assumption that $C_i(T)$ is positive. The inverse is denoted by $T_i(H)$ an defined for $H \leq H_s(p)$. Aschwanden et al. (2012) used this definition to differentiate between cold ice and temperate ice. Given the inverse, cold ice is found where a small change in enthalpy triggers a change in temperature alone, while enthalpy fluctuations in temperate ice lead to a change in liquid water fraction (Aschwanden and Blatter 2005; Aschwanden and Blatter 2009). The inverse of equation (**??**) for the different enthalpy values is denoted as

$$T(H, p) = \begin{cases} T_i(H), & T_i(H), H < H_s(p), \\ T_m(p), & T_m(p), H_s(p) \leq H, \end{cases} \tag{9}$$

$$\phi(H, p) = \begin{cases} 0, & H \leq H_s(p), \\ L^{-1}(H - H_s(p)), & H_s(p) \leq H. \end{cases} \tag{10}$$

This inverse relation allows for the simultaneous computation of the englacial temperature as well as the liquid water content (ϕ) for every grid cell along the entire ice column at each time step. Table

(1) lists the physical constants that have been used within IceT to compute englacial tempeartures.

Table 1: Physical constants for ice and water used as basis for the englacial temperature model.

Symbol	Value	Description
λ_i	2.1 $Wm^{-1}K^{-1}$	Ice thermal conductivity
λ_w	0.6 $Wm^{-1}K^{-1}$	Water thermal conductivity
ρ_i	920 kg m^{-3}	Ice density
ρ_s	350 kg m^{-3}	Snow density
ρ_f	550 kg m^{-3}	Firnd density
ρ_w	1000 kg m^{-3}	Water density
C_i	2100 $Jkg^{-1}K^{-1}$	Specific heat capacity of ice
C_w	4200 $Jkg^{-1}K^{-1}$	Specific heat capacity of water
L	334 x 10^3 Jkg^{-1}	Latent heat of fusion
T_m	273.15 K	Melting temperature of ice

2.1.2 Surface energy balance model

To account for surface ablation, a simple surface energy model has been constituted, based on formulas by Cuffey and Paterson (2010). The net energy flux at the upper boundary of the 1-dimensional ice column E_N is a sum of the following components:

$$E_N = \underbrace{E_S^{\downarrow} + E_S^{\uparrow} + E_L^{\downarrow} + E_L^{\uparrow}}_{E_R} + \underbrace{E_H + E_E}_{Turbulent} \tag{11}$$

where $E_S^{\downarrow}$ denotes the downward shortwave radiation, $E_S^{\uparrow}$ the reflected shortwave radiation, and $E_L^{\downarrow}$ and $E_L^{\uparrow}$ the downward and emitted long-wave radiation. Summing up the 4 terms gives the net radiation term E_R. E_H and E_E represent the sensible and latent heat fluxes due to turbulent mixing represented by the parameter h which is set to a constant value of 1.0. For the sake of simplicity, the subsurface energy flux E_G, which is driven by the geothermal heat flux, is not considered. This decision is justified by the study's focus on the sensitivity of englacial temperatures to boundary conditions at the glacier surface. Furthermore, the model does not account for latent energy inputs E_P from precipitation (refreezing rain). Nevertheless, latent heat release due to snow and ice melt is accounted for through the enthalpy formulation, as stated in section (2.1.1). Energy fluxes are measured in energy per unit area, or Wm^{-2}. The following paragraph will further describe the computation of the individual components in chronological order.

The downward radiation term $E_S\downarrow$ is driven by the total flux of solar radiation at the top of the Earth's atmosphere, which is defined by the solar constant $S = 1367 Wm^{-2}$ (Tab. 2) (Cuffey and

Paterson 2010). Annual variations due to eccentricity of the Earth's elliptical orbit are expected to be in the order of a few percent and not accounted for (Cuffey and Paterson 2010). Nevertheless, seasonal and daily variations in incoming radiation have been included to approximate the direct solar beam $E_{Sd}^{\downarrow}$, which is defined as a fraction of S such that

$$E_{Sd}^{\downarrow} = S \cdot \cos Z \cdot \psi \text{ with } \psi = \psi_0^{P/(P_0 cos Z)} \tag{12}$$

where Z is the zenith angle, the angular distance of the sun below a vertical line, varying with latitude ϕ, time of the year, and time of the day (Oke 2014). Atmospheric transmissivity is represented by the parameter ψ with $\psi \leq 1$. At sea level and under clear sky conditions ψ_0 is about 0.84, whereas under thick cloud cover it reduces to zero (Cuffey and Paterson 2010). As the direct solar radiation increases with altitude the term ψ_0 is introduced which depends on the ratio of P/P_0, where P denotes the pressure at the glacier surface and P_0 the pressure at sea level (ca 101.3 kPa) (Barry and Chorley 2009). A value of 70 kPa is chosen for P_0, which under idealized standard atmospheric conditions (15°C, 0% humidity) corresponds to a pressure at 3000 meters above sea level (Barry and Chorley 2009). The latitude ϕ for all model runs is set to 46.54 ° (Jungfraujoch), which can be seen as representative for Swiss glaciers, as latitudinal variations in Switzerland are small (45.8°-47.8°), even smaller when considering only glaciated regions (ca. 45.9°-47.0°) (Swisstopo 2023) and their relative effect on irradiance is thus negligible. The cosine of the zenith angle is denoted as

$$\cos Z = \sin\phi \sin\delta + \cos\phi \cos\delta \cos h \tag{13}$$

where δ marks the solar declination, meaning the angular distance between the sun and the equator, which itself is defined as

$$\delta = 23.45° \sin\left(\frac{360}{365}(284 + n)\right) \tag{14}$$

where n denotes the days since the beginning of the year. δ is limited to the Earth's tilt of ± 23.45°. The hour angle h is coupled to the hour of the day such that $h = 0$ at local noon. It is denoted as

$$h = \frac{360°}{24h}(t_{sol} - 12h) = \frac{15°}{h}(t_{sol} - 12h) \tag{15}$$

Equations (14) and (15), describing the Earth-Sun angles are based on formulas by Brownson (2014). To account for the reflectance of shortwave radiation due to different surface types, such as snow or ice, the incoming shortwave radiation is multiplied by the surface albedo $E_S^{\uparrow} = \alpha_s E_S^{\downarrow}$. In order to simplify the computation, reflected shortwave radiation is accounted for by denoting

$$E_{SN} = E_S^{\downarrow}[1 - \alpha] \tag{16}$$

where E_{SN} is the net shortwave radiation with respect to a given surface albedo α. Constant albedo values for snow, ice and firn were applied, taken from literature (Cuffey and Paterson 2010). The

snow albedo α_s is set to 0.65, the firn albedo α_f is set to 0.55 and the ice α_i is set to 0.45. The annual cycle for the 3 shortwave radiation model components $cosZ$, ψ, δ as well as the resulting incoming shortwave radiation $E_S\downarrow$ is displayed in figure 2.

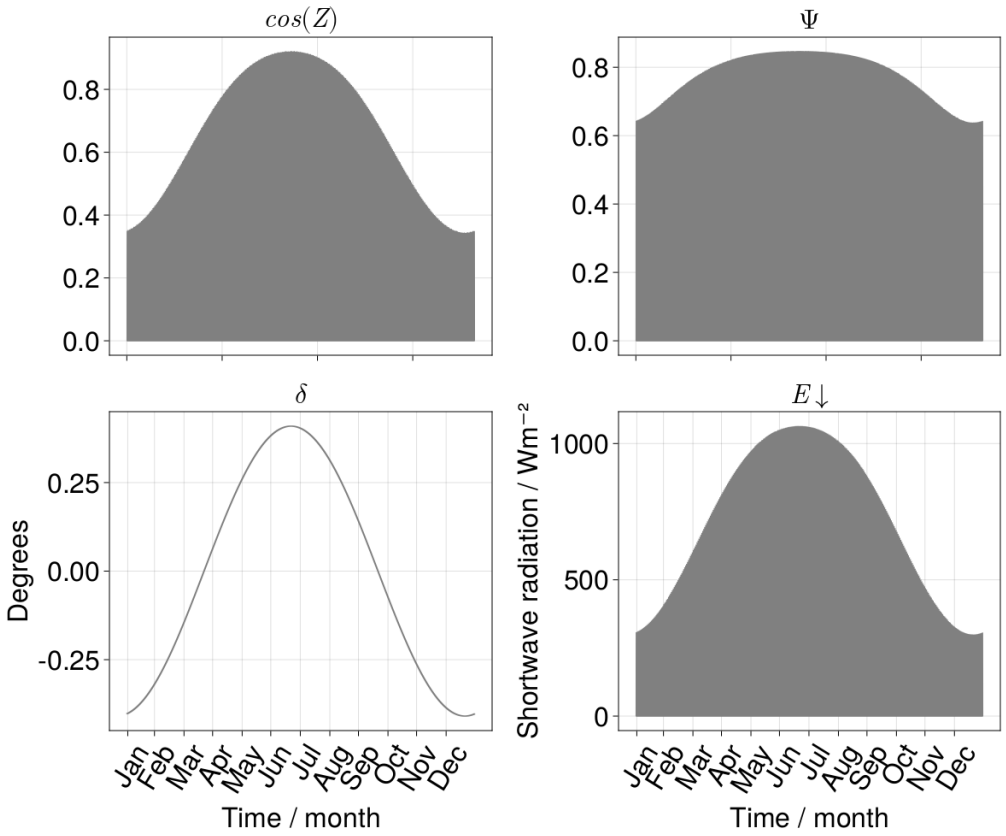

Figure 2: Annual cycle of the 3 shortwave radiation model components (A) cos(Z), (B) ψ, (C) δ and the resulting incoming shortwave radiation (D) $E_S\downarrow$ given the parametric setting in table (2).

Emitted longwave radiation $E_L\uparrow$ is modeled based on the assumption that snow, ice and liquid water are near-perfect radiators with emissivities of $\epsilon = 0.95$ (Hori et al. 2006)(Tab. 2). It is denoted as

$$E_L^{\uparrow} = -\epsilon_s \sigma T_s^4 \tag{17}$$

depending on the surface temperature T_s multiplied by the Stephan-Boltzmann constant σ for a black body. At $T_m = 273.15$ K, $E_L^{\uparrow}$ is equal to -315.6 Wm^{-2}. The downward long wave radiation term $E_L\downarrow$ depends on atmospheric greenhouse gas concentrations (greenhouse effect), such as water vapor, carbon dioxide, ozone or methane. It has been pointed out that $E_L^{\downarrow}$ varies significantly depending on the atmospheric composition (Cuffey and Paterson 2010). However, regional data on temporal variations in atmospheric composition is sparse and for the sake of simplicity $E_L^{\downarrow}$ is computed using a transmissivity factor ϵ_a such that

$$E_L^{\downarrow} = \epsilon_a \sigma T_a^4 \tag{18}$$

as a function of the near surface air temperature T_a. ϵ_a is estimated to be around 0.95 for completely cloudy skies, whereas it reduces to 0.5 under dry and cloudless conditions (Cuffey and Paterson 2010). A consistent value of 0.8 is chosen for all model runs, which has been found to be a good estimate for a late summer average (Hock and Holmgren 2005).

The long-wave components of the surface energy model, $E_L\downarrow$ and $E_L\uparrow$, are primarily influenced by atmospheric temperature. In this study, we actively manipulate atmospheric temperature to represent the impact of varying elevation levels on englacial temperatures. The process of how these parameters are obtained will thus be discussed later. For the shortwave model components $E_S\downarrow$ and $E_S\uparrow$, which together constitute a significant portion of the energy input at the glacier surface, a constant value is applied for each parametric setting based on approximations. As a multiplier within equation (12), the atmospheric transmissivity parameter ψ_0 dominates the outcome of $E_S\downarrow$. Since only few estimates of ψ_0 for glaciated regions exist (Cuffey and Paterson 2010; Konzelmann and Ohmura 1995; Hoyt and Fröhlich 1990), it has been adjusted to fit the radiation cycle of IceT to reference climatological (1993-2013) averages in shortwave global irradiance of several Swiss sites (Figure 4). A value of $\psi = 0.8$ was found to fit best. The resulting annual shortwave radiation cycle can be seen in figure 3.

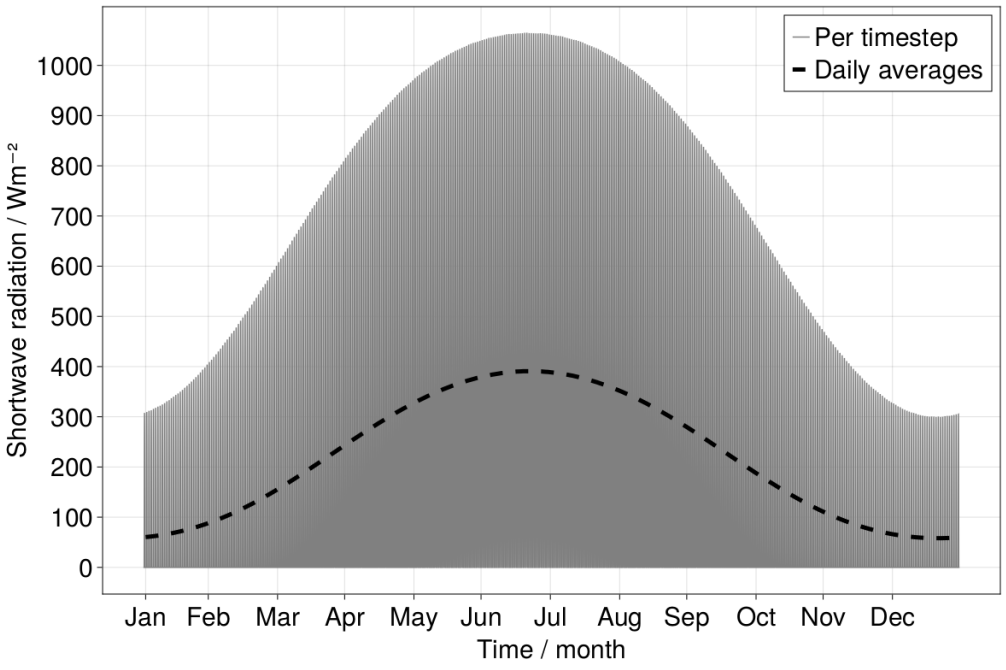

Figure 3: Modeled annual shortwave radiation cycle. The gray line depicts the per-timestep computed radiation, containing daily fluctuations. The dashed black line depicts the averaged daily radiation.

At peak summer the modeled irradiance reaches daily averages of ca. 390 W/m^2, whereas in winter it reaches its low-point averaging at ca. 58.1 W/m^2. Diurnal variations lead to maximum values in summer 0f 1063 W/m^2, while in winter they reduce to a maximum of ca. 310 W/m^2 during noon. This radiation cycle compares well to those of the stations depicted in figure (4), depicting the annual irradiance cycles for Payerne, Locarno-Monti, Davos and Jungfraujoch based

on measurements taken between 1993 and 2013 (MeteoSwiss 2023). For an overview of the physical constants used within the radiation model see table 2.

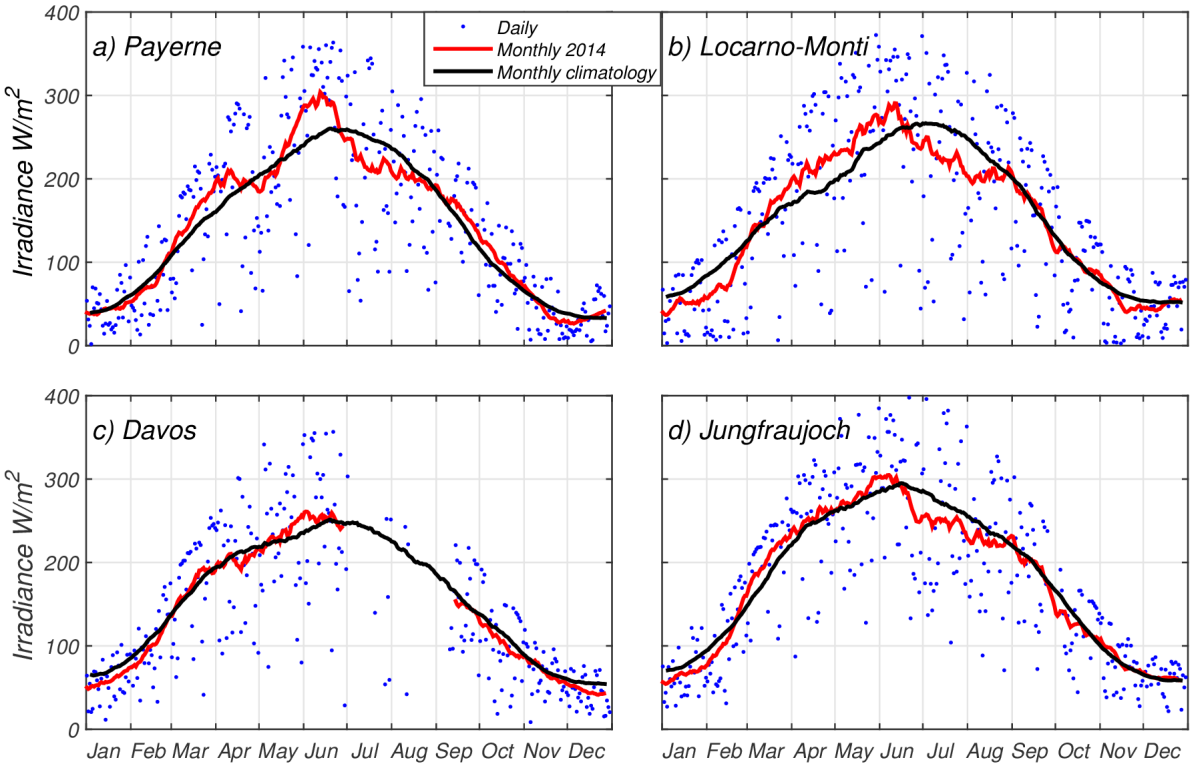

Figure 4: Mean annual climatological irradiance for several sites in Switzerland (reference period 1993-2013), used for approximation of the transmissivity parameter ψ_0 within IceT's shortwave radiation model. The blue dots depict daily average values for the year 2014, the red line the monthly averages for 2014, whereas the black line depicts the monthly climatological average (MeteoSwiss 2023).

Table 2: Physical constants used within the radiation model.

	Value	Description
Shortwave model		
σ	5.67 x 10^{-8} $Wm^{-2}K^{-1}$	Stefan-Boltzmann constant
S	1367 Wm^{-2}	Solar constant
ψ	0.8	Atmospheric transmissivity
P	101.3 kPa	Pressure at sea level
P_0	70 kPa	Pressure at the glacier surface
ϕ	46.54°	Latitude (Jungfraujoch)
α_s	0.65	Default snow albedo
α_f	0.55	Default firn albedo
α_i	0.45	Default ice albedo
Longwave model		
ϵ_s	1.0	Emissivity of the ice
ϵ_a	0.9	Emissivity of the air

2.1.3 Mass balance

Snow accumulation occurs at the first grid cell which is not declared as ice. The model's mesh with a grid spacing of $dz = 0.1$ meters would only allow for accumulation rates ≤ 10 cm. Increasing the resolution is computational inefficient, therefore a coordinate view within the first air grid cell has been implemented. A variable z_{surf} traces the current position of the snow-air interface and can receive small accumulation rates. It is coupled to the coordinate of the uppermost grid cell which is defined by the air index i_{air}. As soon as the difference between the vertex coordinate of i_{air} - 1 (can be either glacier or snow) and that of z_{surf} exceeds the grid spacing dz, the cell will be counted as snow within the next iteration.

All precipitation during air temperatures smaller than 0 ° is counted as snowfall. A volume conversion from water to snow is conducted with

$$vol_s = vol_w \cdot \frac{\rho_w}{\rho_s} \tag{19}$$

where the liquid precipitation volume vol_w is multiplied by the ration of the water density ρ_w = 1000 kgm^{-3} over the density of snow ρ_s = 350 kgm^{-3}, given the densities in table 1. It is a simplified accumulation model that does neither account for effects like wind-driven snow redistribution nor snow contributions by avalanches, however in a 1-dimensional context such effects are anyways

hard to estimate and can only be guessed through parameterization.

The same coordinate tracing as for the accumulation is applied for snow and ice melt, which is directly coupled to the water volume fraction. As stated in section 2.1.1 through the enthalpy formulation, the liquid water content ϕ is continuously computed within each grid cell along the entire ice column. As denoted in equation 10 ϕ itself is a function of enthalpy and pressure. Liquid water occurs as soon as the enthalpy H is greater or equal to the critical enthalpy H_s at $T = T_m(p)$. The englacial temperature T is a function of air temperature, which is actively manipulated within the parametric study (see 2.4), while for the calibration runs temperatures are fetched from the MeteoSwiss dataset utilized within the study of Huss and Fischer (2016). For elevation discrepancies between the weather station and the glacier location an annually constant lapse rate of dT/dz = -6°km^{-1} is applied. When the liquid water content (represented by ϕ) in the topmost snow, firn, or ice grid cell reaches 100%, indicating full saturation, it will be considered as runoff. Subsequently, in the next time step, the grid cell will be designated as air. Depending on the state of the grid cell a volume conversion from ice, snow or firn to water is applied using the same principle as in equation (19) where ρ_i = 920 kg m^{-3} and ρ_f = 550 kg m^{-3}, and the resulting water volume will be added to the ablation.

2.1.4 CTS tracking

The definition of the cold-temperate transition (CTS) is challenging and can result in over or underestimation of the same. In a fundamental sense, the CTS separates water-free cold ice from moist temperate ice (Pettersson et al. 2004; Gusmeroli et al. 2010). Within IceT, index tracking is used to identify the CTS, which is defined as the first location within the ice column of size z where the englacial temperature T_i at index j is smaller than -0.01°C. The CTS depth is then computed by calculating the vertical distance between the uppermost vertex that is still defined as ice and the vertex denoting the location of the CTS within the ice column.

2.1.5 Numerical methods & model mesh

Equations (6) requires numerical approximation. Forward differences for the enthalpy are computed along the computational grid (z) and are denoted as

$$f'(z) \approx \frac{df(z)}{dz} \approx \frac{f(z+\Delta z) - f(z)}{\Delta z} \tag{20}$$

Averaged differences for the heat flux from the uppermost grid cell along the z axis are computed as

$$\bar{f}(z) \approx \frac{f(z) + f(z+\Delta z)}{2} \tag{21}$$

Finally, englacial temperatures and the water volume fractions are derived from the resulting values for the internal energy U using equation (9) and (10).

The time step Δt is adjusted to approximately guarantee von Neumann stability (Crank and Nicolson 1947) and is denoted as

$$\Delta t = \frac{\Delta z^2}{\left(\frac{\lambda_i}{\rho_i \cdot C_i}\right) \cdot 8.1} \tag{22}$$

On the basis of the pysical constants (Tab. 1) for the ice thermal conductivity λ_i, the ice density ρ_i as well as the specific heat capacity of ice C_i a timestep of Δt ≈ 70 minutes is computed.
IceT is initialized with an ice thickness of 70 meters, as glaciers within the studied size category (< 0.5 km^2) typically do not exhibit thicker ice (Signer 2014; Grab et al. 2021). Furthermore, increasing the ice thickness could compromise the model's resolution or lead to an unnecessary increase in computational workload. Given that this study primarily focuses on resolving surface processes, maintaining a consistent model mesh was crucial across all runs, including calibration trials. Various model runs were conducted at different spatial resolutions (200, 500, 1000), with n_z = 1000 vertices proving to be the most accurate configuration. Given a model domain l_z of 100 meters, where 30 meters are predefined as air space and 70 meters are set to be glacier ice, a grid spacing $dz = l_z / n_z$ of 0.1 meters (10 cm) results. Table (3) gives an overview of the default model dimensions.

Table 3: Default model dimensions

Symbol	Value	Description
a_z	30 m	Initial air column
l_z	70 m	Initial ice thickness
f_z	0 m	Initial firn thickness
n_z	1000	Model resolution
dz	0.1 m	Grid spacing

2.2 GERM

In addition to developing the in section (2.1) introduced model, a detailed reanalysis of ice temperature modelling data, generated in the framework of a study by Huss and Fischer (2016), has been conducted. The study uses the Glacier Evolution Runoff Model (GERM) to investigate the sensitivity of very small glaciers (≤ 0.5 km^2) within the Swiss Alps to future climate change. To facilitate the comparison between IceT and GERM modeling results, a brief outline of GERM's model structure will be presented. However, an emphasis is laid on the ice temperature component as it's output is of most relevance for this thesis.
GERM was initially developed to compute mass balance and calculate runoff (Huss et al. 2008; Farinotti et al. 2012), however it has been further extended by an englacial temperature model. The

model includes components for (1) glacier surface mass balance (accumulation and ablation), (2) evaporation, (3) runoff routing, (4) the change in glacier surface topography and glacier retreat as well as (5) ice temperatures.

2.2.1 Mass balance

Accumulation of snow is given for each position (x, y) on the glacier and day t and denoted as

$$C(x, y, t) = P(t) \cdot C_{prec} \cdot D)x, y) \tag{23}$$

where $P(t)$ is the precipitation for local air temperatures $T(x, y, t) < T_{thr}$, which are extrapolated to all grid cells using an annually constant lapse rate dT/dz = -6°C km^{-1}. The threshold, T_{thr} = 1.5°C, controls whether solid or liquid precipitation occurs. C_{prec} serves as a factor to fine tune precipitation based on the conditions on the individual glacier as well as errors in the gridded precipitation data. Furthermore, redistribution of snow due to e.g. wind drift is accounted for by using a dimensionless snow distribution multiplier $D(x, y)$ (Farinotti et al. 2010). Snow and ice melt is generated using a distributed-index model (Hock 1999). A classic degree-day factor method is coupled to potential direct radiation to account for the effects of slope, aspect and shading (Huss and Fischer 2016).

$$E = d(1 - \alpha)Q_e + C_0 + C_1 \cdot T_a \tag{24}$$

Snow and ice melt is computed using a degree-day factor as a function of potential direct radiation, accounting for effects of slope, aspect and shading. Daily surface melt rates M(x,y,t) are computed as

$$M = \begin{cases} (f_M + r_{snow/ice} I_{pot}) & : T \leq 0°C \\ 0 & : T \leq 0°C \end{cases} \tag{25}$$

where f_M is a melt factor, $r_{snow/ice}$ are radiation factors for snow and ice surfaces and I_{pot}(x,y,t) is the potential solar radiation. Furthermore the model accounts for the effects of debris cover by multiplying the melt by a reduction factor f_{debris}, which depends on the thickness of the debris layer (Huss and Fischer 2016):

$$M_{debris}(x, y, t) = f_{debris} \cdot M(x, y, t) \tag{26}$$

As debris cover is assumed to both increase in space as well as thicken, this effect is parameterised by prescribing a linear decrease in f_{debris} with time. Debris-covered areas are presumed to propagate upglacier with time (Huss and Fischer 2016). In addition the model accounts for mass losses due to frontal break-off based on comparable ice fluxes within this domain (Alean 1985; Pralong and Funk 2006).

2.2.2 Glacier geometry

Furthermore, ice thickness and glacier extent are derived, using mass conserving Δh-parameterization (Huss et al. 2008; Huss et al. 2010). This empirical function relates glacier surface elevation change by mass losses to the glacier's altitudinal range. On the basis of this, one expects strong thickness changes at the snout, while the accumulation area varies only slightly (Huss and Fischer 2016). Glacier extent results from the fact that a glacier area disappears as soon as the ice thickness becomes zero.

2.2.3 Englacial temperatures

Englacial temperatures are computed using a one-dimensional heat transfer model, that includes melt and refreezing processes which are again coupled to the glacio-hydrological model (Huss and Fischer 2016). Temperatures are calculated for each 0.5 m layer starting from the base/bedrock interface till the surface based on heat conduction as

$$\frac{\partial T_g}{\partial t} = \frac{1}{c_h \cdot \rho} \frac{\partial}{\partial z} \left(\kappa \frac{\partial T_g}{\partial z} \right) \tag{27}$$

where c_h is the heat capacity of ice, κ the thermal conductivity and ρ the firn/ice density. It is important to notice, that advection of ice is not accounted for, based on the assumption that glacier dynamics are reduced to a minimum for very small glaciers (≤ 0.5 km^2). Equation (27) is solved explicitly at daily resolution. The firn/ice temperature $T_{g,0}$ f the uppermost layer is assumed to equal the daily mean air temperature if the snow depth d is smaller than a threshold $d_{crit,low}$, while if it is greater than an upper threshold $d_{crit,high}$, $T_{g,0}$ is set to 0°C. Between the two thresholds the temperature of the uppermost snow layer is linearly interpolated between the daily mean air temperature and 0°C on the basis of d (Fig. 5). Full permeability of the firn is assumed and the free pore space in the firn layer can be filled with water or air from surface melt or rain, given a fixed porosity. Runoff is generated at the base of the snowpack and is intentionally augmented with the increase in steepness of the terrain. The refreezing of water within the snowpack is permitted, and the resulting effects on the ice temperature due to latent heat release are factored in. In contrast, no vertical water transfer through the ice is possible. The ice is predominantly considered impermeable, except for the uppermost 0.4 meters. In this section, a constant porosity is presumed along with a finite value for the maximum water content (Signer 2014; Huss and Fischer 2016).

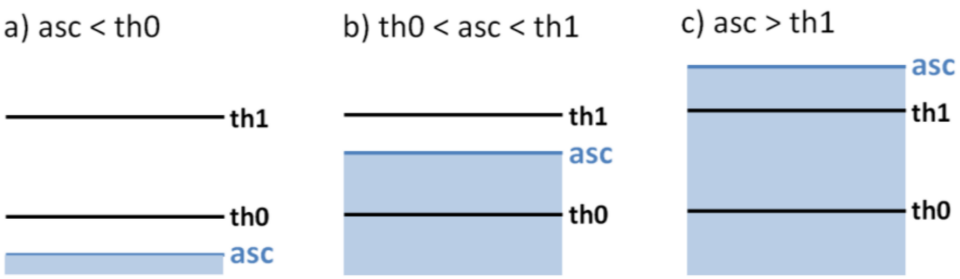

Figure 5: Framework used to model the insulation of the snow cover within GERM. $th0$ represents the lower threshold and $th1$ the upper threshold, while asc abbreviates the actual snow cover. (a) Scenario where asc > th0, (b) scenario where th0 < asc < th1 and linear interpolation between the air temperature and 0 Illustration drawn from Signer (2014).

2.3 Model calibration

Calibrating englacial temperature models presents challenges due to the complex interactions between various factors such as the atmospheric forcing, mass balance, glacier dynamics, as well as the spatio-temporal variations of englacial water content. These factors collectively determine the evolution of englacial temperatures. In the context of these small-sized glaciers, glacier dynamic is considered negligible. Furthermore, the current model assumes a constant water content as no permeability is yet implemented, certainly leading to biases within the modelling results that will be further discussed later. However, it is crucial to calibrate the mass balance component to accurately capture the 1-dimensional ice temperature evolution. Within this study, the model is applied on a subset of 20 very small glaciers (< 0.5 km^2) on the basis of MeteoSwiss gridded temperature and precipitation data (MeteoSwiss 2014a; MeteoSwiss 2014b). The same data set has been used within a study by Huss and Fischer (2016) to model the evolution of the 1133 very small glaciers within the Swiss Alps using GERM. A fully automated calibration scheme for IceT was conducted based on the GERM mass balance results. For each of the very small glaciers (< 0.5 km^2) that have been modeled with GERM in 2016 there exists a unique meteorological data set together with a modeled mass balance record (Huss and Fischer 2016). The data set comprises daily resolution air temperature, precipitation and sunshine hours representing 1 kilometer grid cells. While the precipitation and sunshine data is directly derived from the respective MeteoSwiss data point, Huss and Fischer (2016) apply seasonally varying lapse rates on the air temperature record based on the glacier reference elevation. Within GERM, local correction factors for precipitation (f_{prec}), melt (f_M) and radiation ($r_{\text{snow/ice}}$) are applied to fine-tune the model's mass balance on geodetic mass balances by Fischer et al. (2015) on a 10 meter grid. For simplicity, IceT is run on the initial data representing 1-kilometer grid cells. A single model run is conducted for each glacier-specific data set, averaging out small scale meteorological differences across the glacier. In this way, IceT produces point based averaged mass balances, which are compared against spatially interpolated glacier wide mass balances from GERM during the calibration process. Perfect matches are thus not expected. Most of the physical constants depicted in (2) have been drawn from literature and

are kept constant during the calibration process, however the surface albedo α remains unknown and thus requires calibration. This calibration process is separated into several steps.
In a first step, values for the snow albedo α_s and ice albedo α_i are drawn from literature. α_s is set to 0.65 which is a reasonable mean given a known snow albedo range of 0.4 and 0.85, while α_i is set to 0.45 (Cuffey and Paterson 2010). Within a second step, a radiation factor C_{rad} is used to tune the shortwave radiation model. The net shortwave radiation term $E_S N$ of equation (16) is thus denoted as

$$E_{SN} = E_S^{\downarrow}[1 - \alpha \cdot C_{rad}] \tag{28}$$

where $E_S^{\downarrow}$ is the incoming shortwave radiation and α is the surface albedo. In a fully automated iterative process, annual mass balances generated by GERM are systematically compared to those produced by IceT. The objective is to minimize the discrepancies between the two models. This calibration procedure is executed individually for each of the 20 glaciers within a loop involving 30 different calibration factors, resulting in a total of 20·30 = 600 model runs. During each iteration, the average of all annual mass balance residuals is computed. The calibration factors are incrementally adjusted, using a step size of 0.01. The iteration halts upon detecting the minimum average residual, at which point the corresponding calibration factor is selected as the final parameter. A range of calibration factors for C_{rad} between 0.9 and 1.2 (25%) effectively replicated the long-term mass balance trends obtained from the GERM dataset/model. Calibration runs were conducted given the model dimensions mentioned in section 2.1.5 and the physical constants for ice and water (Tab. 1). As with all model runs the glacier is assumed temperate (0 degrees) and with the water volume fraction ϕ fixed at 0% along the entire ice column. Furthermore, the glacier is initialized without any firn cover.

Mass balance calibrations are exemplarily showcased below for both Glacier du Sex Rouge, a small glacier located in the canton of Vaud, as well as Vadret dal Corvatsch a similarly sized glacier located beneath the peak of Piz Corvatsch in the Bernina Range (Canton Grisons). Both of them are glaciers where direct englacial temperature observations through several boreholes are available (Laternser 1992; Signer 2014). Figure 6 shows the 1962-2014 mass balance modelling results of IceT (solid) against the same period modeled with GERM (dashed) (Huss and Fischer 2016). The mass balance components are depicted (A) as well as the annual mass balances. Furthermore, the residuals, between the two mass balances are depicted (C) as well as the cummulative mass balances (D). IceT is able to reproduce the long-term annual mass balance trend of GERM, while in most cases also tracing the inter-annual variations. The annual residuals offset each other as can be seen in the mean value (μ=0.05 m water equivalent). This is also reflected in the cummulative mass balance trend, which matches quite well with the GERM results. Nevertheless, some years depict very strong residuals as e.g. 1976 (Res. = -2.2 m w.e.) or 2003 (Res. = 1.4 m w.e.) resulting in a high standard deviation (σ=0.74 m w.e.). Furthermore, IceT seems to systematically underestimate the winter

mass balance and overestimate the summer mass balance by a factor of 2.

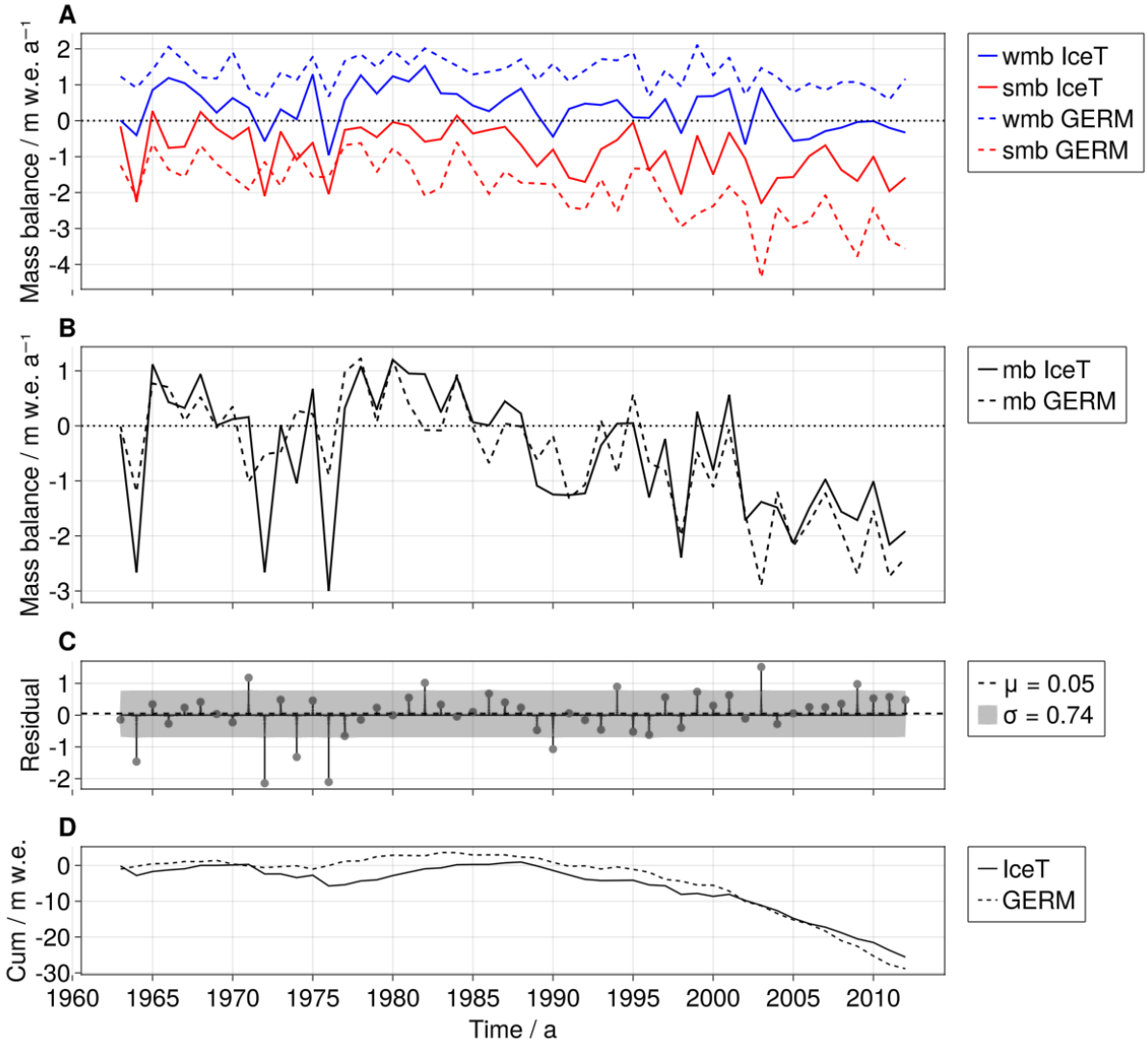

Figure 6: Mass balance comparison of GERM (dashed) against IceT (solid) for Glacier du Sex Rouge. (A) Winter and summer mass balance. (B) Net annual mass balance.

The same comparison has been conducted for Vadret dal Corvatsch (Figure 7). Similar to Sex Rouge, the annual mass balance trend matches very well and inter-annual variations can be mostly reproduced. Residuals are almost completely offsetting each other ($\mu = 0.01$ m w.e.), which results in a very good match of the cummulative mass balance (D). However, a similar picture as for Sex Rouge can be seen when it comes to the mass balance components. The winter mass balance is underestimated by a about 1.0 m water equivalent, however this is compensated by less melt during ablation.

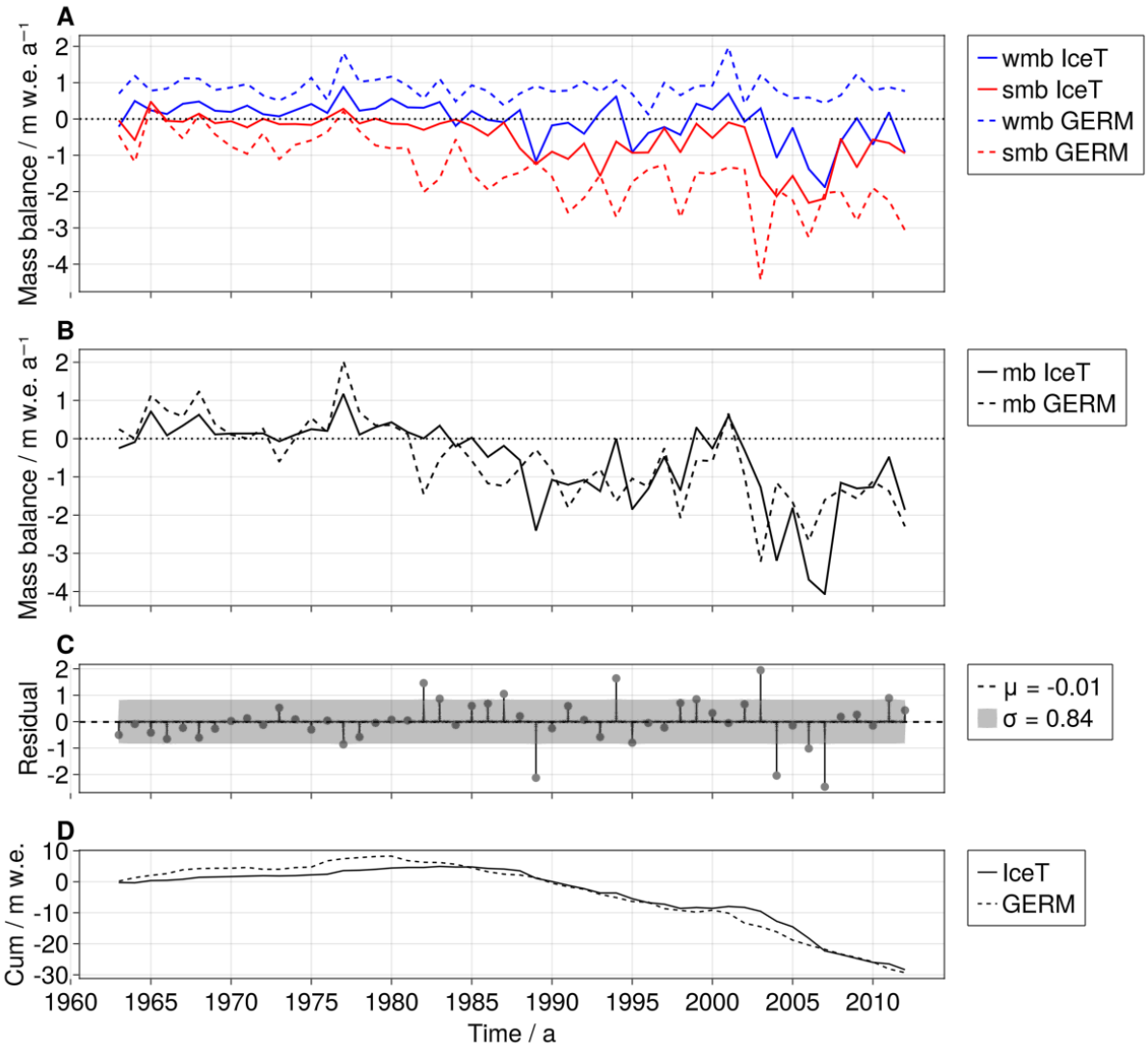

Figure 7: Mass balance comparison of GERM (dashed) against IceT (solid) for Vadret dal Corvatsch. (A) Winter and summer mass balance. (B) Net annual mass balance.

The calibration runs have proven IceT's capability to accurately replicate long-term mass balance trends. Nonetheless, notable inaccuracies persist regarding the mass balance components (winter- & summer mass balance), with an overall tendency to underestimate their divergence. Moreover, significant inter-annual deviations are apparent, as indicated by the mean standard deviation of the residuals (σ = 0.68). Despite this, annual residuals are largely offsetting each other, which results in a relatively low average residual between IceT-modeled mass balances and GERM for all 20 glaciers at μ = -0.06 m (w.e.). This underscores IceT's potential to reproduce the long-term annual and cumulative mass balance trends observed in GERM.

2.4 Parametric study

To gain a deeper understanding of the conditions that initiate a shift from temperate to polythermal states in very small Alpine glaciers, a sensitivity study on englacial temperatures is undertaken. A synthetic air temperature and precipitation model are constructed to generate simulated temperature and snowfall values at the model's temporal resolution. The aim of this parameter study is not to precisely replicate climate conditions, but rather to test the overall sensitivity of the model. The study assesses the sensitivity of englacial temperatures to various parametric settings within a 7-dimensional parameter space, encompassing the following parameters:

1. **Surface energy budget**
    - $MAAT$, the mean annual air temperature
    - α_s, the snow albedo
2. **Snow**
    - P_s, the total annual snowfall
    - σ, the total number of snowfall days per year
    - $t_{0,s}$, the deviation of the snowfall peak from January
    - f_z, the initial firn thickness
3. **Water volume fraction**
    - ϕ, the water volume fraction

A focus is set on those parameters defining the availability and timing of the firn and snow cover (P_s,σ,$t_{0,s}$,f_z). Also, parameters affecting the surface energy balance are utilized, such as the mean annual air temperature ($MAAT$) as well as the the snow albedo α_s. Moreover, the enthalpy formulation (Aschwanden et al. 2012) allows to prescribe the water volume fraction ϕ (in %) within each grid point, to study its effect on the englacial temperature.
A Cartesian combination comprising all parameters is created, and the model is executed using all possible 7-dimensional parametric combinations. The majority of effects have been observed to demonstrate linearity. Hence a uniform parameter range of 3 is employed, leading to a total of 3^7=2181 simulations. Although the specified ranges may not encompass all possible values found in the Swiss Alps, increasing the resolution of the parameter space incurs significant computational expenses. An initial configuration is established to facilitate a two-dimensional exploration of the parameter space. In this setup, all parameters are maintained at default values, while only two parameters are subjected to variation. It is important to note that simulation runs that exhibit significant positive mass balances are deliberately omitted from the data output. A threshold is used as soon as the snow depth reached more than 3 m (w.e.). This exclusion is made due to the absence of a compaction model in IceT, which currently only allows the glacier to accumulate snow

and no transformation to firn or ice takes place. Without a compaction model, very thick snow layers might introduce considerable biases in the computation of ice temperatures. This omission holds significant implications for data interpretation, which will be further elaborated on later.
The subsequent explanation will delve into how the prescribed parameter ranges are selected and incorporated into the model. This will be done separately for the three parameter classes.

2.4.1 Surface energy budget

Two parameters are designed to regulate the amount of energy input at the surface: snow albedo (α_s) and mean annual air temperature ($MAAT$), both of which essentially control the melt rate. Values for the range of α_s are obtained from literature sources (Cuffey and Paterson 2010). Snow albedo can vary significantly, with wet debris-rich snow having an albedo below 0.4, while fresh dry snow can reach albedo values beyond 0.9. Based on this, a parameter range for α_s of 0.4, 0.65, and 0.9 is implemented. However, variations in the parameter α_s can be perceived more broadly as changes in the incoming shortwave radiation. These differences can stem from various factors, such as shading, saturation of snow with water, snow coverage by dust or other particles, among several other influences.
In order to represent seasonal variations within the air temperature, a sinusoidal model is constructed where the air temperature T_{atm} at time step t is denoted as

$$T_{atm}(t) = MAAT + A + \sin(\omega * (t_t - t_{0,t})) \tag{29}$$

where MAAT is the mean annual air temperature, A represents the air temperature amplitude, ω is the frequency of the sinusoidal cycle which is set to $\frac{2\pi}{\text{seconds per year}}$, t is the current time step in seconds, and t_0 stands for the time offset in seconds. Lowest air temperatures are assumed at the beginning of the year (1st of January), thus the time offset is adjusted in such a way that the minimum of the sinusoidal temperature curve coincides with the start of the temperature cycle. In order to represent annual air temperature cycles within the Swiss Alps, a reasonable value for the MAAT as well as the amplitude A need to be found. To approximate the air temperature amplitudes, least-squares sine fitting was applied to meteorological records from several weather stations in Switzerland. This analysis is depicted in figure 8.

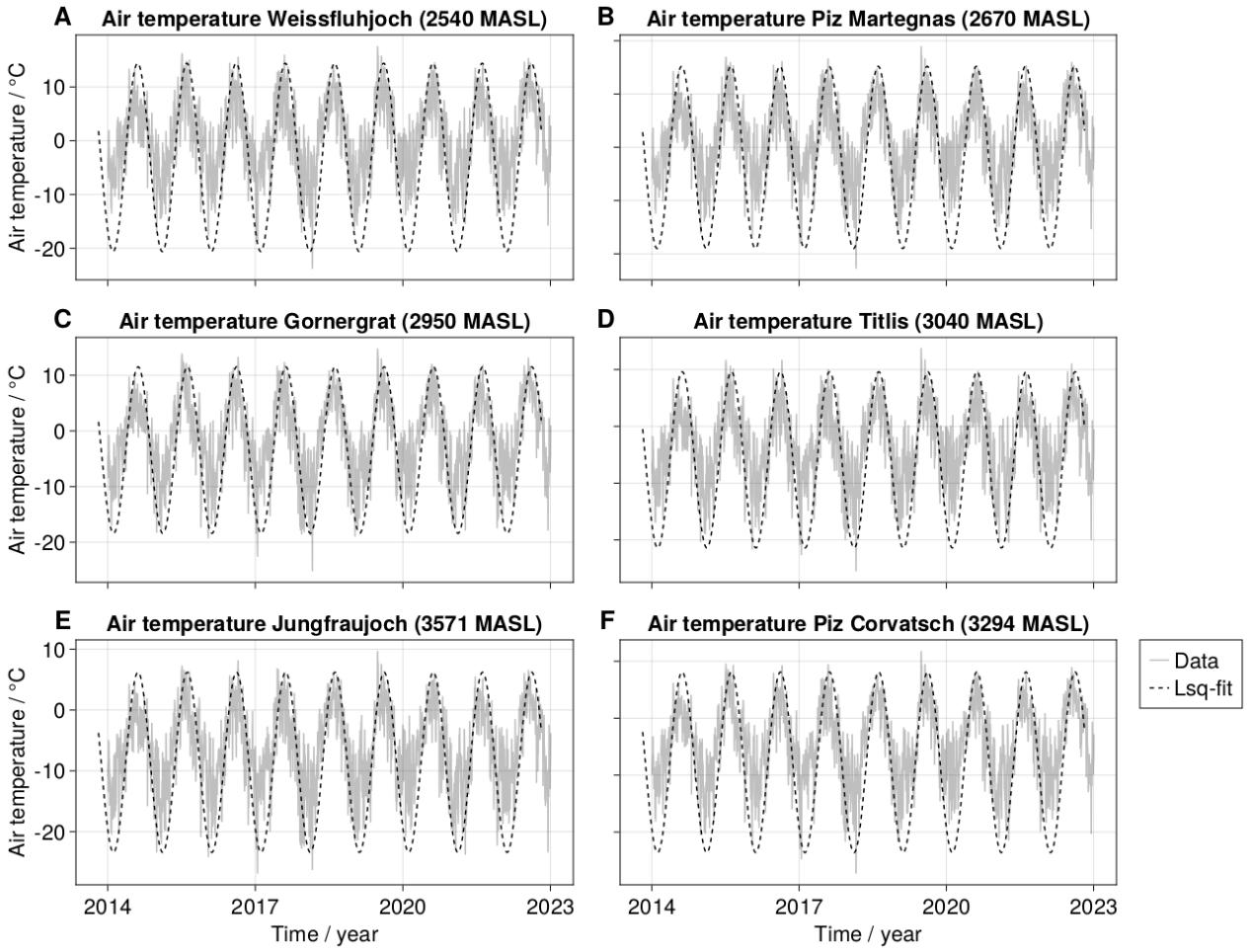

Figure 8: Least-squares sine fitting results based on 9 year air temperature records (2014-2022) for (A) Les Diablerets, (B) Piz Martegnas (2670 MASL), (C) Gornergrat (2950 MASL), (D) Titlis (3040 MASL), (E) Jungfraujoch (3571 MASL) and (F) Piz Corvatsch (3294 MASL).

Air temperature records from 2014 to 2022 for six Alpine weather stations at various elevations (ca. 2500-3500 MASL) are shown. Least-square fitting results in an air temperature amplitude of A = 17.5 °C for Weissfluhjoch at 2540 MASL and A = 17.1°C at Piz Martegnas (2670 MASL). For Gornergrat, situated at 2950 MASL the amplitude reaches 15.2 °C, while for Titlis situated at 3040 MASL A = 15.5°C. At the two highest location Jungfraujoch situated at 3571 MASL A = 14.79 °C, while for Piz Corvatsch at 3294 MASL A = 15.85 °C. Additional fittings have demonstrated that the station-to-station variance in the temperature amplitude is relatively low (σ = 1.08°C), averaging around 16°C. Consequently, it has been decided to maintain this value in order to reduce the complexity of the parameter space.

The MAAT is selected to roughly represent the range of air temperatures found at different elevation levels within the Swiss Alps. MAATs were computed for 15 weather stations situated across the Swiss Alps (Reference period 2014-2022). A linear regression model was fitted to these measurements to obtain an estimate for the lapse rate as well as the absolute values at specific elevation levels. Figure 9 shows the results of the linear model together with the reference wet-adiabatic lapse rate of dT/dz = -6°C km^{-1}, as well as the MAATs of the individual weather stations. The linear model suggests a

significantly lower lapse rate of dT/dz = -5.1°C km^{-1}. On the basis of this model, air temperature categories for various elevation levels (2500-4000 MASL) were computed. These categories are presented in figure 9B.

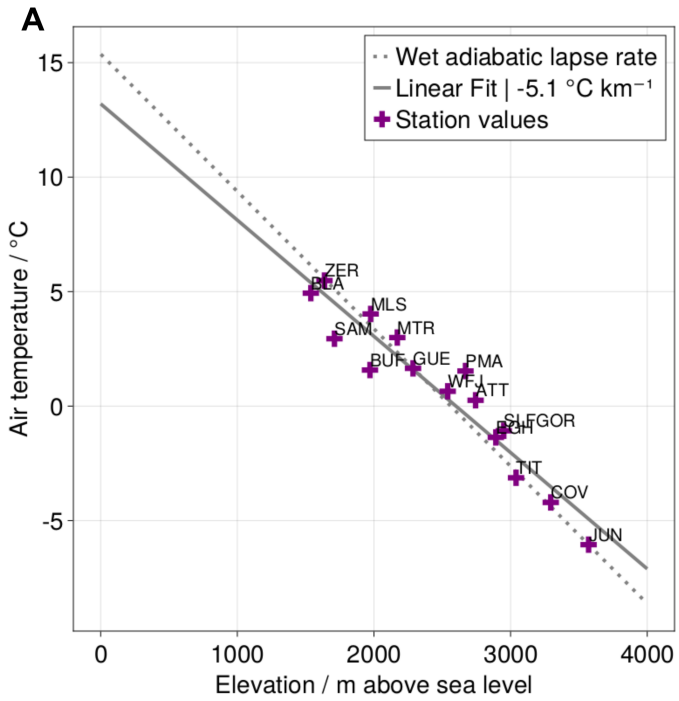

B

Elevation / m above sea level	MAAT / °C
2500	0.51
2750	-0.76
3000	-2.03
3250	-3.29
3500	-4.56
3750	-5.83
4000	-7.1

Figure 9: (A) Lapse-rate approximation for the Swiss Alps based on linear fitting of mean annual air temperatures (Reference period 2014-2022) for several Swiss weather stations. Jungfraujoch (JUN), Piz Corvatsch (COV), Titlis (TIT), Gornergrat (SLFGOR), Eggishorn (EGH), Les Attelas (ATT), Weissfluhjoch (WFJ), Piz Martegnas (PMA), Gütsch (GUE), Buffalora (BUF), Matro (MTR), Samedan (SAM), Le Moléson (MLS), Zermatt (ZER), Blatten, Lötschental (BLA). (B) MAAT at discrete elevation levels resulting from the linear model.

Based on these results a range for $MAAT$ of -3.3,-5.5 and -9.0 °C is utilized. In the default setting, a mean annual air temperature (MAAT) of -5.5°C is employed. Figure (10) depicts the sinusoidal air temperature curve using the default settings and assuming an amplitude A of 16°C.

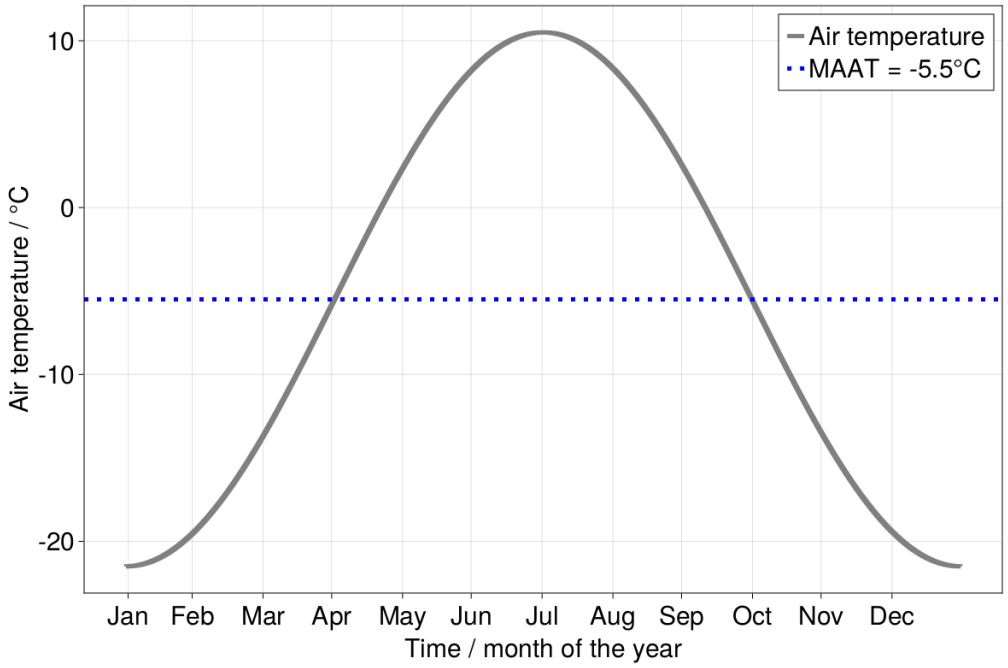

Figure 10: Default annual air temperature curve based on sinusoidal model, applying a MAAT of -5.5°C and an amplitude of A = 16°C.

2.4.2 Snowfall

Synthetic snowfall P_s at time step t is generated applying periodically repeating Gaussian pulses such that

$$P_s(t) = A \cdot \exp\left(-\frac{\mathrm{mod}\,(t_s - t_{0,s} + 0.5d, d - 0.5d)^2}{\sigma^2}\right) \tag{30}$$

where A is the amplitude of the function, the coefficient d defines the gap between two Gaussian peaks (with d = seconds per year), $t_{0,s}$ is the offset in seconds between the beginning of the year and the position of the Gaussian peak, and σ describes the characteristic width of the pulse, meaning the snowfall duration. σ is denoted as

$$\sigma = \frac{Time}{2 \cdot \mathrm{erf}^{-1}(0.99)} \tag{31}$$

applying the inverse of the error function at the 99th percentile. In that way the time limit defined for σ corresponds to the 99th percentile of the function's integral. A given characteristic width ($Time$ in days converted to seconds) thus results in an adaptation of the amplitude A such that the integral below the curve matches the prescribed total annual snowfall P_s. σ is used to study the effects of the distribution of the snow curve on the ice temperatures. A volume conversion of P_s into snow is conducted by applying equation (19). Additionally, to study the effect of an early or delayed snowfall season, the parameter $t_{0,s}$ is constructed, representing a shift in the snowfall peak in days from the beginning of January. To approximate realistic snowfall patterns, a map of mean annual snow water equivalent (SWE) in Switzerland was derived from the MeteoSwiss spatial

climate analysis dataset (Reference period: 1961-2017) (MeteoSwiss 2014a; MeteoSwiss 2014b). This dataset comprises gridded daily precipitation and temperature data. Snowfall was determined by integrating these datasets, considering precipitation as snow only when the air temperature at a specific grid point fell below 0°C. The cumulative snowfall for each year was calculated, and subsequently, an average was computed based on these values. The results of this analysis are depicted in Figure 11.

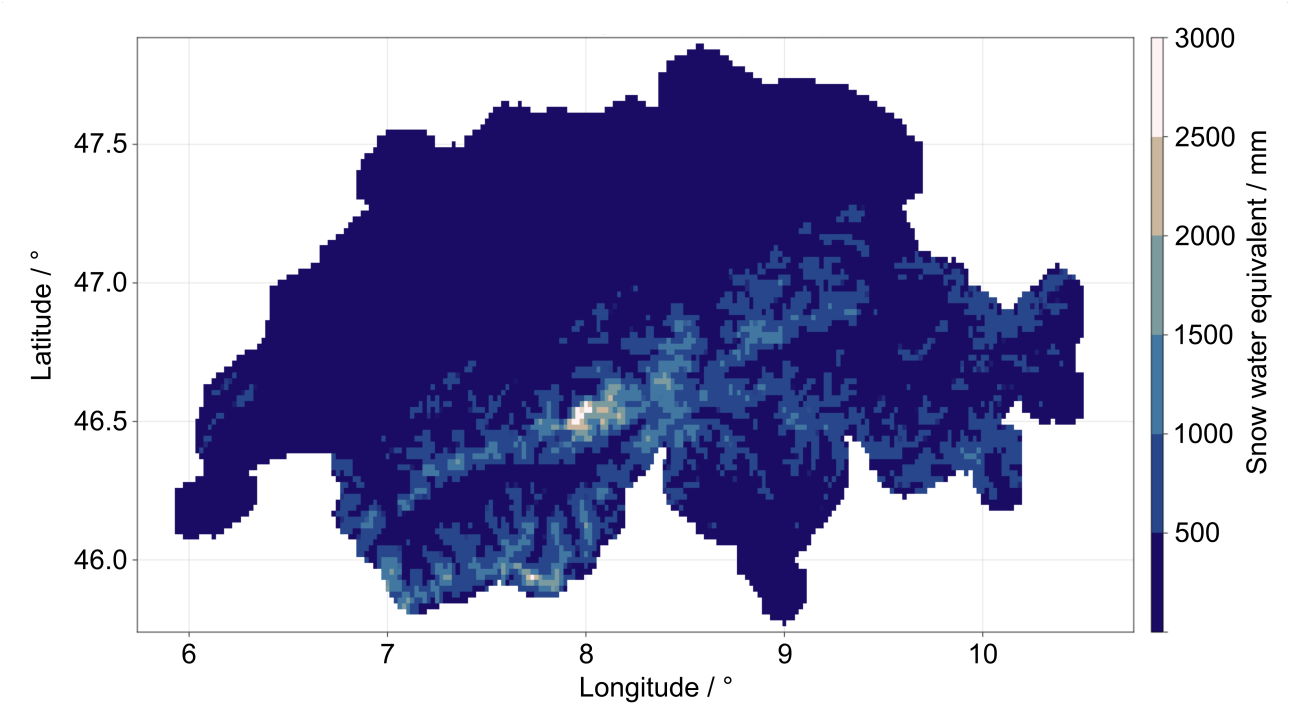

Figure 11: Switzerland's mean annual snow water equivalent (1961-2017) based on MeteoSwiss gridded precipitation and air temperature data (MeteoSwiss 2014a; MeteoSwiss 2014b). Precipitation was counted as snow only when air temperatures dropped below 0°C.

This approximation aims to ensure that the precipitation model broadly aligns with the observed snowfall ranges within the Swiss Alps. However, in order to reduce the amount of model runs with very high snow accumulation which would eventually be sorted out given the prescribed threshold, P_s was capped at a maximum of 2 m a^{-1}. On the basis of these results, a parameter range for P_s of 0.5, 1.2 and 2.0 m w.e. a^{-1} is applied. For the snowfall duration σ a range of 150, 250 and 350 days is applied. $t_{0,s}$ is varied between -60, 0 and 60 days ± 1st of January. Firn cannot be generated by the model, as compaction is not yet implemented. However, the effect of the loss of an initial firn cover is examined by applying a range of parameters for f_z at 0, 5 and 10 m.
Within the default parametric setting a value of P_s = 0.5 m w.e. a^{-1}. Furthermore, the glacier was initialized without any firn. The default snowfall duration is set to 250 days, roughly representing the snow season at an elevation of 2500-3000 meters above sea level (MASL). $t_{0,s}$ was adjusted such that the snowfall peaks at the beginning of February, aligning with studies suggesting a shift of the snowfall peak towards the beginning of the year (Klein et al. 2016). Using the prescribed parametric setting results in the default annual snowfall curve as seen in figure 12.

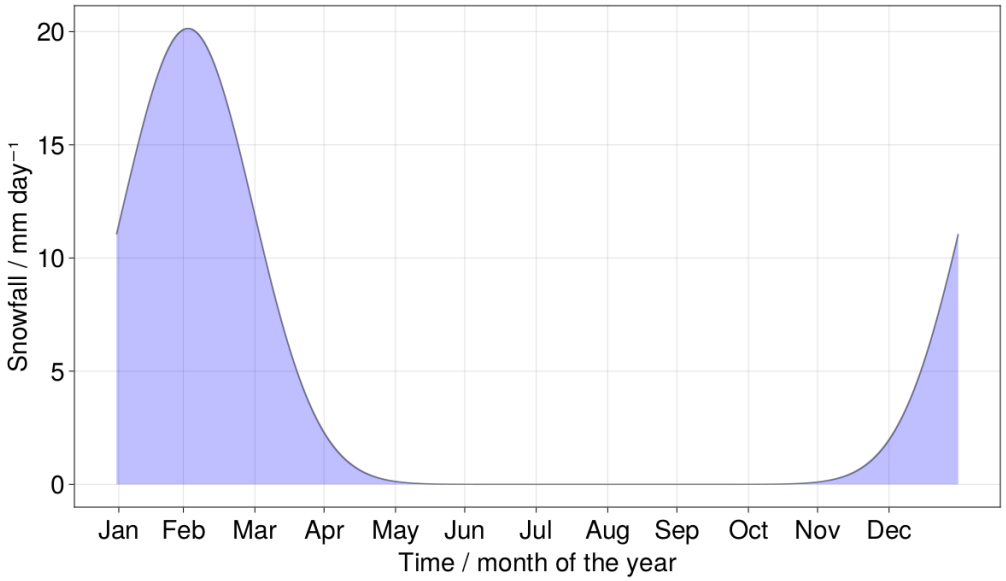

Figure 12: Annual snowfall resulting from the default parametric settings with a total snow accumulation volume of 0.5 m SWE and assuming a total number of 250 snowfall days.

2.4.3 Water volume fraction (ϕ)

Observations regarding water content (ϕ) within temperate and polythermal ice remain limited. Existing measurements have predominantly focused on medium to large valley glaciers or ice sheets rather than the very small glaciers examined in this study (Lüthi et al. 2002). Furthermore, many of the existing observations stem from the polar regions (Moore et al. 1999; Macheret and Glazovsky 2000; Lüthi et al. 2002; Benjumea et al. 2003), with only a few observations within the Alps (Zryd 1991). Additionally, variations in methodologies used to deduce water content have led to a wide range of observed values (ranging from 0.0% to 9.1%) (Pettersson et al. 2004). Establishing definitive patterns representative of specific glacier types in terms of the spatial distribution of water along the glacier profile remains challenging. Hence, a fixed value for ϕ along the entire glacier profile has been chosen. Although this approach might not comprehensively capture the complex effects of water on the ice temperature evolution, it provides an estimation of the overall significance of water within the ice column in predicting the glacier thermal state. Based on the existing observations, a parameter range for ϕ has been selected, encompassing values of 1%, 3%, and 5%.

Table 4 presents a comprehensive summary of all parameters, categorized into the three parameter groups: (1) Surface energy budged, (2) Snow, (3) Water volume fraction. This table includes the ranges applied and the default settings utilized throughout the two-dimensional exploration of the parameter space.

Table 4: Parametric settings used within the parameter study. Depicted are the default values as well as the ranges applied. The different parameters are subdivided into three groups, those affecting the surface energy budget, the snowfall and the water volume fraction.

	Default Setting	Ranges			Description
		I	II	III	
Surface energy budget					
MAAT / °C	-5.5	-3	-5.5	-8	Mean annual air temperature
α_s	0.65	0.4	0.65	0.9	Snow albedo
Snow					
P_s / m w.e.	0.5	0.5	1.25	2.0	Total annual snowfall
σ / days	250	150	250	350	Total annual days of snowfall
$t_{0,s}$ / days ± 1 Jan	0	-60	0	60	Deviation of the snowfall peak
f_z / m	0	0	5	10	Initial firn thickness
Water volume fraction					
ϕ_0 / %	1	1	3	5	Water volume fraction

2.4.4 Tested output variables

Three output variables are tested using the parametric ranges prescribed in table (4): the maximum recorded depth of the CTS (CTS_{max}), the annual CTS propagation rate (CTS_{prop}) as well as the minimum temperature at 10 meters depth ($T10_{min}$). The three variables serve as indicators of how much cold ice can be generated within the modelling time range and thus as a proxy for the state of a the transition from temperate to polythermal or cold conditions. However, the absolute values of CTS_{max} and CTS_{prop} need to be interpreted with caution, as they are both heavily dependend on the initial definition of the CTS as indicated in section (2.1.4). The 10 meter ice temperature is used as an additional proxy, as long-term temperature trends are considered to dominate over seasonal temperature fluctuations within this depth (Cuffey and Paterson 2010; Huss and Fischer 2016).

2.5 Applications on very small Swiss glaciers

In addition to the sensitivity study presented in section 2.4, a dual-track approach is used to identify very small Swiss glaciers (< 0.5 km^2) that tend to transition from temperate to polythermal or cold conditions. First, a detailed reanalysis of ice temperature modelling data, generated in the framework of a study by Huss and Fischer (2016), has been conducted. In their study, they modeled the evolution of all Swiss glaciers smaller 0.5 km ^{2} from 1961 to 2014 with GERM on the basis of a MeteoSwiss gridded data set (MeteoSwiss 2014a). The second approach focuses on replicating the GERM results for a subset of 20 selected very small glaciers using IceT. This replica uses the same

meteorological input data set as GERM while calibrating the mass balance model of IceT against the GERM mass balance output. Alongside enhancing our comprehension of the spatial distribution of very small polythermal glaciers in Switzerland, this replicative study serves as a means to assess IceT's practical application on real glaciers.

2.5.1 GERM geostatistical reanalysis

Huss and Fischer (2016) conducted point wise modeling of englacial temperatures at three distinct locations on each of the glaciers within their data set. These locations were chosen to broadly represent the accumulation area, the ablation area, and the equilibrium line altitude. Ice temperatures at 3,6,10 and 20 meters depth are modeled. A reanalysis of this data set is performed by clustering all glaciers based on their orientation, slope, and elevation using a geostatistical analysis conducted with QGIS software. Glacier outlines, slope, elevation and orientation are drawn from the 2016 Swiss Glacier Inventory (SGI) (Linsbauer et al. 2021). The assignment of the respective model outputs in GERM to the SGI is accomplished using the SGI-ID. For the orientation, 4 clusters are generated: North facing (aspect = 315-45°), East facing (aspect = 45-135°), South facing (aspect = 135-225°) and West facing (225-315°) glaciers. For the slope, clusters have been generated using the median slope of the glacier. Glaciers are subdivided into groups with a median slope <= 15 °, 15-25°, 25-35° and >35°. For the elevation, three clusters are generated for glaciers <= 2000 meters above sea level (MASL), between 2000 and 3000 MASL and between 3000 and 4000 MASL, again using the median elevation. It has been deliberately decided to use the median within the cluster analysis, to avoid biases due to extreme values. 10 meter ice temperature averages have been computed selectively for each glacier and then averaged over the subsets. The 10 meter data point has been chosen, as long-term temperature trends are expected to dominate over seasonal temperature fluctuations within this depth. It is thus used as a proxy for the glacier transition from temperate to polythermal conditions.

2.5.2 IceT

IceT has been re-run using the same MeteoSwiss dataset utilized by Huss and Fischer (2016), specifically targeting a subset of 20 glaciers from this data set. The selection process for the modeled glaciers prioritized those with a documented hazardous record, utilizing the inventory of dangerous glaciers (Raymond et al. 2003). Furthermore, glaciers where ice temperature observations are available, like Glacier du Sex Rouge, St. Annafirn or Vadret dal Corvatsch were preferred. Modeled glaciers are listed in table 5, together with their hazardous record as well as whether ice temperature observations are apparent.

Table 5: Overview of modeled glaciers with IceT. The hazardous record for the individual glaciers is based on the inventory of dangerous glaciers (Raymond et al. 2003).

Glacier	Hazardous Record	Ice Temperature Observations
Altelsgletscher	Yes (Ice avalanche)	No
Birchgletscher	Yes (Ice avalanche)	No
Chesselfirn	No	No
Chessjengletscher SE	No	No
Chlinegletscher	No	No
Chüebodengletscher	No	No
Eiger Hängegletscher Westgrad	Yes (Cerrac fall)	Yes
Glacier du Sex Rouge	No	Yes
Gutzgletscher	Yes (Ice avalanches)	Yes
Hangendegletscher	No	No
Hangfirn	Yes (Ice avalanche)	Yes
Lavaz West	No	No
Ofentalgletscher	No	No
Plattalva	No	No
Pointes de Mourti	No	Yes
St. Annafirn	No	Yes
Vadret d'Arlas	No	No
Vadret da l'alp Ota	No	No
Vadret dal Corvatsch	No	Yes
Weisshorn West	Yes (Cerrac fall)	No

Following successful mass balance calibration against GERM, the maximum CTS depth CTS_{max} occuring throughout the 1961-2014 time series is computed for each of the glaciers. IceT is run using the physical constants for ice and water 1 and on the basis of the surface energy balance model prescribed in section 2.1.2 and the associated physical constants for the radiation model (Tab. (2)). The default model dimensions (refer to Tab. 3) are employed. In contrast to the parameter study, where various values for the englacial water content were explored, ϕ is uniformly set to 0 across the entire glacier profile. This choice is substantiated by the lack of knowledge about the englacial water content of the 20 modeled glaciers. CTS_{max} is used as it is most suitable to assess the probability of a polythermal structure evolving within the glacier. Furthermore, a normalized CTS value $n(CTS)$ is generated within the data set to enhance comparability among individual values. $n(CTS)$ is denoted as

$$n(CTS) = \frac{\text{Glacier specific value}}{\text{Maximum value of all glaciers}} \tag{32}$$

IceT produces point-values on the basis of 1 km grid cells for precipitation and temperature

(adjusted to the elevation by a local lapse rate) utilizing the meteorological input dataset of Huss and Fischer (2016). Calibration against GERM mass balances downscales these values to the glacier-specific scale. However, since calibration is performed using GERM's glacier-wide mass balance output, IceT's resulting output represents averaged values for the entire glacier, disregarding small-scale topographical variations. Consequently, it is unable to distinguish the ice temperature evolution among specific zones like the accumulation area, equilibrium line altitude, or ablation area. Nonetheless, these averaged values can be used as a benchmark for identifying polythermal glaciers when compared to others in the data set.

3 Results

3.1 Parametric study

3.1.1 Full parametric analysis

Given the 7-dimensional parameter space (3 values per parameter), a total number of 3^7=2187 simulations have been produced, from which 567 (ca. 26%) were excluded due to too positive mass balances. The output of the remaining 1620 simulations was used for further analysis. Cross correlations between the 7 parameters, as well as the output variables: CTS_{max}, CTS_{prop} and $T_{10,min}$ have been computed. Additionally the net annual mass balance has been computed for each run, in order to analyse it's influence on ice temperatures. The results are displayed in figure 13. The Pearson R^2 correlation coefficients are presented, with colors indicating whether they are positive (blue) or negative (red). Annotations are applied only to correlation coefficients with R^2 values greater than or equal to 0.1, while lower correlations are considered insignificant and are thus not highlighted. Correlation coefficients between ±0.1-0.3 are considered weak, correlation coefficients ±0.3-0.49 are considered moderate and correlation coefficients >= 0.5 are considered high. The matrix will be described chronologically, from top to bottom starting with parameters affecting the surface energy budget.

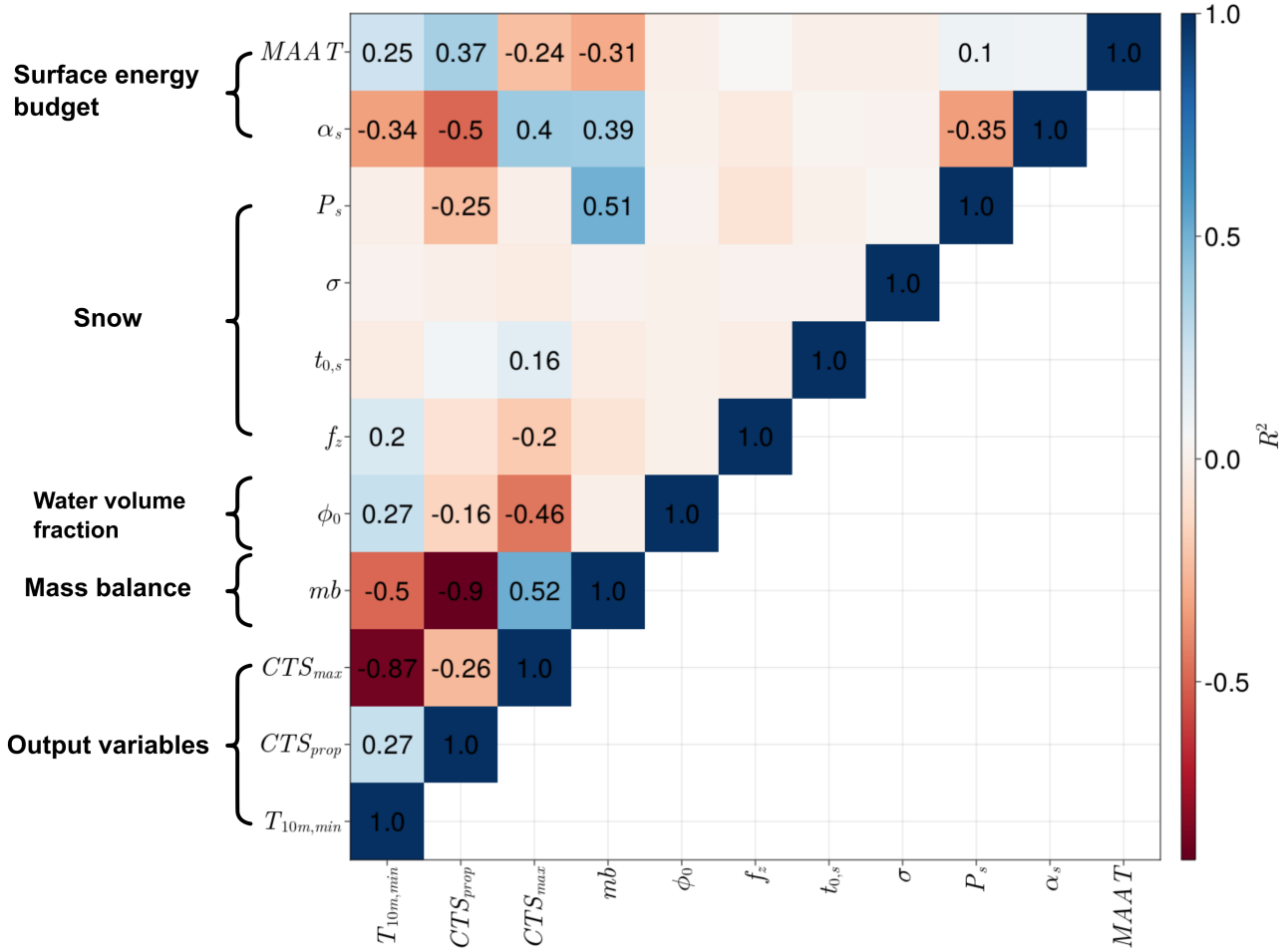

Figure 13: Correlation matrix depicting all cross correlations between the 7 parameters, the net annual mass balance, as well as the 3 output variables CTS_{max},CTS_{prop} and $T_{10m,min}$. The parameters are structured according their type: $MAAT$ and α_s (Surface Energy Budget), P_s,σ,$t_{0,s}$,f_z (Snow),ϕ_0 (Water volume fraction).

The mean annual air temperature $MAAT$ shows a weak positive correlation with $T_{10m,min}$ (R^2=0.25), a weak negative negative correlation with CTS_{max} (R^2=-0.24) and a moderate positive correlation with CTS_{prop} (R^2=0.37). The snow albedo α_s shows a moderate negative correlation with $T_{10m,min}$ (R^2=-0.34), a strong negative correlation with CTS_{prop} (R^2=-0.5) and a moderate positive correlation with CTS_{max} (R^2=0.4). Only two of the 4 snow specific parameters show relations to the output variables. The total number of snowfall days σ as well as the snowfall peak deviation from January, show no correlation with the three output variables apart from a weak positive correlation between $t_{0,s}$ and CTS_{max} (R^2=0.16). The total annual snowfall P_s, depicts a weak negative correlation to the annual CTS propagation rate CTS_{prop} (R^2=-0.25). The initial firn thickness f_z shows a weak positive correlation to $T_{10,min}$ (R^2=0.2), and a weak negative correlation to the CTS_{max} (R^2=-0.2). The water volume fraction ϕ correlates with all three output variables. A weak positive correlation with $T_{10,min}$ can be observed (R^2=0.27), as well as a weak negative correlation to CTS_{prop} (R^2=-0.16). Furthermore, a moderate negative correlation to the maximum CTS depth CTS_{max} can be observed (R^2=-0.46). By far the highest correlation coefficients can be observed for the net annual mass balance mb, with a strong negative correlation to $t_{0,min}$ as well as

a strong negative correlation to the CTS propagation rate CTS_{prop} (R^2=-0.9). Furthermore, a strong positive correlation between the mass balance and the maximum depth of the CTS CTS_{max} can be observed.
As already mentioned in section 2.4, model runs with significant positive mass balances (>3 m w.e.) were systematically excluded from the analysis, since snow compaction is not yet implemented within IceT. Some of the coefficients need thus to be interpreted with caution. This applies particularly to the snow specific parameters P_s as well as the snow albedo α_s. Runs where both α_s and P_s are high generate markedly positive mass balances and are thus omitted from the data record. This bias is supported by the moderate negative correlation between α_s and P_s (R^2=-0.35).

To better grasp the relative importance of the parameters in predicting the evolution of the CTS and thus the ice temperature distribution, a linear regression model was utilized. For the sake of clarity, parameters that exhibited negligible impacts (Coef. < 0.1) on CTS_{max} or were statistically insignificant (p > 0.05) are not displayed. This applies to the parameters: σ and $t_{0,s}$. Table 7 depicts the regression coefficients and the statistical output for the prediction of the maximum CTS depth CTS_{max}. The regression coefficient represents the estimated change in the dependent variable CTS_{max} for a one-unit change in the predictor variable (the respective parameters), assuming all other variables in the model are held constant. Highlighted are the most dominating coefficients (bold). The mean annual air temperature depicts a small positive regression coefficient (=0.14), indicating that an increase in temperature leads to a small increase in the maximum CTS depth. The albedo depicts a more dominant negative coefficient (=-2.16). The same applies to the total annual snowfall P_s, depicting a negative coefficient (=-1.53). However, the results for α_s and P_s are most likely an artefact of sorting the output data and are thus greyed out. A small negative coefficient (=-0.26) can be seen for the initial firn thickness f_z. The most substantial impact on the maximum CTS depth CTS_{max}, is attributed to the water volume fraction ϕ. According to the linear model, a mere 1% increase in ϕ results in a substantial decrease of -165.07 m in the maximum CTS depth.This effect is in accordance with the correlation matrix where ϕ and $_{max}$ depict a relatively high negative correlation (R^2=-0.46). On the contrary, an increase of the net annual mass balance mb by 1 m (w.e.) results in an increase of CTS_{max} by 2.37 m. A counter intuitive effect, as negative mass balances are usually related to stronger cooling of glaciers (Huss and Fischer 2016). However, this outcome might be biased, as strong negative mass balances are accompanied by significant losses of cold ice at the surface, consequently leading to a reduction in the maximum CTS depth.

Table 6: Regression Coefficients and Statistics for the prediction of the maximum CTS depth CTS_{max} for $MAAT$, α, P_s, f_z,ϕ and mb.

Name	**Coef.**	**Std. Error**	**t**	**p**	**Lower 95%**	**Upper 95%**
(Intercept)	29.61	1.62	18.26	0.0^{***}	26.43	32.79
$MAAT$ / °C	0.14	0.07	2.09	0.04^{*}	0.01	0.27
α_s / 0-1	**-2.16**	1.02	-2.13	0.03^{*}	-4.15	-0.17
P_s	**-1.53**	0.12	-13.09	0.0^{***}	-1.76	-1.3
fz	-0.26	0.02	-11.39	0.0	-0.3	-0.21
ϕ / %	**-165.07**	5.53	-29.88	0.0^{***}	-175.91	-154.23
mb / m w.e.	**2.37**	0.11	21.14	0.0^{***}	2.15	2.59

In order to get a better understanding of the development of the CTS, independent from ice losses at the surface, the CTS propagation rate CTS_{prop} can be utilized. CTS_{prop} can be interpreted as the downwards directed rate of cooling in meters per year, and is less dependent on glacier losses due to melt. The output of the linear regression model for the prediction of CTS_{prop} from the seven parameters (+ mass balance) can be seen in table 7. The snow specific parameters σ, $t_{0,s}$, f_z, as well as $MAAT$ are not listed, as their influence was either statistically insignificant (p > 0.05) or negligible (Coef. < 0.1). Rows containing the results of systematically biased parameters like α_s and P_s are again greyed out. The mean annual air temperature shows a small positive effect on CTS_{prop} (=0.04). The most significant coefficient can be again observed for ϕ. According the the linear model an increase of ϕ of 1% decreases the CTS propagation rate CTS_{prop} by -13.85 m a^{-1}. Remarkably, the impact of mass balance on CTS propagation appears to differ from its effect on the maximum CTS depth. Elevating the annual net mass balance by 1 meter of water equivalent (w.e.) leads to a decline in the CTS propagation rate by -0.66 m a^{-1}. This aligns with the correlation matrix findings (Fig. 13), highlighting a strong negative correlation between mb and CTS_{prop} (R^2=-0.9). To put it differently, reducing the mass balance by 1 m (w.e.) results in a rise in the CTS propagation rate by 0.66 m a^{-1}. Considering these opposing effects of mass balance on the output variables CTS_{max} and CTS_{prop}, an equilibrium state seems to exist, favoring the formation of cold ice. This equilibrium state necessitates a balance between excessively negative mass balances leading to considerable cold ice loss due to glacier melt and overly positive mass balances causing a cooling effect buffered by meltwater within the snowpack.

Table 7: Regression Coefficients and Statistics for the prediction of the annual CTS propagation rate CTS_{prop} for $MAAT$, α, P_s, ϕ and mb

Name	**Coef.**	**Std. Error**	**t**	**p**	**Lower 95%**	**Upper 95%**
(Intercept)	3.57	0.17	20.79	0.0^{***}	3.23	3.9
α_s / 0-1	**-0.41**	0.11	-3.84	0.0^{***}	-0.62	-0.2
P_s	0.16	0.01	12.92	0.0	0.14	0.18^{***}
ϕ / %	**-13.85**	0.58	-23.7	0.0^{***}	-15.0	-12.71
mb / m w.e.	**-0.66**	0.01	-55.51	0.0^{***}	-0.68	-0.64

3.1.2 Parameter space slicing

On the basis of the in section 3.1.1 presented findings, 2-dimensional slices of the parameter space have been generated for parametric combinations of particular interest. The model outputs for CTS_{max} and CTS_{prop} were drawn individually from each model run. Apart from the 2 selected parameters, all other parameters are kept constant at the default settings (Tab. 4). This default setting serves as a reference and will thus first be presented.

Figure 14 illustrates the temporal evolution of the ice temperature, the water volume fraction, and the glacier state for the default scenario. Furthermore, figure (15) depicts the snow depth, the ice temperatures at 3, 6, 10, and 20 meters, and the cumulative mass balance. Notably, the default glacier settings exhibit strong negative mass balances, evident in the cumulative mass balance plot (Fig. 15).The glacier looses around 5 m (w.e.) each year given a maximum snow depth of 0.6 m (w.e.). Ice thickness reduces from 70 meters initially to around 10 meters within 10 years (Fig. 14) C). Figures 14A and 14B provide a more direct visualization of the CTS evolution (indicated by the dashed turquoise line), which can be estimated from the interface between the 0% to >0% regions on the water content profile. For the area at ϕ = 0% all water is effectively frozen and the ice can be assumed cold, while for the area at ϕ > 0%, pore water is still available. The ice can thus be considered temperate. The ice temperature record depicts a shallow cold ice layer at the surface, which seems in steady state with the occurring melt rate after around 2 years of simulation time. However, seasonal variations in the ice temperature record as well as the CTS depth can still be observed. The maximum temperature within the frozen surface layer reaches around -0.5 °C in summer whereas it cools down to -5°C in winter. This is more directly detectable in the temperature sensor record (Fig. (15) B) with the 3 meter sensor depicting a minimum englacial temperature of ca. -4 °C. The ice at this rather shallow depth is still seasonally temperate. The maximum CTS depth during the model run is around 8 meters.

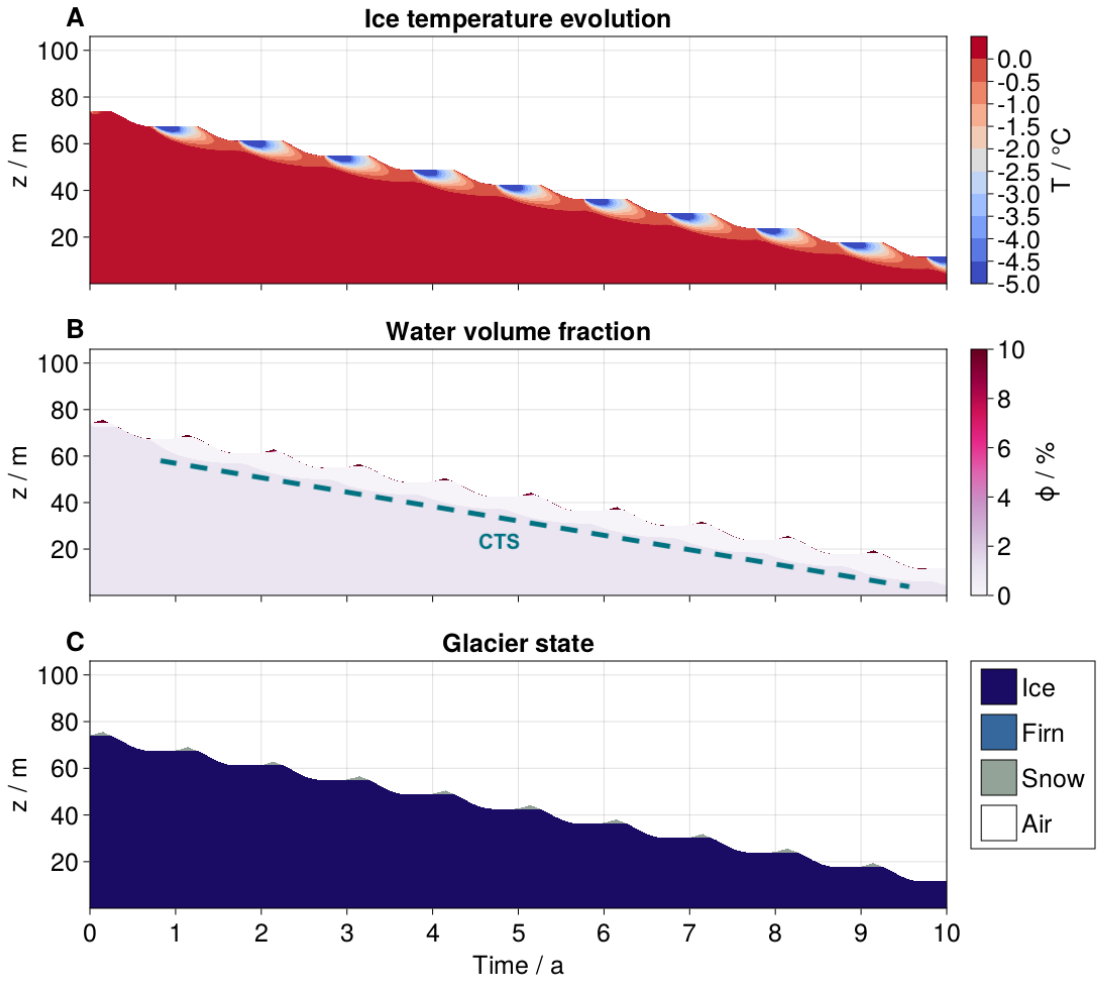

Figure 14: Modeled glacier profile evolution plotted against time using the default parametric setting as prescribed in table 4. (A) Ice temperature evolution, (B) Water volume fraction ϕ together with the approximate location of the CTS, (C) Glacier state.

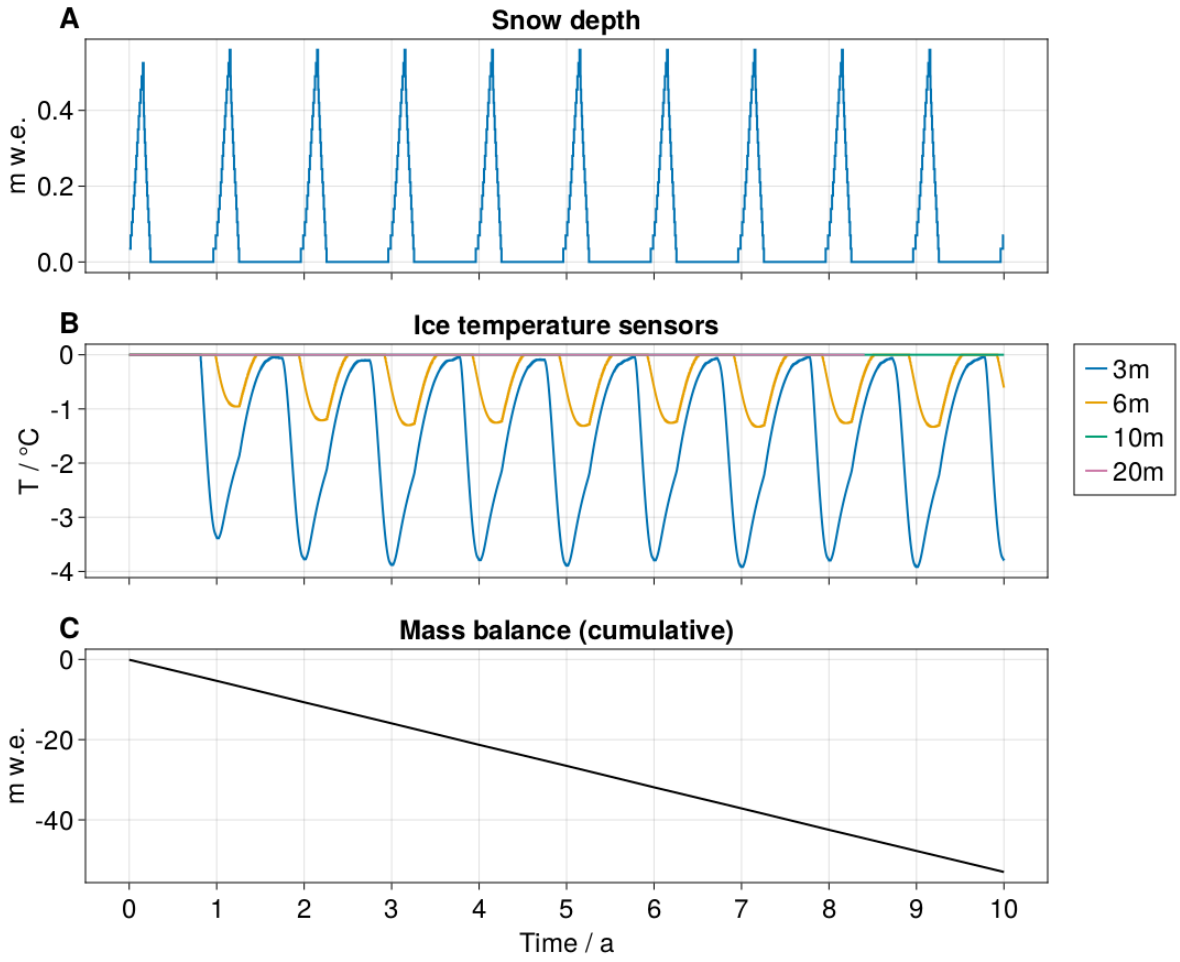

Figure 15: Modeled glacier profile evolution plotted against time using the default parametric setting as prescribed in table 4. (A) Ice temperature evolution, (B) Water volume fraction ϕ together with the approximate location of the CTS, (C) Glacier state. The profile further represents scenario 3 depcited in figure 16.

Using the default scenario as a starting point, parametric slices for P_s,α_s,$MAAT$ against ϕ have been generated. The water content ϕ is used as a baseline, as it exhibited the most prominent effects on both CTS_{max} and CTS_{prop} (Sec. 3.1.1). P_s and α_{snow} are the most influential parameters in determining mass balance, which has been proven to be an important predictor for the CTS evolution, and are therefore also subject to further analysis. Furthermore, $MAAT$ is investigated as it depicted relatively high correlations to all three output variables. The results are illustrated using 2-dimensional heat-maps, where each grid cell represents the results of one individual model run, colored either according to the maximum CTS depth found throughout the run (turquoise) or the annual CTS propagation rate (blue). Figure 16 shows the outcomes for P_s against the water content ϕ. Depicted are both the results for CTS_{max} (A) and CTS_{prop} (B). A negative effect of ϕ on both output variables can be observed, however the effect is much more present for CTS_{max} as opposed to CTS_{prop}. An increase in the CTS_{max} with increasing annual snowfall can be observed (A) with the strongest cold ice penetration of 20.8 meters, given a mean annual snowfall of 2 m (w.e.) and a water content of ϕ=1%. The lowest CTS depth of 4.2 m is reached at P_s=0.5 m (w.e.) and ϕ=5%. On the contrary, the effect seems to inverse when it comes to the annual CTS propagation

rate CTS_{prop}, where less snowfall results in an increase in CTS_{prop}, with a maximum of 6.87 m a^{-1} reached for the P_s=0.5 m (w.e.) and ϕ=1% and a minimum of 4.24 m (w.e.) reached for P_s=2.0 m (w.e.) and ϕ=5%. Considering the strong positive relations between snowfall and mass balance (R^2=0.51) these findings are in accordance with the results from the linear regression model (see 3.1.1). Melt dominated glaciers with very strong negative mass balances destroy more cold ice as can be generated, resulting in smaller depths of the CTS. However, when controlling for the surface melt and explicitly considering the CTS propagation itself, thus reducing the dependencies on a single interface, the picture reverses and less snowfall leads to an increase in the CTS propagation rate.

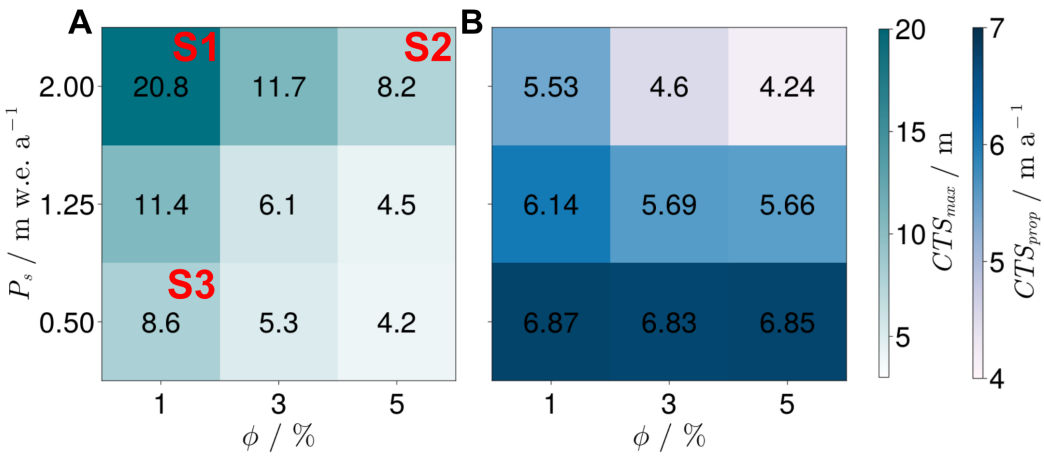

Figure 16: Heatmaps colored according to the maximum depth of the CTS as well as the annual CTS propagation rate for the parameter range of the total annual snowfall (P_s) against the water volume fraction ϕ_0. Each square represents the results for one individual model run applying the given parametric combination, while all other parameters are drawn from the default parametric setting (Tab. 4). S1-S3 mark exemplary selected scenarios to further illustrate their ice temperature evolution and can be seen in figure 17, 18. S1 represents the parametric combination of the default scenario plotted in 14.

To further confirm these findings, three parametric combinations (S1-S3) have been selected, plotting their glacier evolution against time. The parametric combinations for those scenarios are marked in red on figure 16. Figure 17 depicts the temporal evolution of the ice column given the scenario S1 with high snowfall (P_s=2.0 m w.e.) and low water content (ϕ=1%). As apparent from the ice temperature evolution, despite experiencing consecutive negative mass balances, the CTS propagation rate exceeds the surface melt. Moreover, as opposed to the default scenario (Fig. 14), the CTS depth seems to not yet have reached steady state and the cold surface layer is able to steadily grow throughout the model run. Seasonal warming is apparent as well but is not sufficient to counteract the increase in the CTS depth.

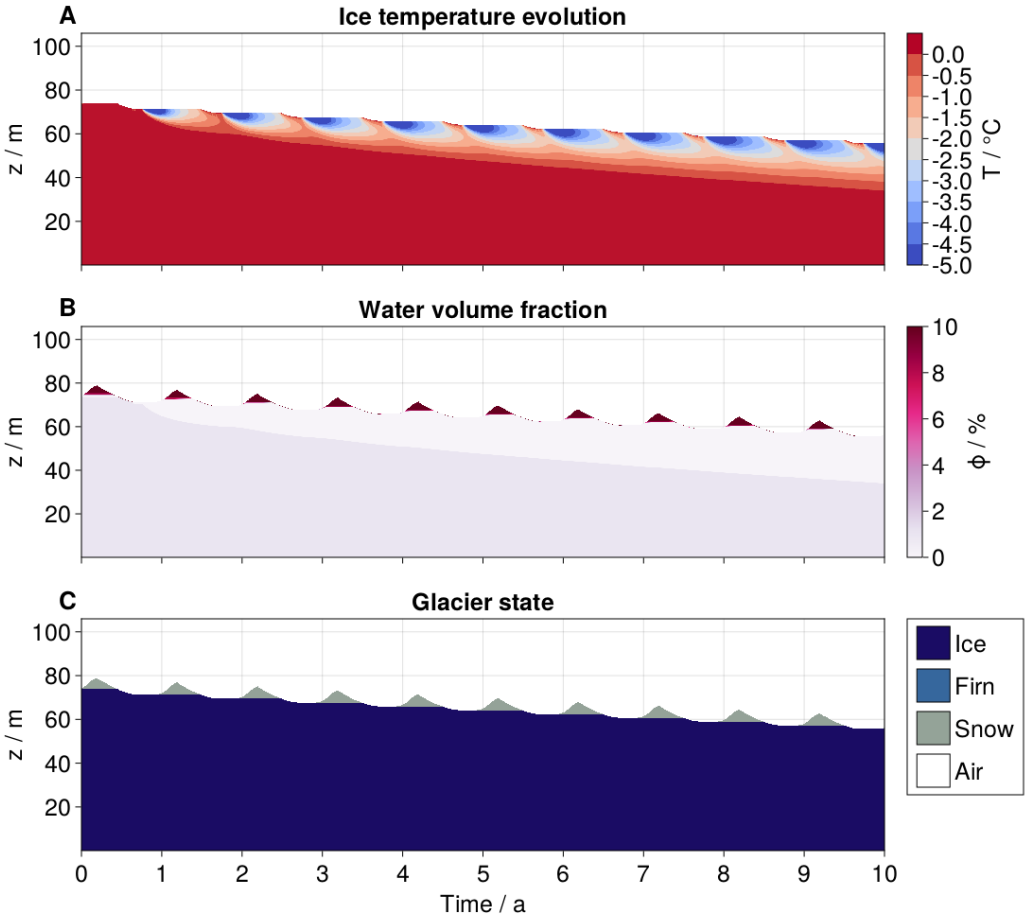

Figure 17: Modeled ice temperature evolution for the parametric settings S1 depicted in figure 16, with high snowfall (2.0 m w.e. a^{-1}) and low water content (1%).

Figure 18 depicts the temporal evolution of the ice column for the scenario S2, given the same amount of total annual snowfall (P_s=2.0 m w.e.), however with substantially more water along the glacier profile (ϕ=5%). The water exerts a significant buffering effect on the cold temperature penetration. After the initial spin-up phase where the CTS propagation rate is relatively high, as apparent from the quick evolution of a small cold ice layer at the surface, further development of this layer is significantly slowed down. At the end of the 10 years simulation the cold ice depth seems to approximate steady state with the climatic forcing. Due to the slow CTS propagation rate, the glacier can be assumed to disappear before developing a pronounced polythermal structure.

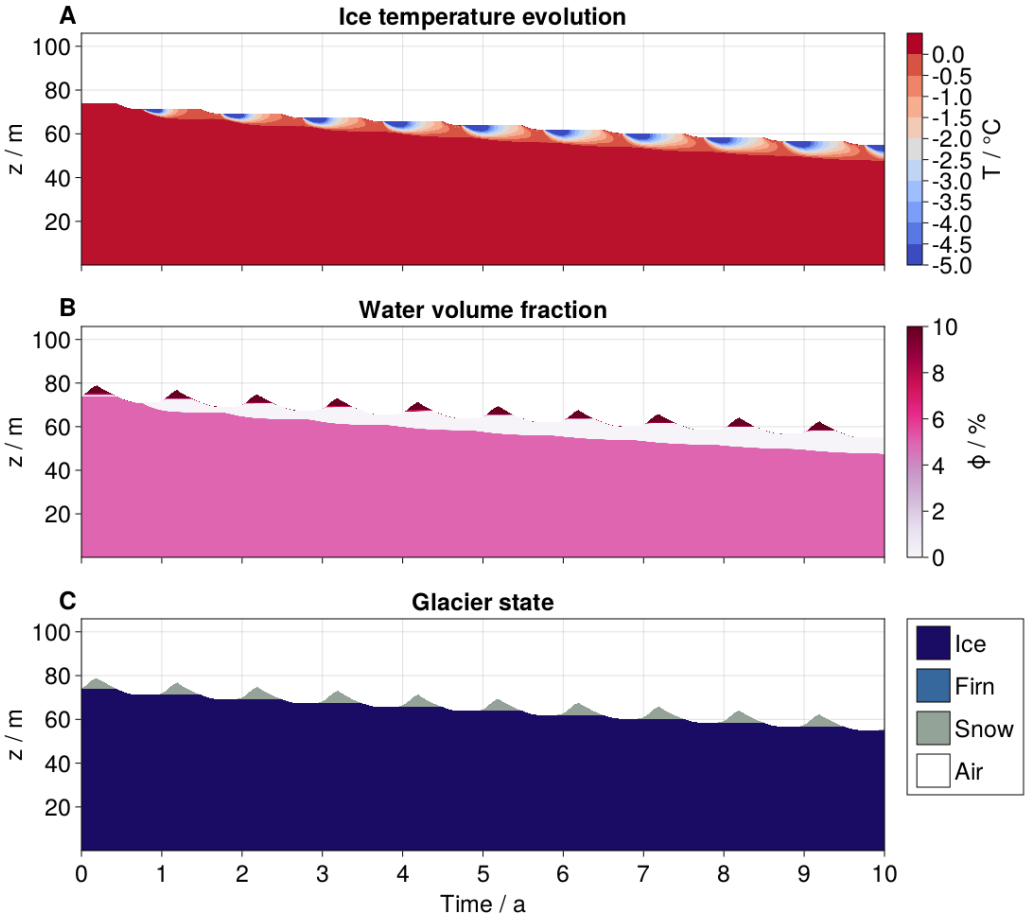

Figure 18: Modeled ice temperature evolution for the parametric settings S2 depicted in figure 16, with high snowfall (2.0 m w.e. a $^{-1}$) and high water content (5%). Note the evident mitigation of cooling within the glacier owing to the increased englacial water content.

Finally, scenario S3 represents the exact parametric combination as in the default setting (Fig. 14). In this case the total annual snowfall is at it's lowest (P_s=0.5 m w.e.) while the water content is equal to that in scenario S1 (ϕ=1%). In this case melt dominates over the CTS propagation and a steady state is already reached after 2 years.

Figure 19 depicts the results for the two surface energy budget determining parameters $MAAT$ and α_s. Results for CTS_{max} and CTS_{prop} are again showcased. As expected, lower mean annual air temperatures increase the maximum depth of the CTS, however the effect appears to be relatively small with the maximum CTS depth of 12.4 m (w.e.) reached for $MAAT$=-8.0°C and ϕ=1% while the minimum CTS depth of 3.9 m (w.e.) is generated at $MAAT$=-3.0°C and ϕ=5% (19A). A substantial difference in the annual mean air temperature of 5°C results in a variation of only 8.5 meters. Interestingly the effect reverses for the CTS propagation rate where the maximum of 7.04 m a^{-1} is observable for $MAAT$=-3°C and ϕ=1%, whereas the minimum of 5.33 m a^{-1} can be observed for $MAAT$=-8.0°C and ϕ=5% (19B). For the snow albedo the thickest CTS depth can be observed for α_s=0.9 and ϕ=1% while the minimum CTS depth is generated for α_s=0.4 and ϕ=5% (19C). Opposite effects can be again observed for CTS_{prop} with a maximum of 7.0 m a^{-1} for α_s=0.4 and ϕ=1% while

the minimum of 4.08 m a^{-1} is generated for α_s=0.9 and ϕ=5%. Similarly to P_s, these diverging effects are likely due to the positive relationship between the snow albedo and the mass balance, as evident from the correlation matrix (Fig. 13) (R^2=0.39).

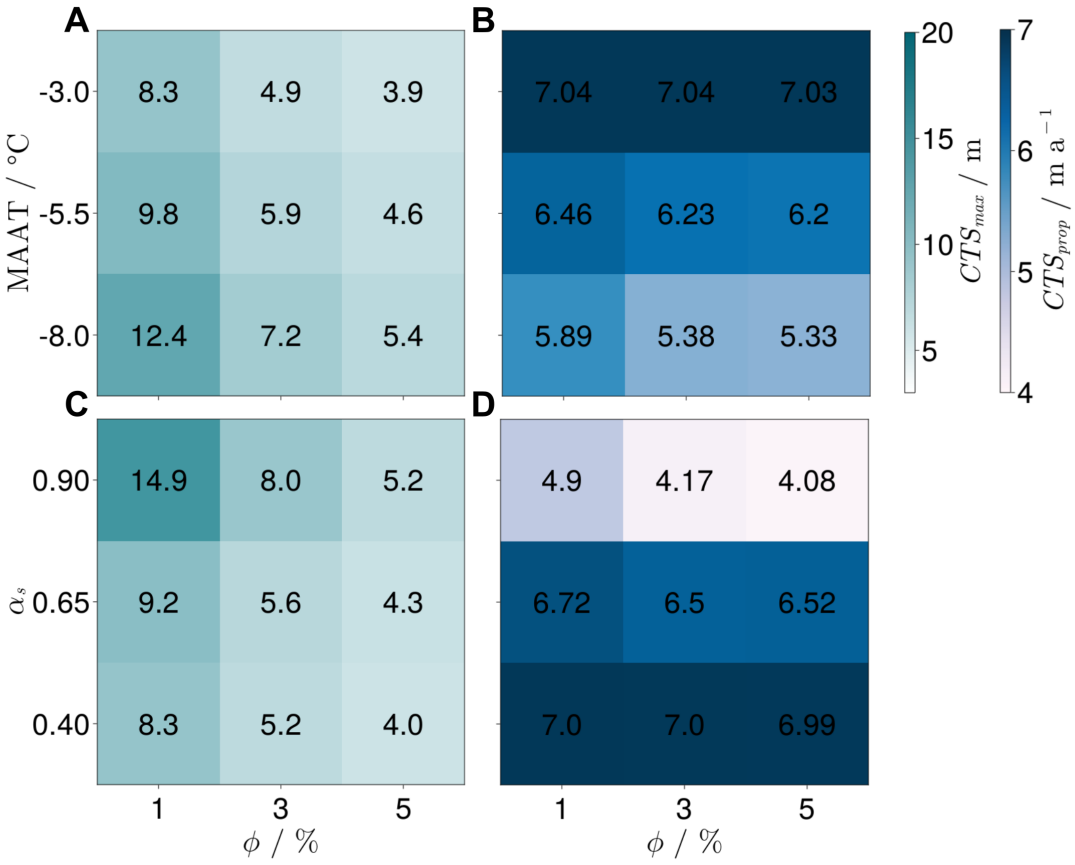

Figure 19: Heatmaps colored according to the maximum depth of the CTS as well as the annual CTS propagation rate for the two parameters controlling the surface energy budget, the mean annual air temperature (A,B) and snow albedo (C,D). Each square represents the results for one individual model run applying the given parametric combination, while all other parameters are drawn from the default parametric setting (Tab. 4). Displayed are the results for

Upon closer examination of the six heatmaps, it becomes evident that the influence of water content on both variables determining CTS is more exponential than linear in nature. For example, keeping the snowfall at a constant P_s=2.0, the jump in CTS_{max} between ϕ = 5% and ϕ = 3% is 11.7-8.2 = 3.5 m, while the same reduction in water content between 3% and 1% almost doubles CTS_{max} by 20.8-11.7=9.1 m. A similar picture emerges for CTS_{prop}. However, the data suggests a maximum upper limit for CTS_{prop} of approximately 7 meters per year.

3.2 Applications on very small Swiss glaciers

Predicting the spatial occurence of polythermal ice within Switzerland is challenging, as englacial temperatures are the result of long-term climatic conditions. Both model uncertainties as well as uncertainties within the forcing data occur, leading to biases within the model output. Nevertheless,

an attempt is made within this study, studying the output of two methodically different ice temperature models. The results of the GERM geostatistical reanalysis will be first elaborated followed by the model results of IceT.

3.2.1 GERM geostatistical reanalysis

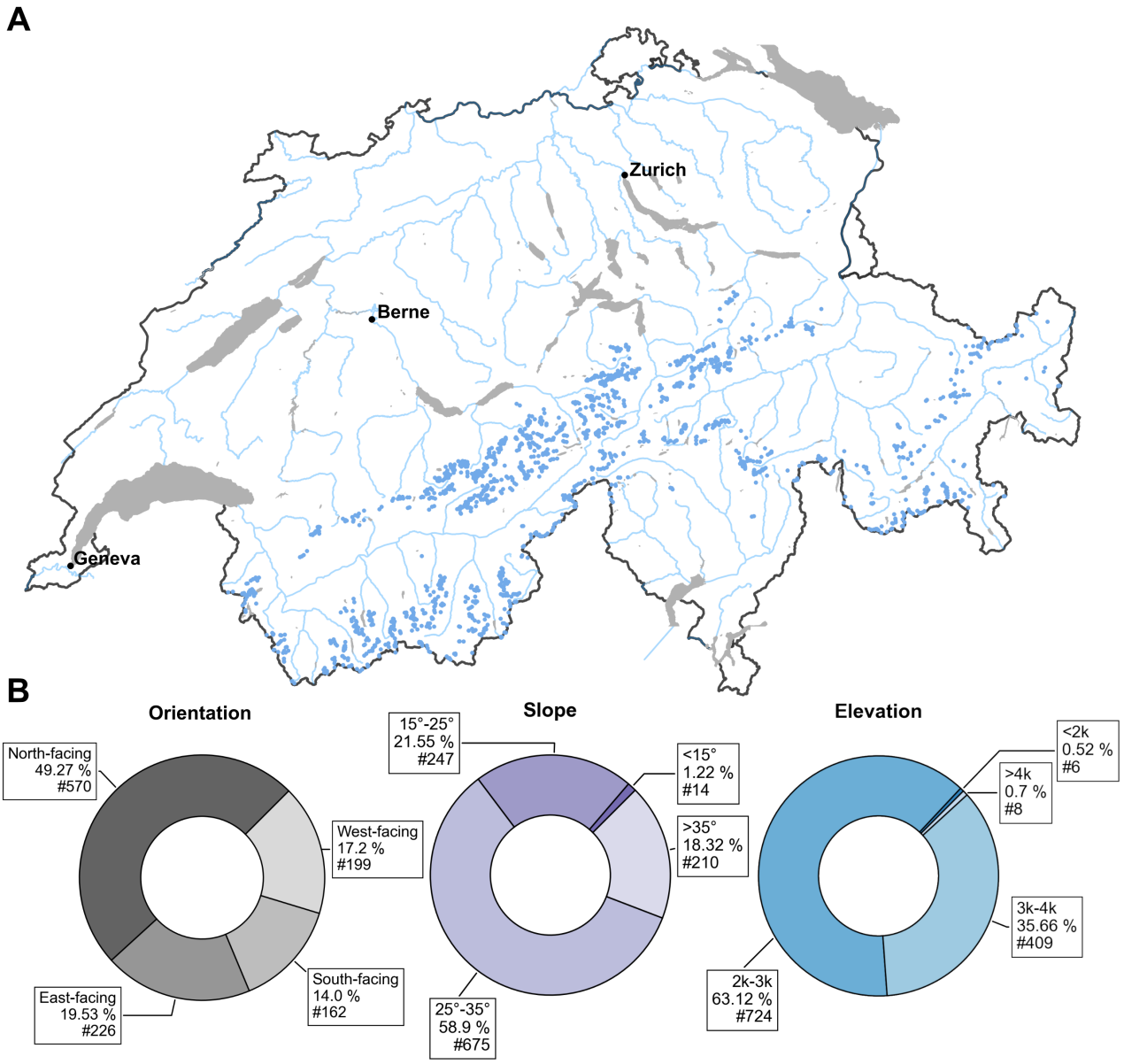

Figure 20: (A) Swiss map displaying the locations of all very small glaciers (< 0.5 km^2) as small blue dots. (B) Pie charts displaying the results of the geostatistical analysis of all glaciers clustered for aspect, slope and elevation. Displayed are the relative percentage as well as the number of glaciers contained within each cluster. The analysis is based on the 2016 Swiss glacier inventory (Linsbauer et al. 2021).

On the basis of the 2016 Swiss glacier inventory (Linsbauer et al., 2021), a geostatistical analysis was conducted on all very small Swiss glaciers (< 0.5 km^2). The dataset underwent clustering based on glacier orientation, slope, and elevation. Figure 20A presents the spatial distribution of these very small glaciers in Switzerland, depicted as small blue dots. In Figure 20B, the clustered data

is displayed. Annotations indicate the relative percentage and total number of glaciers within each cluster. Predominantly, very small glaciers are situated on north-facing slopes (49.27%) and east-facing slopes (19.53%). The majority of these glaciers exhibit a median slope ranging between 25° and 35° (58.9%) and are characterised by median elevations between 2000 and 3000 MASL (63.12%). Few glaciers are situated below 2000 MASL (0.52%) or above 4000 MASL (0.7%).
Restructuring of the GERM data output generated by Huss and Fischer (2016) on the basis of these geostatistical clusters was conducted. The results of this analysis can be seen in figure 21. 10 m averages in the ice temperature are depicted for different data clusters. Figure 21A serves as a reference, depicting the output of all very small glaciers separately for the accumulation area (blue), ELA (dashed gray) and ablation area point (red). The initial ice temperature for the three data points in 1961 is -0.2°C. However, due to the averaging process, the presence of extreme values distorts this value downwards. Most glaciers can thus still be presumed to start at an ice temperature around 0°C. All three points exhibit a long-term cooling trend within the ice temperature. The accumulation area cools least, down to about -0.7°C. The ELA point depicts stronger cooling down to about -1.25°C, while the ablation area point depicts the strongest cooling down to >-1.5°C. Pronounced warming is notable during the 1980s, a period characterized by relatively cold and wet conditions when glaciers received substantial snowfall. Consequently, many glaciers were covered by a thick and water-saturated firn layer, which acted as an insulator, impeding cooling. Overall, the temperature trends for the three data points suggest that the majority of the modelled glaciers with GERM transitioned to polythermal or cold states. However, variations in cooling might be identifiable within the individual geostatistical clusters. To simplify the output, it has been decided to concentrate on the ablation area point within the cluster analysis. Figure 21B-D, therefore, solely reflect the output for the ablation area. All three plots contain the average off all glaciers at that point as a reference. Furthermore, the sample size of each cluster is indicated. The ice temperature evolution for the different orientation clusters can be seen in figure 21B. The ice temperature evolution of north (n=503) and east-facing glaciers (n=80) come quite close to the average value, however ice temperatures for north-facing glaciers are a bit higher towards the end of the time series. South-facing glaciers (n=190) show above average cooling down to -1.75°C by 2014, while west-facing glaciers (n=58) depict the most dominant cooling given a final 10 m average ice temperature of >-2°C. A tendency towards more pronounced cooling can be observed as the slope of the glacier increases (Fig. 21C). The strongest cooling can be observed for glaciers with a median slope >35° (n=188), given a minimum 10 m ice temperature of -2.2°C in 2014. The most prominent deviations from the mean ice temperature evolution, can be observed for the elevation clusters. Glaciers with a median elevation <= 2000 meters above sea level (MASl) show no particular cooling trend throughout the time series. However, the sample size (n=6) is substantially lower than those of the other two clusters. Glaciers between 2000 and 3000 MASL (n=541) make out the biggest fraction, and show below average cooling throughout the time series with a minimum temperature of -1.05°C in 2014. In contrast, glaciers between 3000 and 4000 MASL (n=282) depict above average cooling (the strongest cooling of all clusters) with a minimum 10 m ice temperature of -2.3°C in

2014. The data suggests the presence of an amplitude effect, where higher elevated glaciers tend to show higher amplitudes within the data set as opposed to lower elevated glaciers. This effect is most likely attributable to increasing orographic precipitation during cold and wet periods such as in the 1980s (Huss and Fischer 2016), where high elevated glaciers received above average snow. Due to illustrative reasons, four Glaciers with a median elevation above 4000 MASL are not showcased, as their cooling trend is two orders of magnitude stronger than the average cooling.

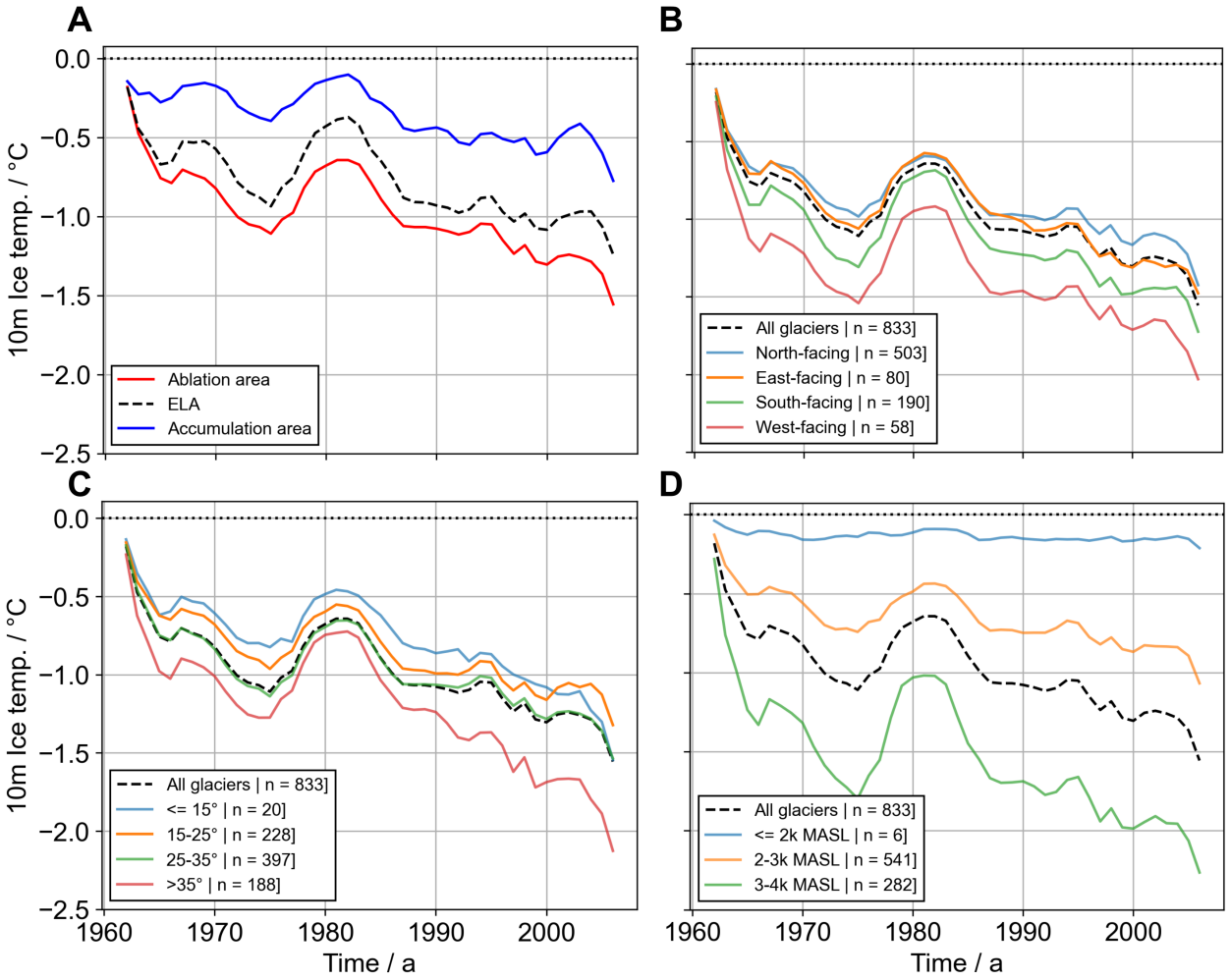

Figure 21: Modeled 10 meter ice temperatures with GERM from 1961-2014. Time series represents averages of (A) all very small glaciers (< 0.5 km^2) within the Swiss Alps for the ablation, ELA and accumulation point, (B) averages plotted for different glacier orientations, (C) averages for different glacier slopes and (D) averages for different glacier elevations.

Figure 21 indicates that by 2014, according to GERM, the majority of the small glaciers in Switzerland exhibit polythermal or cold conditions. To confirm this, temporal snapshots of the dataset for 1980, 1990 and 2000 have been extracted, displayed in figure 22. Evident from the box-plots, both in the ablation area and at the ELA, there is a noticeable decrease in the median 10 m ice temperature. By the early 2000s, 75% of all glaciers exhibited a 10 m ice temperature below -0.5°C. Even within the uppermost 25% of glaciers, temperature ranges between -0.5°C and 0.0°C, suggesting that only a small fraction of all glaciers modeled with GERM exhibit temperate conditions.

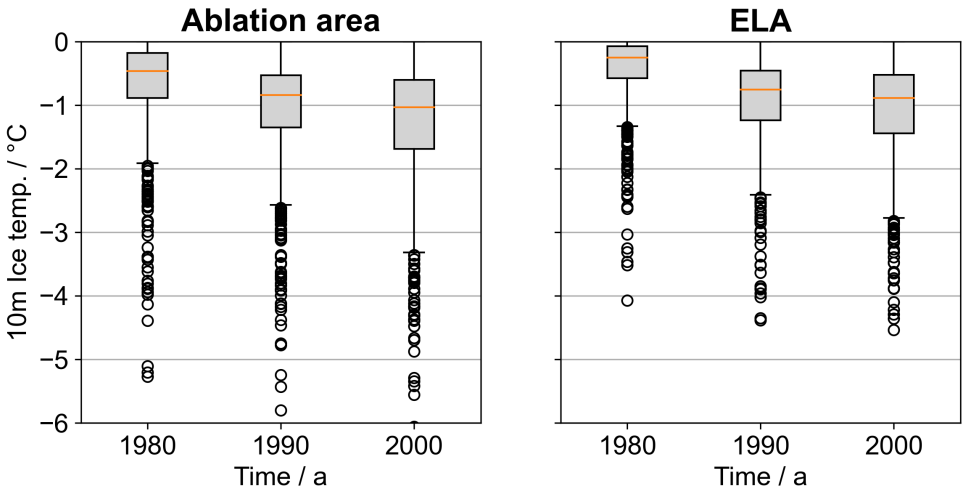

Figure 22: Modeled 10 m ice temperature with GERM. Box-plots display snapshots in time for 1980, 1990 and 2000 in the ablation area and at the ELA.

3.2.2 IceT

Based on the same meteorological dataset utilized in the study by Huss and Fischer (2016), IceT has been run for a subset of 20 very small glaciers (< 0.5 km^2). Fully automated mass balance calibration for each of the 20 glaciers was conducted utilizing the GERM mass balances as a reference (See 2.5.2). The process involved adjusting the incoming shortwave radiation by a correction factor (C_{rad}). A range of calibration factors for C_{rad} between 0.9 and 1.2 (a 25% deviation) effectively replicated the long-term annual mass balance trends obtained from the GERM data set. On the basis of this mass balance evolution, maximum CTS depths that occurred throughout the simulation CTS_{max} were computed for each of the 20 glaciers listed in table 5. The model is initialized without any snow cover, resulting in a significant cooling effect at the beginning of the simulation period, likely overestimating the actual conditions by neglecting snow accumulation from previous years. Consequently, the ice temperature record during the model's initialization (spin-up phase) was not factored in, encompassing the first four years. In addition to CTS_{max}, a normalized CTS value was generated within the data set to enhance comparability among the values. The absolute values of the CTS need to be interpreted with caution, as they are heavily dependent on the definition of the CTS within the model. In IceT, the CTS is defined as the interface where ice temperatures are at or below -0.01°C, and all liquid water within the ice is frozen. Any ice temperatures above this threshold are classified as temperate ice. This definition aligns with existing literature, which predominantly characterizes the CTS based on the absence of liquid water (Pettersson et al. 2004; Gusmeroli et al. 2010). Altering this threshold value can significantly impact the determination of the CTS. However, when compared to each other, the CTS_{max} values serve as an indicator of the probability of encountering a polythermal structure within the 20 glaciers. In order to gain a better perspective on the results, CTS_{max} values were clustered into three groups employing K-means clustering. Figure 23 depicts the maximum depth of the CTS observed in each glacier throughout the simulation period. The glaciers are sorted in ascending order and colored based on their cluster

categories (low, medium, high).

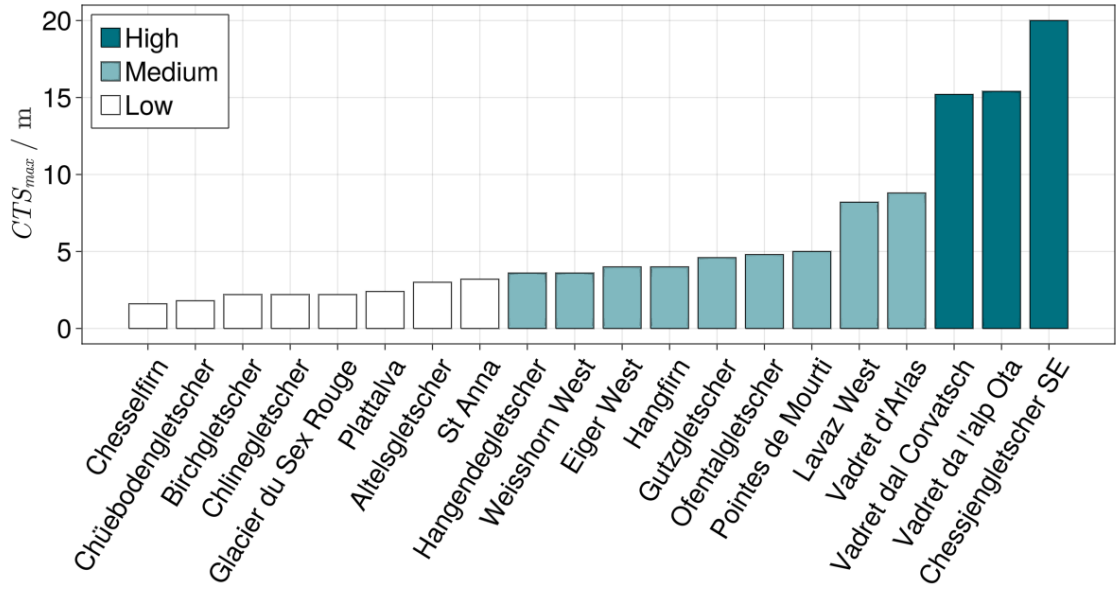

Figure 23: The maximum CTS depth, CTS_{max}, derived from ice temperature modeling for a subset of 20 very small glaciers (< 0.5 km^2). The glaciers have been categorized into three groups (high,medium,low) using k-means clustering and are sorted based on their CTS_{max} values to demonstrate their ranking.

The low cluster contains all glaciers with a CTS_{max} <= 3.6 m, containing Chesselfirn, Chüebodengletscher, Birchgletscher, Chlinegletscher, Glacier du Sex Rouge, Plattalva, Altelsgletscher, St. Annafirn as well as Hangendegletscher. Normalised CTS values range between $n(CTS)$ = 0.08 for Chesselfirn and $n(CTS)$ = 0.16 for St. Annafirn. The model results indicate that these glaciers are predominantly temperate, with the exception of a seasonally frozen surface layer. The second cluster comprises glaciers with CTS_{max} values ranging from 3.6 m to 8.8 m. This group contains Hangendegletscher, Weisshorn West, Eiger West, Hangfirn, Gutzgletscher, Ofentalgletscher, Pointes de Mourti, Lavaz West and Vadret d'Arlas. Normalised CTS values range between $n(CTS)$ = 0.18 for Hangendegletscher and $n(CTS)$ = 0.44 for Vadret d'Arlas. Both Lavaz West and Vadret d'Arlas show notably greater maximum CTS depths, exceeding 8 m. The third cluster exhibits significantly higher maximum CTS depths ranging from 15.2 m to a maximum of 20.0 m. It contains Vadret dal Corvatsch, Vadret da l'alp Ota as well as Chessjengletscher south-east (SE). Normalised CTS values range between $n(CTS)$ = 0.76 for Vadret dal Corvatsch and $n(CTS)$ = 1.0 for Chessjengletscher south-east (SE), which represents the highest value in the data set. Among this limited sample of 20 very small Swiss glaciers, Vadret dal Corvatsch, Vadret da l'alp Ota and Chessjengletscher SE show the highest likelihood for a polythermal structure according to the model. Maximum CTS depths greater then 15 m are reached, a depth that is considered to represent long-term climatological trends as opposed to seasonal temperature variations (Huss and Fischer 2016; Cuffey and Paterson 2010). This observation is especially relevant as the model results present glacier-wide averages. CTS depths in the ablation area, typically experiencing less latent heat transfer due to meltwater in the thin snow cover, are potentially even higher. Figure 24, depicts the spatial distribution of all very

small glaciers across Switzerland (small blue dots) as well as the position of the modeled glaciers (big dots). modeled glaciers are colored turquoise according to the maximum CTS depth generated during the model run. In addition, glacier names are attached depicting the actual value for the CTS depth (turqoise) and the normalised CTS value (grey). Interestingly, a distinct spatial cluster in the south-eastern Engadin emerges among glaciers exhibiting strong indications of polythermal ice. This region is known to experience relatively low precipitation as apparent from the Swiss spatial climate analysis (Fig. 11), which might be one explanation for the model output.

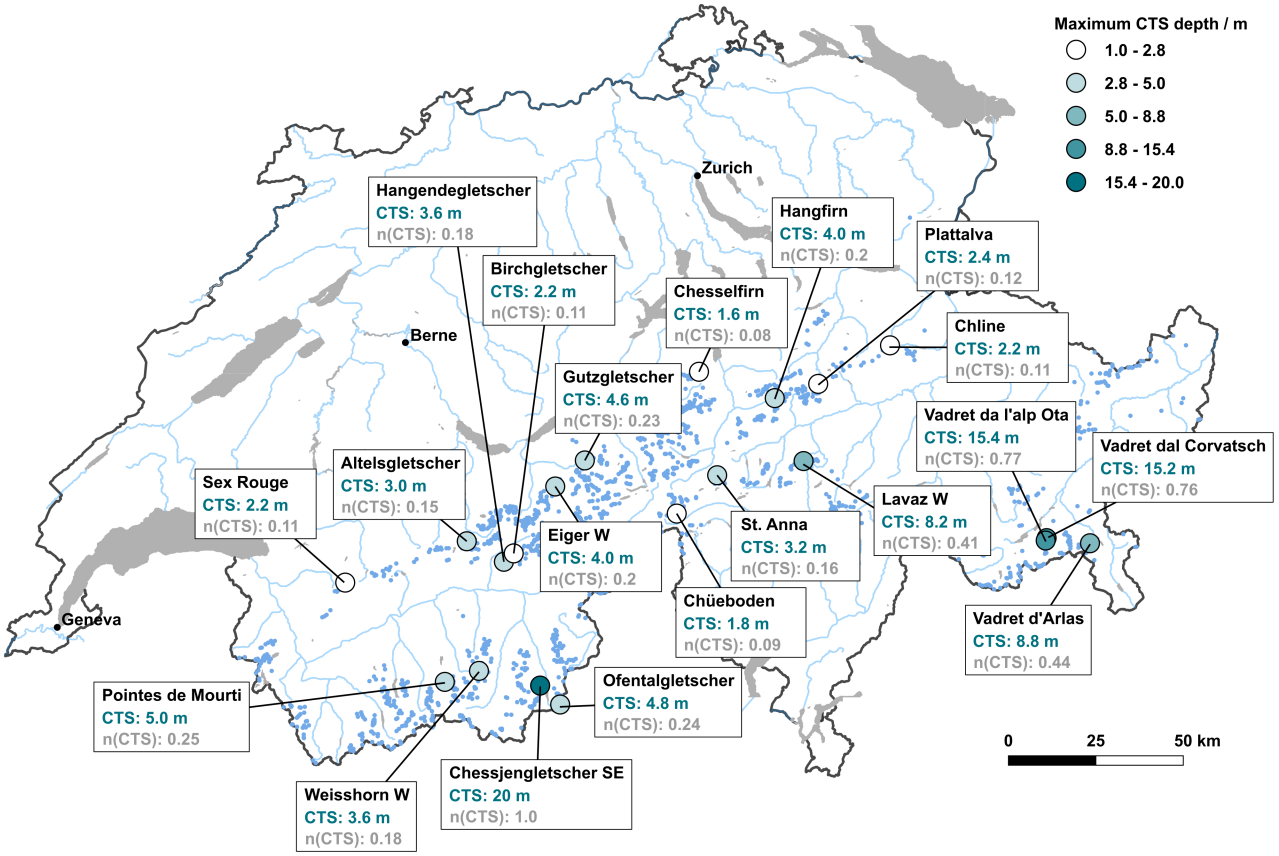

Figure 24: Swiss map displaying IceT model outcomes for a subset of 20 very small glaciers (< 0.5 km^2) utilizing the meteorological dataset of Huss and Fischer (2016). The map displays the locations of all very small glaciers (small blue dots) and the modeled glaciers (larger dots), shaded in turquoise to represent the maximum CTS depth achieved during the modeling process. Additionally, the names of the modeled glaciers, their respective maximum CTS depth values (turquoise), and the normalized CTS value $n(CTS)$ (grey) are provided.

The individual model output for the three glaciers belonging to the highest cluster will be analyzed in greater detail to gain a more comprehensive understanding of their ice temperature evolution. In order to compare the outputs of GERM against IceT, the GERM data acquired at the ELA has been plotted as well. The ELA point was chosen intentionally as it better represents the average thermal condition of each glacier in comparison to the accumulation and ablation area. Figure 25 depicts the modeled ice temperature evolution for Vadret dal Corvatsch at 3,6,10 and 20 m depth. Both results for IceT (Fig. 25A) and GERM (Fig. 25B) are showcased. In addition, the snow depth (computed with IceT) (C) as well as the cumulative mass balance record (D) are plotted, as they've

proven to substantially influence the ice temperature evolution (See 2.4). The spin-up phase, which was not included in the computation of CTS_{max} (1961-1965) is shaded in gray. The ice temperature records of the two models depict substantial differences. Following the spin-up phase, where both models depict relatively negative temperatures, ice temperatures for IceT emerge to temperate conditions staying there until the late 1980s. In contrast, GERM's englacial temperature record depicts much more variance between the 1960s and the 1980s, and a second cooling phase around the mid 1970s, which is not apparent in IceT's temperature record. The 1980s are characterised by relatively high snowfall and positive mass balances resulting, favourable for temperate conditions. However, from the 1990s on-wards, mass balances are much more negative (Fig. 25 D). The GERM ice temperature record indicates a very quick transition towards polythermal conditions with the 20 m ice temperature < 1°C constantly decreasing. IceT captures this trend only, sporadically and indicates repetitive phases of warming, apart from the 21st century where the lowest temperatures in IceT's temperature record can be observed with the 10 m ice temperature reaching down to >0.1 °C.

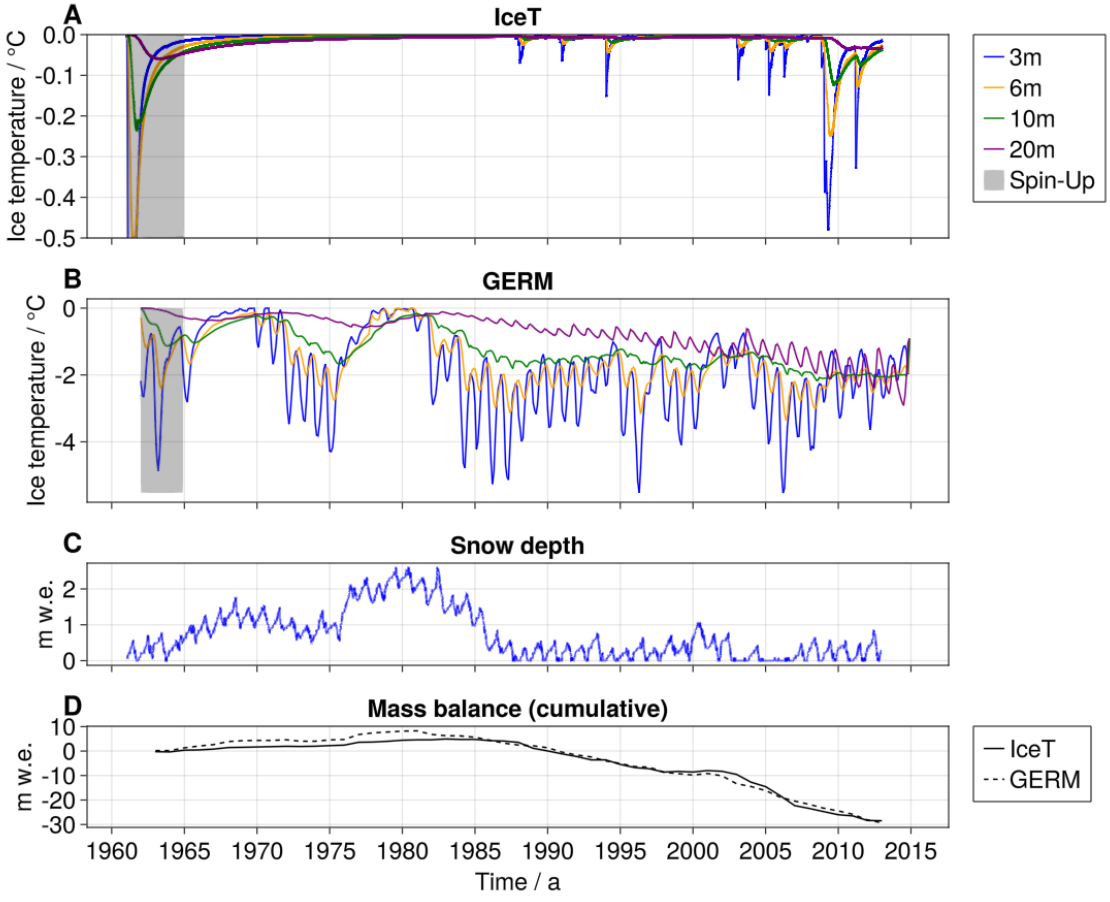

Figure 25: Modeled ice temperatures at different depths for Vadret dal Corvatsch. Modelling results of IceT (A), Model results of GERM for the ELA point (B), modeled snow depth using IceT (C), cummulative mass balances of the two models plotted against each other (D). Please note the distinct y-axis limits between IceT and GERM.

Figure 26 shows the modeled ice temperature evolution for Vadret da l'alp Ota, a glacier located just next to Vadret dal Corvatsch only about 300 meters below on the north-eastern flank of Piz

Murtel. Similarly to Corvatsch the IceT indicates temperate conditions from 1965 till approximately 1990, where a cooling occurs down to -0.2 °C at 3 m depth. The cooling trend in the 2000s, however, appears to be less prominent, with the lowest ice temperature not dropping below -0.1°C. GERM exhibits a closely analogous ice temperature pattern to that of Vadret dal Corvatsch, displaying temperate conditions from 1975 to 1985. Subsequently, it demonstrates sustained cold conditions at depths of 10 and 20 meters from the 1990s onward. Please note that the last years are drawn from the predictive model run, initialised at 0°C, as no temperature record could be found within the data.

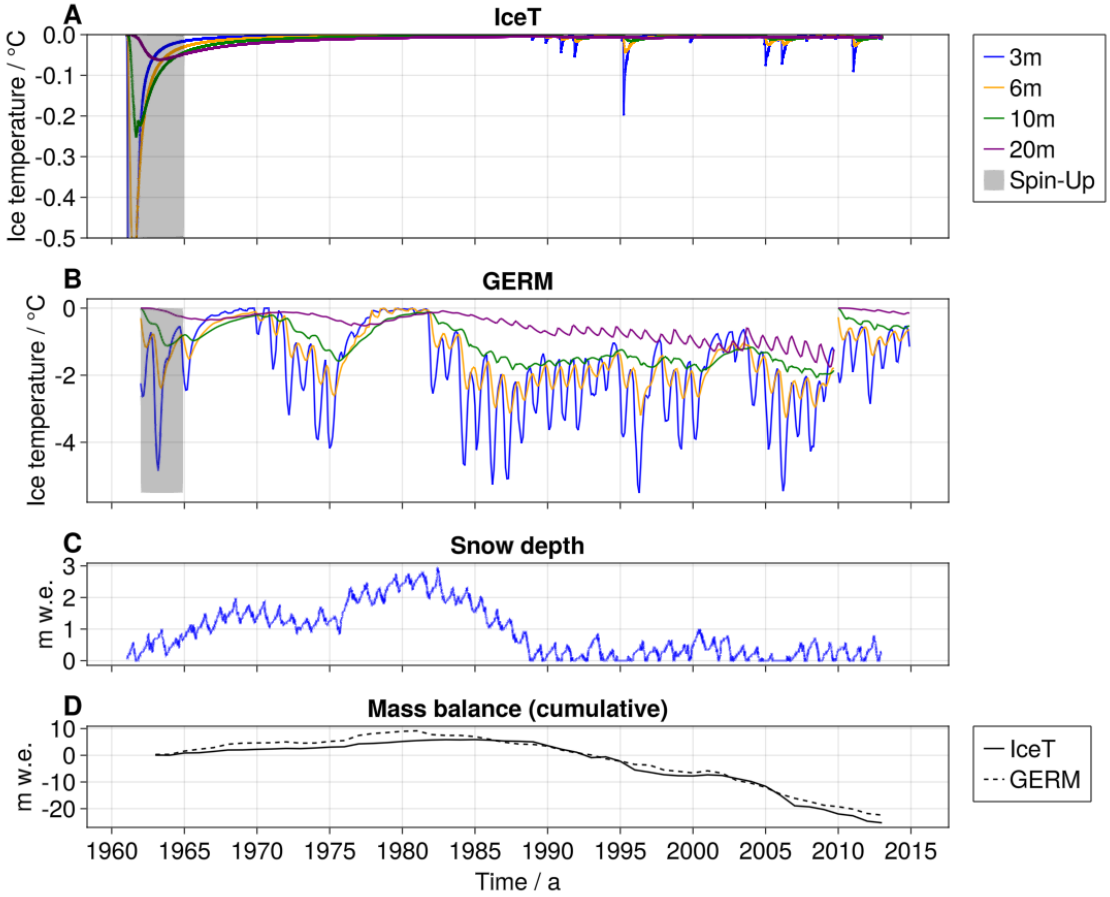

Figure 26: Modeled ice temperatures at different depths for Vadret da l'alp Ota. Modelling results of IceT (A), Model results of GERM for the ELA point (B), modeled snow depth using IceT (C), cummulative mass balances of the two models plotted against each other (D). Please note the distinct y-axis limits between IceT and GERM.

Figure 27 depicts the modeled ice temperature evolution for Chessjengletscher, representing the coldest conditions from all 20 modeled very small glaciers. Following the spin-up phase, both GERM and IceT depict significant cooling, particularly in the 1970s. IceT indicates minimum ice temperatures at 3 m depth of <-1°C and -0.25 °C in 10 m depth around that time. This is followed by a temperate phase between 1975 and 1997. Two distinct cooling periods arise at the end of the 1990s and again around 2005 with minimum temperatures at 3 m depth of -0.7°C. Relating GERMs output to those of Corvatsch and Vadret da l'alp Ota shows that very cold conditions are much more frequent in the 3,6 and 10 m data record. With the exception of a brief warming phase in the late

1970s, the ice temperature at a depth of 10 meters consistently remains below -1°C, whereas for Corvatsch and Ota temperate conditions are reached more frequently at this depth.

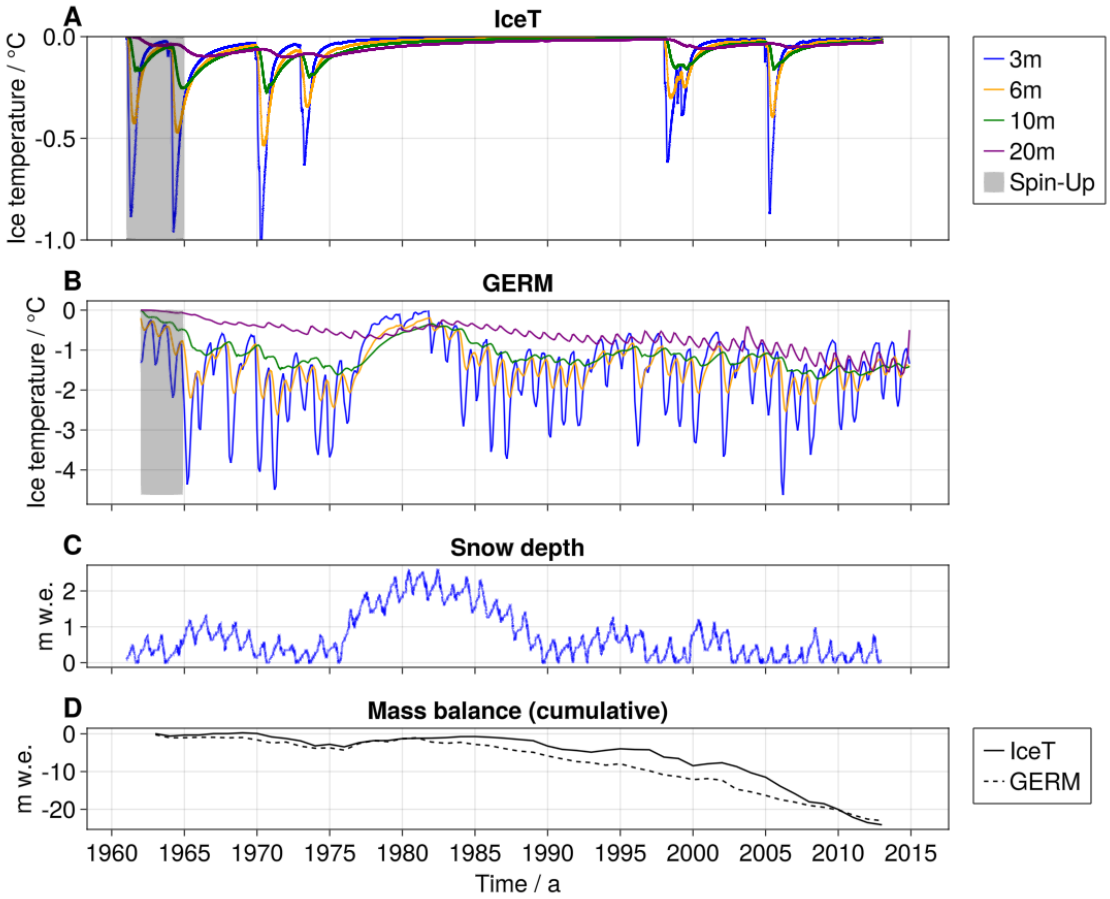

Figure 27: Modeled ice temperatures at different depths for Chessjengletscher SE. Modelling results of IceT (A), Model results of GERM for the ELA point (B), modeled snow depth using IceT (C), cummulative mass balances of the two models plotted against each other (D). Please note the distinct y-axis limits between IceT and GERM.

To create a realistic parallel with the parameter study presented in section 2.4, an additional examination has been conducted on the climatic forcing data of the individual glaciers in relation to the maximum CTS depth CTS_{max}. The scatter plots in Figure 28 illustrate various variables plotted against the maximum CTS depth. These include the mean annual snowfall (Fig. 28A), the average number of snowfall days (Fig. 28B), the mean annual air temperature (Fig. 28C), and the elevation above sea level (Fig. 28D). Glacier specific values are marked with a small cross. Furthermore, Pearson R^2 correlation coefficients are displayed. A significant negative correlation between the mean annual snowfall and CTS_{max} can be observed (R^2 = -0.79, p = 0.0). Corvatsch, L'alp Ota and Chessjengletscher depict the lowest snowfall over the modeled time series of 1961-2014, all of them on average receiving less then 1.0 m (w.e. a^{-1}). For the number of snowfall days no significant correlation can be observed (R^2 = 0.12, p = 0.6). The mean annual air temperature does also not show a significant correlation with CTS_{max} (R^2=-0.14,p = 0.56). For the elevation the correlation is slightly higher, however still not significant (R^2 = 0.27, p = 0.26).

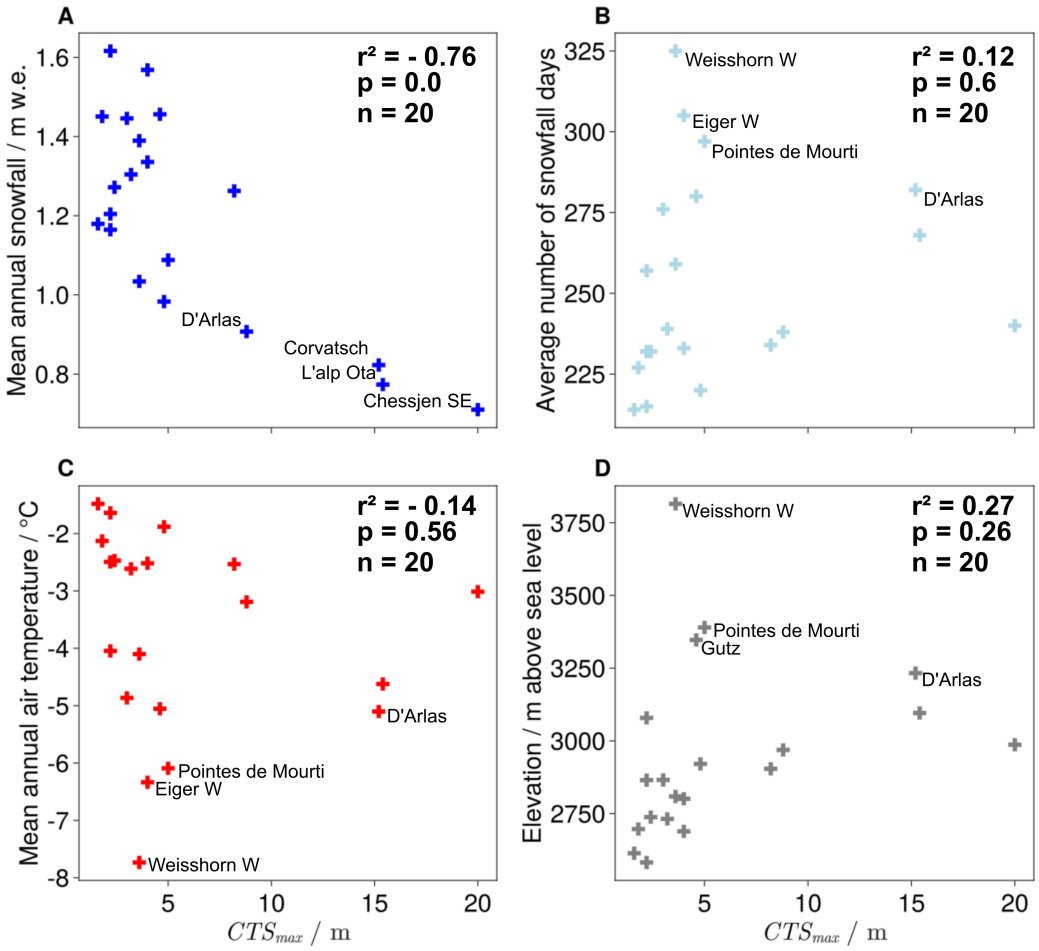

Figure 28: Correlation analysis of glacier characteristics and their influence on the maximum depth of the CTS: Mean annual snowfall (A), Average number of snowfall days (B), Mean annual air temperature (C), Elevation above sea level (D).

3.2.3 Comparison to measured borehole temperatures

In order to evaluate the representativeness of IceT, a comparison with borehole ice temperature measurements is presented for Vadret dal Corvatsch, Glacier du Sex Rouge, and St. Annafirn. Ice temperature measurements on Corvatsch were conducted between 1999 and 2001 by Hager (2002), while measurements on Sex Rouge and St. Anna were carried out by Signer (2014) between 2013 and 2014. All measurements were performed using thermistor chains, reaching depths betwen 13 and 35 meters. The locations of the boreholes on the three glaciers are depicted in figure 29.

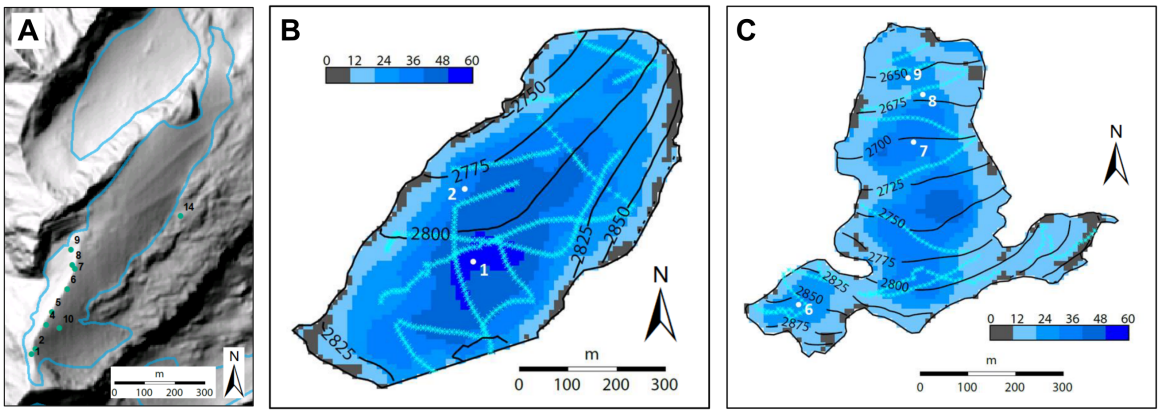

Figure 29: Locations of borehole measurements for (A) Vadret dal Corvatsch by Hager (2002) as well as (B) Glacier du Sex Rouge and (C) St.Annafirn conducted by Signer (2014).

Figure 30A displays the temperature measurements for borehole 5 on Vadret dal Corvatsch, captured at various times throughout the year 2000. The measurements reveal temperatures dropping to -4°C at depths exceeding 12 meters, indicating cold ice. Seasonal fluctuations between -9°C and 0°C are observable in the uppermost 10 meters. In Figure 30B, boreholes 1 (blue) and 2 (green) on Glacier du Sex Rouge are illustrated. Seasonal cooling from the previous winter is visible in the upper 20 meters, with temperatures down to -1.1. However, at greater depths, temperatures remain around -0.05°C, suggesting temperate conditions. Figure 30C showcases boreholes 6 (red) and 9 (blue) on St. Annafirn. There is a considerable disparity in ice temperatures between the two locations. Borehole 6 registers an ice temperature of -1.25°C at 6 meters depth, while borehole 9 records -0.25°C at the same depth.

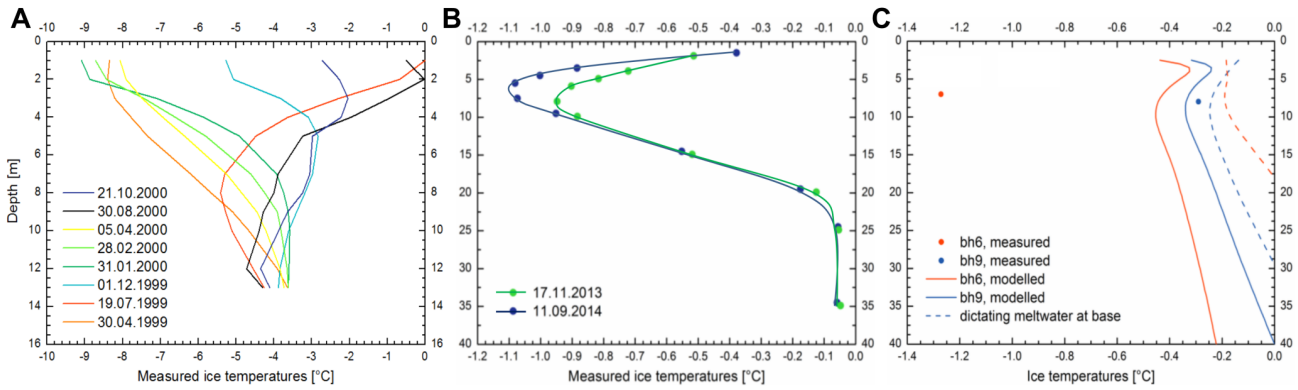

Figure 30: Results of borehole ice temperature measurements for different times for (A) Vadret dal Corvatsch (borehole 5) , (B) Glacier du Sex Rouge (borehole 1 in blue, borehole 2 in green) and (C) St.Annafirn (borehole 6 in red and borehole 9 in blue).

Figure 31 illustrates the modeled ice temperatures for Corvatsch (A), Sex Rouge (B), and St. Annafirn (C). All profiles exhibit ice temperatures above -0.01°C, indicative of temperate conditions. The slight curvature in the profile toward negative values reflects remnants from the preceding cooling period. When compared to the measurements, IceT appears to systematically overestimate the ice temperatures. Moreover, even seasonal variations cannot be detected, as apparent in figure 31A.

This systematic bias is most likely attributable to the strong buffering effect of meltwater contained within the snowpack, inhibiting any significant cooling. The issue will be discussed further in subsequent sections as it holds significant implications for interpreting the modeling results.

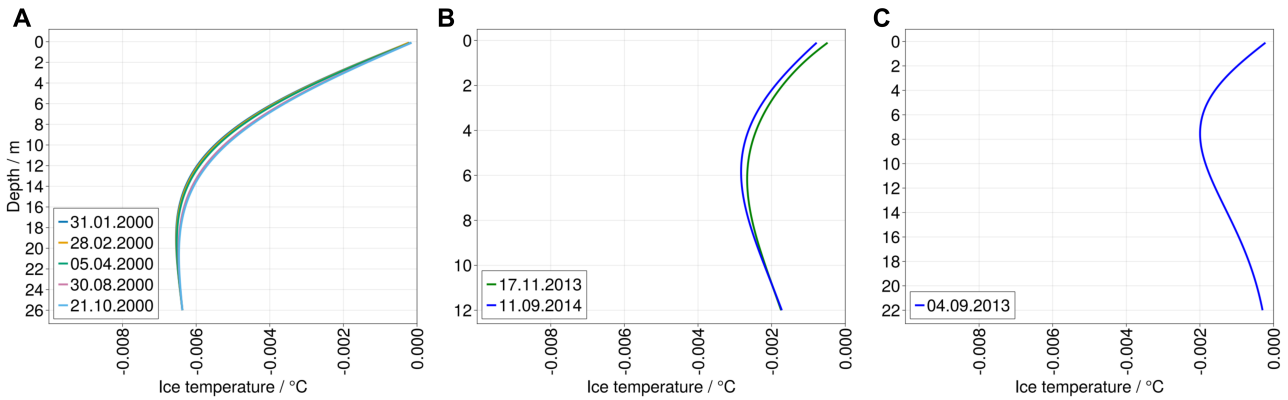

Figure 31: IceT model results for (A) Vadret dal Corvatsch , (B) Glacier du Sex Rouge and (C) St.Annafirn. All three glaciers depict clear temperate conditions. The bending of the temperature curve towards slightly negative temperatures can be interpreted as a remnant of the last cooling period.

4 Discussion

4.1 Model uncertainties

Multiple uncertainties arise when considering the various components of the model presented in this study. To gain a better overview, they are structured into uncertainties related to: (1) The input data, (2) the parameterization, (3) the calibration process, (4) the model structure and dimensionality.

Regarding the input data, it's important to differentiate between synthetic and realistic applications of the model. Within the parametric framework, ice temperature sensitivities were tested using synthetically generated parameter ranges for the air temperature, the albedo, different snow scenarios as well as the water volume fraction. Parametric ranges for the climatic variables were derived from data specifically obtained for the Swiss Alps, aiming to roughly represent the conditions prevalent within Switzerland. This approach is however highly simplified, making it challenging to directly relate certain model outputs to specific glacier settings within the Swiss Alps. Nevertheless, it offers insight into the relative significance of different parameters in determining englacial temperatures and provides information on the temporal and spatial scales of the transition from temperate to polythermal or cold conditions.

Uncertainties in the input data are particularly relevant in the realistic application of the model, as concrete reconstructions of the englacial temperature evolution of specific glaciers were conducted. For simplicity, it has been decided to run the model on a single meteorological data set representing the regional average as opposed to calibrating against geodetic mass balances on the glacier scale, as has been done with GERM (Huss and Fischer 2016). Glacier specific differences in

the surface energy input were accounted for, using the lapse rate corrected air temperatures from the initial GERM data as well as correcting the incoming shortwave radiation using a correction factor C_{rad}. Consequently, the model output presented in this study represents point values for each glacier, portraying the average glacier evolution while concealing local differences. This needs to be considered during the interpretation of the data.

IceT utilizes the enthalpy formulation by Aschwanden et al. (2012), which derives ice temperatures and water content from a thermodynamic look-up table. This approach relies on fundamental physical laws governing the conservation of mass and energy. However, due to certain limitations, a fully physically-based model was not feasible, thus necessitating parameterizations for some of the physical processes. For instance, constant values for the ice and snow albedo are assumed, neglecting non-linear effects that are known to exist within the snowpack (Lehning et al. 2002). A more precise method could involve applying differential equations to model the decrease in the albedo during snow settling, which significantly impacts the surface energy budget.

The comparison with measured borehole temperatures indicates that IceT systematically overestimates ice temperatures. The effect is most likely attributable to the speed of meltwater drainage within the snowpack. Meltwater drainage within IceT only occurs at the uppermost grid cell, as soon as the water content reaches 100%. The remnant melt signal from previous ablation is consequently retained within the snowpack. This leads to significant inaccuracies during periods of extensive snow cover and pronounced surface melt. As evident in figure 31A this might even eliminate seasonal variations in the englacial temperature. It is noteworthy that this bias predominantly manifests in realistic model applications, where substantial daily and seasonal variations frequently cause snowmelt. Within the synthetic model applications (refer to section 3.1), this effect is less pronounced as the sinusoidal air temperature curve, prohibits any snowmelt during the winter months.

As evident in section 2.3, net mass balance trends can be captured quite well, however summer mass balances are systematically overestimated while winter mass balances are underestimated. This is likely an artifact stemming from the fact that GERM applies both corrections on the melt (f_M,$r_{snow/ice}$) as well as the precipitation (C_{prec}). According to the authors, C_{prec} is varied within a range 0.5 to 2.5, therefore the meteorologically given snowfall can be more than doubled. Neglecting this factor can lead to significant underestimations of GERM's winter snowfall while at the same time a reduction in melt occurs as calibration is conducted to match the net annual mass balances. This is presumably also the reason for the overestimation of the summer mass balance. Nevertheless, while snow depths may be underestimated, the timing of the snow cover remains unchanged as the net mass balance trends are accurately captured. In other words, periods when the buffering effect of meltwater within the snowpack diminishes remain the same. The effects on the ice temperature evolution should thus be minimal. This point will be further elaborated in section 4.2.3.

Finally, with IceT being a 1-dimensional model at it's current state, introducing a single boundary at the surface, horizontal heat fluxes are not accounted for. Furthermore, the model doesn't account

for the geothermal heat flux. Ice temperatures are thus likely being overestimated as the glacier thins and approaches its bed.

4.2 Sensitivities of very small Alpine glaciers to thermal regime changes

Among the total of 7 parameters studied, 5 have shown to exert a significant influence on the glacier thermal evolution: The mean annual air temperature $MAAT$, the snow albedo α_s, the total annual snowfall P_s, the initial firn thickness f_z, the annual mass balance mb as well as the water volume fraction ϕ. For reasons of clarity, they were grouped into parameters affecting the surface energy budget, the snow availability & mass balance as well as the water content.

4.2.1 Surface energy budget

Variations in the surface energy input were introduced through changes in air temperature ($MAAT$) as well as differing the snow albedo (α_s) and thus the shortwave radiation input. Considering its significant correlation with glacier mass balance, the impact of the snow albedo on the ice temperature evolution will be addressed in conjunction with the glacier mass balance in section 4.2.2.

The air temperature proved to be of minor importance for the prediction of the thermal state of the glacier, as indicated by linear regression analysis (Tab. 6 &7). The correlation between the air temperature and the maximum CTS depth was relatively low (R^2 = -0.24) (Fig. 13). A similar trend was observed within the modeled subset of Swiss glaciers (Fig. 28) (R^2 = -0.14). At first sight, these findings appear to contradict the fundamental principles of heat conduction outlined in Fourier's Law, which asserts that the heat flux within a medium is directly proportional to the temperature gradient (Cuffey and Paterson 2010). One possible explanation for this outcome could be that lower air temperatures result in a longer preservation of the snowpack, thereby altering the insulation through refreezing meltwater. However, this effect may diminish for very high-elevated glaciers experiencing extremely cold temperatures and minimal snowmelt throughout the year (Haeberli and Funk 1991). The impact of the mean annual air temperature on the glacier's thermal regime needs to thus be interpreted with regard to the snow availability and the presence of meltwater within the snowpack. Following that logic, a combination of minimal snow accumulation and low snow meltwater content would significantly alter the effects of the air temperature on the glacier thermal regime. This applies only to a small number of parameter combinations within this study, which is why the net effect of $MAAT$ on englacial temperatures appears relatively low. However, given a more realistic 3-dimensional setting, snow distribution across glaciers is far from homogeneous, when factoring in avalanches, wind driven snow drift (Kuhn 1995; Farinotti et al. 2010) or largely snow free calving fronts of hanging glaciers. The 1-dimensional setting of IceT might be limited in representing these processes, which are important when understanding the effects of air temperature on the thermal state of glaciers.

4.2.2 Snow & mass balance

Paradoxically, snow specific parameters depicted relatively little correlations with the CTS (Fig. 13). For the total annual snowfall P_s and the snow albedo α_s this finding is most likely an artefact of the systematic exclusion of model runs with substantially positive mass balances. In that way, runs with high albedo only occurred when snowfall was low and vise versa, concealing their effects on the CTS evolution. However, given the notable positive correlations of P_s and α_s with mass balance (as seen in Fig. 13), their impacts can be traced by examining the mass balance trends. Mass balance emerged as the second most crucial predictor among the 7 parameters. Interestingly, it shows bidirectional effects. Regarding the maximum CTS depth, a positive relationship was observed (with R^2 = 0.52 and Coef. = 2.37). This is due to the fact that in some of the scenarios the emergence of a distinct polythermal structure is hindered when surface melt surpasses the CTS propagation rate (Fig. 14). In such a setting, the glacier's thermal evolution is dominated by melt. However, a thresh hold seems to exist where this process reverses and the CTS propagation dominates over the surface melt. In that case the thermal evolution of the glacier is able to adjust to the climatic conditions before the glacier disappears. This process is well recognisable in figure 17. When controlling for surface melt, the situation changes. The annual CTS propagation rate depicted a significant negative correlation with mass balances ($R^2 = -0.9$). According to regression analysis, increasing the mass balance by 1 m (w.e.) results in a reduction of CTS_{prop} by -0.66 m. In other words, a more negative mass balance results in accelerated cooling of the glacier, aligning with various global observations (Irvine-Fynn et al. 2011; Huss and Fischer 2016; Østby et al. 2017). Segmenting the parameter space based on P_s and α_s reveals comparable trends in the CTS evolution to those observed in the mass balance (Fig. (16) & (19)). An increase in the two parameters results in greater maximum CTS depths, while the relation inverts for the CTS propagation.

As compaction is not yet implemented in the model, the evolution of a firn cover could not be integrated. However, it could be proven that an initial firn layer can significantly delay the glacier's cooling. The model indicates that the snow cover timing ($t_{0,s}$) and the number of snowfall days have no significant influence on the three output variables. This may appear counter intuitive, as the temporal overlap of minimal snow cover with cold temperatures would seemingly accelerate cooling, by lowering the buffering effect of meltwater within the snowpack. Nonetheless, the simplified temperature and precipitation models (refer to 2.4) integrated into the model may not comprehensively capture these complex climatic interactions.

4.2.3 Water content (ϕ)

The water volume fraction emerged as the overwhelmingly dominant parameter affecting the glacier's thermal state. The linear model suggests that for each 1% increase in the englacial water content, there was a reduction in the maximum CTS depth by -165.07 m (Fig. 6), and a decrease in the CTS propagation rate by -13.85 m a^{-1} (Fig. 7). Upon closer examination of individual model outputs, there are strong indications pointing towards an exponential relationship between

the water content and the CTS determining output variables, where the effect intensifies as ϕ approaches zero. The linear model might thus not be fully suited to represent this relationship, yet it illustrates it's magnitude. This finding demonstrates the pivotal connection between the ice temperature evolution and the englacial water content. According to fundamental thermodynamic principles, water contained within ice masses acts as a thermal buffer, maintaining the temperature at 0°C during phase transitions owing to the latent heat of fusion (Cuffey and Paterson 2010). Augmenting the water content extends the duration of this buffer. It is thus crucial to identify the spatio-temporal distribution of this 0°C interface in order to comprehend the temporal and spatial variations in ice temperatures. In this study, ϕ was kept constant throughout the entire profile, resulting in a cumulative effect when it was increased. This assumption is based on the limited knowledge available regarding the distribution of englacial water. However, several observations indicate a strong variability in the water content of temperate ice (Raymond and Harrison 1975; Murray et al. 2000; Pettersson et al. 2004; Ogier et al. 2023). These findings, along with this study's results, emphasize the necessity of a better understanding of the spatio-temporal distribution of the water content within glaciers to accurately model their thermal evolution. On the one hand this could be achieved by adding more observational data, which may involve methods such as geophysical surveys utilizing ground-penetrating radar (Murray et al. 2000; Ogier et al. 2023) or surface nuclear magnetic resonance (SNMR) (Hertrich and Walbrecker 2008). On the other hand, a model framework for the intergranular movement of water within temperate ice (Lliboutry 1971; Nye and Frank 1973; Fowler 1984) could be included into englacial temperature models. Granular flow might be modeled by incorporating a Darcy flow implementation, as previously explored within subglacial sediments (Fountain and Walder 1998; Flowers 2015). However, such a model framework requires a more profound knowledge on the variability of ice porosities within these very small alpine glaciers.

The englacial water content remains poorly understood, yet it represents the most crucial parameter in determining the englacial temperature evolution of temperate glaciers.

4.3 The thermal evolution of very small Swiss glaciers

4.3.1 Model comparison

There are certainly some limitations to the comparability of the two model outputs. GERM represents 10 by 10 m grid points, locally calibrated for snow accumulation and melt, whereas IceT was applied on the basis of the average meteorological signal for the entire glacier, limiting calibration to the melt component. Hence, IceT normalizes the ice temperature signal, which would probably have been more negative in the ablation area and less negative in the accumulation area due to variations in snow depth. However, it is unlikely that this normalization fully explains the substantial differences observed in the model output between GERM and IceT. Overall, GERM indicates much lower englacial temperatures, with some of them being four orders of magnitude lower as indicated by IceT. This trend was consistently observed across all 20 modeled glaciers. Reanalysis of

the GERM output from 2016 (Huss and Fischer 2016), revealed that the majority of the very small Swiss glaciers (< 0.5 km^2) are either polythermal or cold by 2014 with 10 m averaged ice temperatures in the ablation area reaching far below -1.5°C. In contrast, within the subset of 20 glaciers modeled with IceT, only a small fraction (3 out of 20) displayed an ice temperature evolution that suggests polythermal conditions by the end of the simulation period. The englacial water content during these comparison runs was set to 0%, similar to the water impermeability assumptions made for GERM. Thus, the differences between the two model outputs needs to be attributed to processes occurring within the snowpack. Applying the enthalpy formulation (Aschwanden et al. 2012), IceT is constantly tracking the mixture of water, air and ice/snow within each of the grid cells. Meltwater drainage only occurs at the uppermost grid cell, as soon as the water content reaches 100%. The remnant melt signal from the previous ablation period is consequently retained within the snowpack. In contrast, GERM assumes complete permeability of the available pore space in the firn, generating runoff at the base of the snowpack that is proportional to the glacier slope. Consequently, the water contained within the snowpack is drained much more rapidly in GERM compared to IceT. As soon as the temperature buffer through meltwater diminishes (see 4.2.3), attenuated cooling within the winter months can occur. In IceT, this situation occurs notably less frequently than in GERM. Studies on the percolation of meltwater through the snowpack have shown that the time delay between the initiation of snowmelt at the surface and the start of run-off at the base of the snowpack are typically in the order of days (Bengtsson 1982). This indicates that IceT is likely overestimating water storage within the snowpack.
Both models make assumptions which do not correspond to reality and thus lead to errors in the computation of englacial temperatures. While GERM most certainly overestimates cooling as it assumes ice impermeability and thus no englacial water content, IceT is probably underestimating cooling due to overestimated water storage within the snowpack.

4.3.2 Spatio-temporal scales of glacier thermal regime transitions

It remains challenging to precisely identify specific locations where transitions from temperate to polythermal conditions are more likely. Reanalysis of the GERM model output, produced by Huss and Fischer 2016, revealed that certain spatial clusters are though detectable. For example west-facing glaciers appeared to be cooler than other orientations and also an increased slope seems to have a negative impact on the englacial temperatures. The most significant differences were found between the different elevation clusters, likely mediated through air temperatures and the low availability of meltwater within the snowpack (see 4.2.1). The model outputs from IceT reveal a concentration of potentially polythermal glaciers in the southern Engadin region (Fig. 24). These glaciers are characterized by minimal winter snowfall while still being exposed to low air temperatures due to their relatively high elevation. This cluster includes Vadret dal Corvatsch, Vadret da l'alp Ota as well as Vadret d'Arlas. Nevertheless, some of the model results also raise questions, as for example the hanging glacier at the Eiger west ridge, or Weisshorn west depicted

relatively low CTS depths. These are very high elevated glaciers, both characterised by steep glacier fronts (Pralong and Funk 2006), which are assumed to be partially cold (Funk and Lüthi 1997). As discussed in section 4.1, IceT's restriction to one dimension and its oversight of two-dimensional variations in snow distribution are insufficient for capturing such features. Nevertheless, Funk and Lüthi 1997, also argue that, despite a mean annual air temperature of -6°C, the greater part of the Eiger hanging glacier is still temperate, owing to the high winter snow accumulation and refreezing rain and meltwater within the snowpack.

Both ice temperature models indicate a relatively rapid transition from temperate to polythermal conditions, occurring within a span of several years (refer to Fig. 25, 26, 27). These transitions are heavily reliant on the snowpack's evolution, especially its persistence throughout the year. Firn is not directly represented as compaction is not yet implemented. However, perennial snow cover usually results in temperate conditions, whereas the absence of snow cover lowers the englacial temperatures. This cooling can be recognised almost instantaneously at shallower depths (3 to 6 m) and typically reaches depths of 10 to 20 m after 2 to 3 years (see 3.2.2). In the practical applications of the two ice temperature models, a water content of zero within the ice column was assumed as no reliable information on the water profile of the modeled glaciers is available. Similar assumptions were made by Gilbert et al. (2018) when modelling Tête Rousse glacier. However, as demonstrated within the parametric study (see (3.1)), the speed of these thermal regime changes relies heavily on the englacial water content (Fig. 14,17,18). A mere reduction of ϕ by 1% could slow down the CTS propagation by 13.85 m a^{-1}. These findings underscore the significance of englacial water in modeling ice temperatures. In order to accurately estimate the spatio-temporal scales of thermal transitions in very small glaciers within the Swiss Alps, a deeper understanding of their englacial water content is indispensable.

5 Conclusion & Outlook

This thesis presented a new enthalpy-based englacial temperature model and further utilized it to investigate the sensitivities of very small glaciers (< 0.5 km^2) in transitioning from temperate to polythermal or cold conditions. 7 parameters were tested, of which 5 have shown to exert a significant influence on the glacier thermal evolution: The mean annual air temperature, the annual snow accumulation, the snow albedo, the initial firn thickness and the englacial water content. The influence of air temperature was partially offset by increased snow accumulation. This impact is believed to be most significant when there is limited availability of meltwater due to very cold temperatures at e.g. high elevations (Haeberli and Funk 1991). Effects of the snow accumulation and snow albedo appeared to be concealed by the systematic exclusion of model runs with positive mass balances. However, their effects could be inferred from glacier mass balance as they both depicted strong positive correlations with it. The model results indicate two distinct effects of mass balance on the evolution of the glacier thermal regime: (1) Under very strong negative mass balances surface melt surpasses the CTS propagation rate and the emergence

of a polythermal structure is hindered. The thermal evolution is thus melt dominated. (2) With less negative mass balances and limited snowfall, the rate of CTS propagation exceeds surface melt, leading the glacier to transition into polythermal conditions characterized by increased CTS depths. The timing of the snow cover appeared to be of minor importance for the prediction of the glacier thermal regime. However, the simplified precipitation and temperature model implemented in IceT might not be able to fully capture complex climatic interactions. The initial firn thickness has shown to delay the transition from temperate to polythermal conditions due to the relatively high storage of meltwater. Ultimately, the englacial water content proved to be the most crucial parameter in predicting ice temperatures. Moreover, this parameter mediates many of the effects implied by the other parameters. A mere increase of the englacial meltwater fraction by 1% reduced the maximum CTS depth by 165.07 m and the annual CTS propagation rate by 13.85 m a^{-1}. This effect appeared to exhibit an inverse exponential trend, being most pronounced as ϕ approaches 0%.

In addition to the sensitivity study, the model was applied to a subset of 20 very small Swiss glaciers (< 0.5 km^2) using the MeteoSwiss dataset utilized by Huss and Fischer (2016). Furthermore, a comprehensive reanalysis of ice temperature model results for all very small Swiss glaciers based on the Glacier Evolution Runoff Model was conducted. Both approaches aimed to identify spatial clusters of very small Swiss glaciers that exhibit a tendency to transition from temperate to polythermal or cold conditions. The GERM data suggests that the majority (>75%) of all very small Swiss glaciers are either polythermal or cold. Spatial clusters of glaciers exhibiting more pronounced cooling than others can be identified for west-facing glaciers as well as higher elevated glaciers. Contrary to this, among the 20 glaciers modeled using IceT, only about 15% (3 out of 20) exhibited an ice temperature distribution implying polythermal conditions by the end of the simulated time span in 2014. The significant differences in the output of the two models likely stem from temporal variations in the water storage within the snowpack. GERM is draining snow meltwater much quicker than IceT, thereby reducing its temperature buffering effect caused by latent heat release during refreezing. The findings indicate that IceT systematically overestimates ice temperatures as a result of this effect. The comparison with borehole measurements has shown that this reduces the model's representativeness. Addressing this issue in future model versions is crucial. This could potentially be achieved by coupling the surface runoff intensity to variables such as glacier slope, similar to the approach in GERM (Huss and Fischer 2016).

The significant influence of englacial water content in predicting ice temperatures, alongside our limited understanding of how it's distributed within very small glaciers, leads to notable uncertainties in the outcomes presented by the model. There are two distinct approaches to address this concern. (1) Firstly, additional observational data can be obtained, which may involve methods such as geophysical surveys utilizing ground-penetrating radar (Murray et al. 2000; Ogier et al. 2023) or surface nuclear magnetic resonance (SNMR) (Hertrich and Walbrecker 2008; Vincent et al. 2012). Alternatively, englacial water content can be directly derived from borehole samples (Murray et al. 2000; Lüthi et al. 2002), or thermodynamic properties (Lüthi et al. 2002). (2) The second approach

involves integrating intergranular water flow into englacial temperature models, treating ice as a porous medium and calculating Darcy velocities based on specified porosities. The enthalpy formulation provides a computational framework for such a model by considering temperate ice as a combination of ice, air, and water. However, additional observational ice temperature data is urgently needed to accurately refine and constrain this model. Such refinement could assist in precisely identifying polythermal glaciers, a crucial factor in glacier hazard assessments due to their increased susceptibility to englacial water storage, which heightens the risk of ice avalanches (Bondesan and Francese 2023) or water pocket outbursts (Vincent et al. 2012).

References

Alean, J. (1985). "Ice Avalanche Activity and Mass Balance of a High-Altitude Hanging Glacier in the Swiss Alps". en. In: *Annals of Glaciology* 6. Publisher: Cambridge University Press, pp. 248–249. ISSN: 0260-3055, 1727-5644. DOI: 10.3189/1985AoG6-1-248-249. URL: https://www.cambridge.org/core/journals/annals-of-glaciology/article/ice-avalanche-activity-and-mass-balance-of-a-highaltitude-hanging-glacier-in-the-swiss-alps/C4E154FCEB902CE8190FEF6B30B298FF (visited on 24/05/2023).

Aschwanden, A. and H. Blatter (2009). "Mathematical modeling and numerical simulation of polythermal glaciers". en. In: *Journal of Geophysical Research: Earth Surface* 114.F1. _eprint: https://onlinelibrary.wiley.com/doi/pdf/10.1029/2008JF001028. ISSN: 2156-2202. DOI: 10.1029/2008JF001028. URL: https://onlinelibrary.wiley.com/doi/abs/10.1029/2008JF001028 (visited on 23/05/2023).

Aschwanden, A. and H. Blatter (2005). "Meltwater production due to strain heating in Storglaciären, Sweden". en. In: *Journal of Geophysical Research: Earth Surface* 110.F4. _eprint: https://onlinelibrary.wiley.com/doi/pdf/10.1029/2005JF000328. ISSN: 2156-2202. DOI: 10.1029/2005JF000328. URL: https://onlinelibrary.wiley.com/doi/abs/10.1029/2005JF000328 (visited on 23/05/2023).

Aschwanden, A. et al. (2012). "An enthalpy formulation for glaciers and ice sheets". en. In: *Journal of Glaciology* 58.209. Publisher: Cambridge University Press, pp. 441–457. ISSN: 0022-1430, 1727-5652. DOI: 10.3189/2012JoG11J088. URL: https://www.cambridge.org/core/journals/journal-of-glaciology/article/an-enthalpy-formulation-for-glaciers-and-ice-sheets/605D2EC3DE03B82F2A8289220E76EB27 (visited on 27/02/2023).

Barry, R. G. and R. J. Chorley (Oct. 2009). *Atmosphere,, Weather and Climate*. en. Google-Books-ID: NxaPAgAAQBAJ. Routledge. ISBN: 978-1-135-26749-0.

Bengtsson, L. (Aug. 1982). "Percolation of meltwater through a snowpack". In: *Cold Regions Science and Technology* 6.1, pp. 73–81. ISSN: 0165-232X. DOI: 10.1016/0165-232X(82)90046-5. URL: https://www.sciencedirect.com/science/article/pii/0165232X82900465 (visited on 21/11/2023).

Benjumea, B. et al. (June 2003). "Estimation of water content in a temperate glacier from radar and seismic sounding data". In: *Annals of Glaciology* 37, pp. 317–324. DOI: 10.3189/172756403781815924.

Benn, D. and D. J. A. Evans (Feb. 2014). *Glaciers and Glaciation, 2nd edition*. en. Google-Books-ID: dkjKAgAAQBAJ. Routledge. ISBN: 978-1-4441-2839-0.

Bondesan, A. and R. G. Francese (June 2023). "The climate-driven disaster of the Marmolada Glacier (Italy)". en. In: *Geomorphology* 431, p. 108687. ISSN: 0169-555X. DOI: 10.1016/j.geomorph.2023.108687. URL: https://www.sciencedirect.com/science/article/pii/S0169555X23001071 (visited on 28/04/2023).

Brownson, J. R. S. (Jan. 2014). "Chapter 06 - Sun-Earth Geometry". en. In: *Solar Energy Conversion Systems*. Ed. by J. R. S. Brownson. Boston: Academic Press, pp. 135–178. ISBN: 978-0-12-397021-3. DOI: 10.1016/B978-0-12-397021-3.00006-5. URL: https://www.sciencedirect.com/science/article/pii/B9780123970213000065 (visited on 16/05/2023).

Bueler, E., J. Brown and C. Lingle (2007). "Exact solutions to the thermomechanically coupled shallow-ice approximation: effective tools for verification". en. In: *Journal of Glaciology* 53.182. Publisher: Cambridge University Press, pp. 499–516. ISSN: 0022-1430, 1727-5652. DOI: 10.3189/002214307783258396. URL: https://www.cambridge.org/core/journals/journal-of-glaciology/article/exact-solutions-to-the-thermomechanically-coupled-shallowice-approximation-effective-tools-for-verification/759FCA0663405388ABE5422BB8CCA5F3 (visited on 22/05/2023).

Crank, J. and P. Nicolson (Jan. 1947). "A practical method for numerical evaluation of solutions of partial differential equations of the heat-conduction type". en. In: *Mathematical Proceedings of the Cambridge Philosophical Society* 43.1. Publisher: Cambridge University Press, pp. 50–67. ISSN: 1469-8064, 0305-0041. DOI: 10.1017/S0305004100023197. URL: https://www.cambridge.org/core/journals/mathematical-proceedings-of-the-cambridge-philosophical-society/article/practical-method-for-numerical-

evaluation-of-solutions-of-partial-differential-equations-of-the-heatconduction-type/B3230893A53384D418228AB39D41A451# (visited on 26/11/2023).

Cuffey, K. M. and W. S. B. Paterson (June 2010). *The Physics of Glaciers*. en. Google-Books-ID: Jca2v1u1EKEC. Academic Press. ISBN: 978-0-08-091912-6.

Faillettaz, J., M. Funk and C. Vincent (2015). "Avalanching glacier instabilities: Review on processes and early warning perspectives". en. In: *Reviews of Geophysics* 53.2. _eprint: https://onlinelibrary.wiley.com/doi/pdf/10.1002/2014RG000466, pp. 203–224. ISSN: 1944-9208. DOI: 10.1002/2014RG000466. URL: https://onlinelibrary.wiley.com/doi/abs/10.1002/2014RG000466 (visited on 03/03/2023).

Farinotti, D. et al. (2010). "Snow accumulation distribution inferred from time-lapse photography and simple modelling". en. In: *Hydrological Processes* 24.15. _eprint: https://onlinelibrary.wiley.com/doi/pdf/10.1002/hyp.7629, pp. 2087–2097. ISSN: 1099-1085. DOI: 10.1002/hyp.7629. URL: https://onlinelibrary.wiley.com/doi/abs/10.1002/hyp.7629 (visited on 19/11/2023).

Farinotti, D. et al. (2012). "Runoff evolution in the Swiss Alps: projections for selected high-alpine catchments based on ENSEMBLES scenarios". en. In: *Hydrological Processes* 26.13. _eprint: https://onlinelibrary.wiley.com/doi/pdf/10.1002/hyp.8276, pp. 1909–1924. ISSN: 1099-1085. DOI: 10.1002/hyp.8276. URL: https://onlinelibrary.wiley.com/doi/abs/10.1002/hyp.8276 (visited on 23/05/2023).

Fischer, M., M. Huss and M. Hoelzle (Mar. 2015). "Surface elevation and mass changes of all Swiss glaciers 19802010". English. In: *The Cryosphere* 9.2. Publisher: Copernicus GmbH, pp. 525–540. ISSN: 1994-0416. DOI: 10.5194/tc-9-525-2015. URL: https://tc.copernicus.org/articles/9/525/2015/tc-9-525-2015.html (visited on 15/11/2023).

Flowers, G. E. (Apr. 2015). "Modelling water flow under glaciers and ice sheets". In: *Proceedings of the Royal Society A: Mathematical, Physical and Engineering Sciences* 471.2176. Publisher: Royal Society, p. 20140907. DOI: 10.1098/rspa.2014.0907. URL: https://royalsocietypublishing.org/doi/10.1098/rspa.2014.0907 (visited on 20/11/2023).

Fountain, A. G. and J. S. Walder (1998). "Water flow through temperate glaciers". en. In: *Reviews of Geophysics* 36.3. _eprint: https://onlinelibrary.wiley.com/doi/pdf/10.1029/97RG03579, pp. 299–328. ISSN: 1944-9208. DOI: 10.1029/97RG03579. URL: https://onlinelibrary.wiley.com/doi/abs/10.1029/97RG03579 (visited on 20/11/2023).

Fowler, A. C. (Mar. 1984). "On the transport of moisture in polythermal glaciers". In: *Geophysical & Astrophysical Fluid Dynamics* 28.2. Publisher: Taylor & Francis _eprint: https://doi.org/10.1080/03091928408222846, pp. 99–140. ISSN: 0309-1929. DOI: 10.1080/03091928408222846. URL: https://doi.org/10.1080/03091928408222846 (visited on 22/11/2023).

Funk, M. and M. Lüthi (May 1997). "Wie stabil ist der Hängegletscher am Eiger?" de. In: *Spektrum der Wissenschaft* 5. Accepted: 2021-06-08T11:50:38Z Publisher: Spektrum der Wissenschaft, pp. 21–24. ISSN: 0170-2971. URL: https://www.research-collection.ethz.ch/handle/20.500.11850/483463 (visited on 22/11/2023).

Gilbert, A. et al. (2015). "Assessment of thermal change in cold avalanching glaciers in relation to climate warming". en. In: *Geophysical Research Letters* 42.15. _eprint: https://onlinelibrary.wiley.com/doi/pdf/10.1002/2015GL064838, pp. 6382–6390. ISSN: 1944-8007. DOI: 10.1002/2015GL064838. URL: https://onlinelibrary.wiley.com/doi/abs/10.1002/2015GL064838 (visited on 14/11/2022).

Gilbert, A. et al. (Nov. 2012). "The influence of snow cover thickness on the thermal regime of Tte Rousse Glacier (Mont Blanc range, 3200 m a.s.l.): Consequences for outburst flood hazards and glacier response to climate change". In: *Journal of Geophysical Research* 117. DOI: 10.1029/2011JF002258.

Gilbert, A. et al. (Sept. 2018). "Mechanisms leading to the 2016 giant twin glacier collapses, Aru Range, Tibet". English. In: *The Cryosphere* 12.9. Publisher: Copernicus GmbH, pp. 2883–2900. ISSN: 1994-0416. DOI: 10.5194/tc-12-2883-2018. URL: https://tc.copernicus.org/articles/12/2883/2018/ (visited on 23/02/2023).

Grab, M. et al. (Dec. 2021). "Ice thickness distribution of all Swiss glaciers based on extended ground-penetrating radar data and glaciological modeling". en. In: *Journal of Glaciology* 67.266. Publisher: Cambridge University Press, pp. 1074–1092. ISSN: 0022-1430, 1727-5652. DOI: 10.1017/jog.2021.55. URL: https://www.cambridge.

org/core/journals/journal-of-glaciology/article/ice-thickness-distribution-of-all-swiss-glaciers-based-on-extended-groundpenetrating-radar-data-and-glaciological-modeling/CB6685222A664FD3FCE1367E2B5245D8 (visited on 19/10/2023).

Gusmeroli, A. et al. (2010). "Vertical distribution of water within the polythermal Storglaciären, Sweden". en. In: *Journal of Geophysical Research: Earth Surface* 115.F4. _eprint: https://onlinelibrary.wiley.com/doi/pdf/10.1029/2009JF001539. ISSN: 2156-2202. DOI: 10.1029/2009JF001539. URL: https://onlinelibrary.wiley.com/doi/abs/10.1029/2009JF001539 (visited on 26/11/2023).

Haeberli, W. and M. Funk (Jan. 1991). "Borehole temperatures at the Colle Gnifetti core-drilling site (Monte Rosa, Swiss Alps)". en. In: *Journal of Glaciology* 37.125. Publisher: Cambridge University Press, pp. 37–46. ISSN: 0022-1430, 1727-5652. DOI: 10.3189/S0022143000042775. URL: https://www.cambridge.org/core/journals/journal-of-glaciology/article/borehole-temperatures-at-the-colle-gnifetti-coredrilling-site-monte-rosa-swiss-alps/BC506384A4516ED10165937DA48908FA (visited on 19/09/2023).

Hager, P. (2002). "Glaziologische Untersuchungen am Gipfelgrat des Vadret dal Corvatsch: Thermik und Oberflächenprozesse". PhD thesis. Geographisches Institut der Universität Zürich, master thesis.

Hertrich, M. and J. Walbrecker (2008). "The potential of surface-NMR to image water in permafrost and glacier ice". In: *Geophysical Research Abstracts*. Vol. 10.

Hock, R. and B. Holmgren (2005). "A distributed surface energy-balance model for complex topography and its application to Storglaciaren, Sweden". English. In: *JOURNAL OF GLACIOLOGY* 51.172. Num Pages: 12 Place: Cambridge Publisher: Cambridge Univ Press Web of Science ID: WOS:000233397200003, pp. 25–36. ISSN: 0022-1430, 1727-5652. DOI: 10.3189/172756505781829566. URL: https://www.webofscience.com/api/gateway?GWVersion=2&SrcAuth=DOISource&SrcApp=WOS&KeyAID=10.3189%2F172756505781829566&DestApp=DOI&SrcAppSID=EUW1ED0C1B7llLf6ycfDvWII1xVfW&SrcJTitle=JOURNAL+OF+GLACIOLOGY&DestDOIRegistrantName=International+Glaciological+Society (visited on 12/10/2023).

Hock, R. (1999). "A distributed temperature-index ice- and snowmelt model including potential direct solar radiation". en. In: *Journal of Glaciology* 45.149. Publisher: Cambridge University Press, pp. 101–111. ISSN: 0022-1430, 1727-5652. DOI: 10.3189/S0022143000003087. URL: https://www.cambridge.org/core/journals/journal-of-glaciology/article/distributed-temperatureindex-ice-and-snowmelt-model-including-potential-direct-solar-radiation/2013F2D6B911401D67EA84728AF93629 (visited on 24/05/2023).

Hori, M. et al. (Feb. 2006). "In-situ measured spectral directional emissivity of snow and ice in the 814 m atmospheric window". In: *Remote Sensing of Environment* 100.4, pp. 486–502. ISSN: 0034-4257. DOI: 10.1016/j.rse.2005.11.001. URL: https://www.sciencedirect.com/science/article/pii/S0034425705003974 (visited on 12/10/2023).

Hoyt, D. V. and C. Fröhlich (Dec. 1990). "Atmospheric transmission at Davos, Switzerland 19091979". en. In: *Climatic Change* 5.1, pp. 61–71. ISSN: 1573-1480. DOI: 10.1007/BF00144680. URL: https://doi.org/10.1007/BF00144680 (visited on 13/10/2023).

Huggel, C. et al. (Dec. 2004). "An assessment procedure for glacial hazards in the Swiss Alps". In: *Canadian Geotechnical Journal* 41.6. Publisher: NRC Research Press, pp. 1068–1083. ISSN: 0008-3674. DOI: 10.1139/t04-053. URL: https://cdnsciencepub.com/doi/10.1139/t04-053 (visited on 22/11/2023).

Hugonnet, R. et al. (Apr. 2021). "Accelerated global glacier mass loss in the early twenty-first century". en. In: *Nature* 592.7856. Number: 7856 Publisher: Nature Publishing Group, pp. 726–731. ISSN: 1476-4687. DOI: 10.1038/s41586-021-03436-z. URL: https://www.nature.com/articles/s41586-021-03436-z (visited on 10/03/2023).

Huss, M. et al. (May 2010). "Future high-mountain hydrology: a new parameterization of glacier retreat". English. In: *Hydrology and Earth System Sciences* 14.5. Publisher: Copernicus GmbH, pp. 815–829. ISSN: 1027-5606. DOI: 10.5194/hess-14-815-2010. URL: https://hess.copernicus.org/articles/14/815/2010/hess-14-815-2010.html (visited on 24/05/2023).

Huss, M. and M. Fischer (2016). “Sensitivity of Very Small Glaciers in the Swiss Alps to Future Climate Change”. In: *Frontiers in Earth Science* 4. ISSN: 2296-6463. URL: https://www.frontiersin.org/articles/10.3389/feart.2016.00034 (visited on 03/03/2023).

Huss, M. et al. (2008). “Modelling runoff from highly glacierized alpine drainage basins in a changing climate”. en. In: *Hydrological Processes* 22.19. _eprint: https://onlinelibrary.wiley.com/doi/pdf/10.1002/hyp.7055, pp. 3888–3902. ISSN: 1099-1085. DOI: 10.1002/hyp.7055. URL: https://onlinelibrary.wiley.com/doi/abs/10.1002/hyp.7055 (visited on 23/05/2023).

Irvine-Fynn, T. D. L. et al. (2011). “Polythermal Glacier Hydrology: A Review”. en. In: *Reviews of Geophysics* 49.4. _eprint: https://onlinelibrary.wiley.com/doi/pdf/10.1029/2010RG000350. ISSN: 1944-9208. DOI: 10.1029/2010RG000350. URL: https://onlinelibrary.wiley.com/doi/abs/10.1029/2010RG000350 (visited on 16/11/2023).

Kääb, A. et al. (Apr. 2021). “Sudden large-volume detachments of low-angle mountain glaciers more frequent than thought?” English. In: *The Cryosphere* 15.4. Publisher: Copernicus GmbH, pp. 1751–1785. ISSN: 1994-0416. DOI: 10.5194/tc-15-1751-2021. URL: https://tc.copernicus.org/articles/15/1751/2021/ (visited on 01/05/2023).

Kavanaugh, J. L. and G. K. C. Clarke (2001). “Abrupt glacier motion and reorganization of basal shear stress following the establishment of a connected drainage system”. en. In: *Journal of Glaciology* 47.158. Publisher: Cambridge University Press, pp. 472–480. ISSN: 0022-1430, 1727-5652. DOI: 10.3189/172756501781831972. URL: https://www.cambridge.org/core/journals/journal-of-glaciology/article/abrupt-glacier-motion-and-reorganization-of-basal-shear-stress-following-the-establishment-of-a-connected-drainage-system/9242E1585C22044DAF3C574C782E0E31 (visited on 01/05/2023).

Klein, G. et al. (Dec. 2016). “Shorter snow cover duration since 1970 in the Swiss Alps due to earlier snowmelt more than to later snow onset”. en. In: *Climatic Change* 139.3, pp. 637–649. ISSN: 1573-1480. DOI: 10.1007/s10584-016-1806-y. URL: https://doi.org/10.1007/s10584-016-1806-y (visited on 09/10/2023).

Konzelmann, T. and A. Ohmura (Jan. 1995). “Radiative fluxes and their impact on the energy balance of the Greenland ice sheet”. en. In: *Journal of Glaciology* 41.139. Publisher: Cambridge University Press, pp. 490–502. ISSN: 0022-1430, 1727-5652. DOI: 10.3189/S0022143000034833. URL: https://www.cambridge.org/core/journals/journal-of-glaciology/article/radiative-fluxes-and-their-impact-on-the-energy-balance-of-the-greenland-ice-sheet/50DB2AE2F1CD2DB9A4273F49924D273F (visited on 13/10/2023).

Kuhn, M. (Jan. 1995). “The mass balance of very small glaciers”. In: *Zeitschrift für Gletscherkunde und Glazialgeologie* 31, pp. 171–179.

Laternser, M. (1992). “Firn Temperaturen in den Schweizer Alpen”. PhD thesis. ETH Zürich, Diploma Thesis. (Visited on 20/11/2023).

Lehning, M. et al. (Nov. 2002). “A physical SNOWPACK model for the Swiss avalanche warning: Part III: meteorological forcing, thin layer formation and evaluation”. In: *Cold Regions Science and Technology* 35.3, pp. 169–184. ISSN: 0165-232X. DOI: 10.1016/S0165-232X(02)00072-1. URL: https://www.sciencedirect.com/science/article/pii/S0165232X02000721 (visited on 16/11/2023).

Linsbauer, A. et al. (2021). “The New Swiss Glacier Inventory SGI2016: From a Topographical to a Glaciological Dataset”. In: *Frontiers in Earth Science* 9. ISSN: 2296-6463. URL: https://www.frontiersin.org/articles/10.3389/feart.2021.704189 (visited on 11/11/2023).

Lliboutry, L. (Jan. 1971). “Permeability, Brine Content and Temperature of Temperate Ice”. en. In: *Journal of Glaciology* 10.58. Publisher: Cambridge University Press, pp. 15–29. ISSN: 0022-1430, 1727-5652. DOI: 10.3189/S002214300001296X. URL: https://www.cambridge.org/core/journals/journal-of-glaciology/article/permeability-brine-content-and-temperature-of-temperate-ice/CDBD694ECD95138E22347EB8CCCC47A7 (visited on 22/11/2023).

Lüthi, M. et al. (Jan. 2002). “Mechanisms of fast flow in Jakobshavn Isbræ, West Greenland: Part III. Measurements of ice deformation, temperature and cross-borehole conductivity in boreholes to the bedrock”. en. In: *Journal of Glaciology* 48.162. Publisher: Cambridge University Press, pp. 369–385. ISSN: 0022-1430, 1727-5652. DOI: 10.

3189/172756502781831322. URL: https://www.cambridge.org/core/journals/journal-of-glaciology/article/mechanisms-of-fast-flow-in-jakobshavn-isbrae-west-greenland-part-iii-measurements-of-ice-deformation-temperature-and-crossborehole-conductivity-in-boreholes-to-the-bedrock/56AA2A50780E776FDFC91622AC8F63E6 (visited on 21/11/2023).

Macheret, Y. Y. and A. F. Glazovsky (Jan. 2000). "Estimation of absolute water content in Spitsbergen glaciers from radar sounding data". en. In: *Polar Research* 19.2. Number: 2, pp. 205–216. ISSN: 1751-8369. DOI: 10.3402/polar.v19i2.6546. URL: https://polarresearch.net/index.php/polar/article/view/2202 (visited on 23/11/2023).

Maussion, F. et al. (May 2022). "The Randolph Glacier Inventory (RGI) version 7". In: Conference Name: EGU General Assembly Conference Abstracts ADS Bibcode: 2022EGUGA..24.4484M, EGU22–4484. DOI: 10.5194/egusphere-egu22-4484. URL: https://ui.adsabs.harvard.edu/abs/2022EGUGA..24.4484M (visited on 22/11/2023).

MeteoSwiss (2014a). *Daily mean temperature: TabsD*. Zürich.

– (2014b). *Daily Precipitation: RhiresD*. Zürich.

– (Oct. 2023). URL: https://www.meteoswiss.admin.ch/climate/the-climate-of-switzerland/radiation-monitoring.html (visited on 16/10/2023).

Moore, J. C. et al. (Jan. 1999). "High-resolution hydrothermal structure of Hansbreen, Spitsbergen, mapped by ground-penetrating radar". en. In: *Journal of Glaciology* 45.151. Publisher: Cambridge University Press, pp. 524–532. ISSN: 0022-1430, 1727-5652. DOI: 10.3189/S0022143000001386. URL: https://www.cambridge.org/core/journals/journal-of-glaciology/article/highresolution-hydrothermal-structure-of-hansbreen-spitsbergen-mapped-by-groundpenetrating-radar/A171CA41FBF56C0EAB046929849E34B1 (visited on 23/11/2023).

Moran, M. J. et al. (Dec. 2010). *Fundamentals of Engineering Thermodynamics*. en. Google-Books-ID: oyt8iW6B4aUC. John Wiley & Sons. ISBN: 978-0-470-49590-2.

Murray, T. et al. (Jan. 2000). "Englacial water distribution in a temperate glacier from surface and borehole radar velocity analysis". en. In: *Journal of Glaciology* 46.154. Publisher: Cambridge University Press, pp. 389–398. ISSN: 0022-1430, 1727-5652. DOI: 10.3189/172756500781833188. URL: https://www.cambridge.org/core/journals/journal-of-glaciology/article/englacial-water-distribution-in-a-temperate-glacier-from-surface-and-borehole-radar-velocity-analysis/49C1E579B840B9CAFD23296F30FBC805 (visited on 20/11/2023).

Nye, F. and F. C. Frank (1973). "HYDROLOGY OF THE INTERGRANULAR VEINS IN A TEMPERATE GLACIER". en. In.

Ogier, C. et al. (Sept. 2023). "Ground penetrating radar in temperate ice: englacial water inclusions as limiting factor for data interpretation". en. In: *Journal of Glaciology*. Publisher: Cambridge University Press, pp. 1–12. ISSN: 0022-1430, 1727-5652. DOI: 10.1017/jog.2023.68. URL: https://www.cambridge.org/core/journals/journal-of-glaciology/article/ground-penetrating-radar-in-temperate-ice-englacial-water-inclusions-as-limiting-factor-for-data-interpretation/F37D1510D3FDDE32490F0ABCD75E254B (visited on 20/11/2023).

Oke, T. (June 2014). *Boundary Layer Climates*. en. Google-Books-ID: vNAangEACAAJ. Routledge. ISBN: 978-0-415-49811-1.

Østby, T. I. et al. (Jan. 2017). "Diagnosing the decline in climatic mass balance of glaciers in Svalbard over 1957–2014". English. In: *The Cryosphere* 11.1. Publisher: Copernicus GmbH, pp. 191–215. ISSN: 1994-0416. DOI: 10.5194/tc-11-191-2017. URL: https://tc.copernicus.org/articles/11/191/2017/ (visited on 16/11/2023).

Paul, F. et al. (2004). "Rapid disintegration of Alpine glaciers observed with satellite data". en. In: *Geophysical Research Letters* 31.21. _eprint: https://onlinelibrary.wiley.com/doi/pdf/10.1029/2004GL020816. ISSN: 1944-8007. DOI: 10.1029/2004GL020816. URL: https://onlinelibrary.wiley.com/doi/abs/10.1029/2004GL020816 (visited on 22/11/2023).

Payne, A. J. et al. (2000). "Results from the EISMINT model intercomparison: the effects of thermomechanical coupling". en. In: *Journal of Glaciology* 46.153. Publisher: Cambridge University Press, pp. 227–238. ISSN: 0022-1430, 1727-

5652. DOI: 10.3189/172756500781832891. URL: https://www.cambridge.org/core/journals/journal-of-glaciology/article/results-from-the-eismint-model-intercomparison-the-effects-of-thermomechanical-coupling/CE37FA73A1E79EA3A320A11C86AE7CC2 (visited on 22/05/2023).

Petrenko, V. F. and R. W. Whitworth (Aug. 1999). *Physics of Ice*. en. Google-Books-ID: oC941a8lXWIC. OUP Oxford. ISBN: 978-0-19-158134-2.

Pettersson, R., P. Jansson and H. Blatter (2004). "Spatial variability in water content at the cold-temperate transition surface of the polythermal Storglaciären, Sweden". en. In: *Journal of Geophysical Research: Earth Surface* 109.F2. _eprint: https://onlinelibrary.wiley.com/doi/pdf/10.1029/2003JF000110. ISSN: 2156-2202. DOI: 10.1029/2003JF000110. URL: https://onlinelibrary.wiley.com/doi/abs/10.1029/2003JF000110 (visited on 02/05/2023).

Pralong, A. and M. Funk (2006). "On the instability of avalanching glaciers". en. In: *Journal of Glaciology* 52.176. Publisher: Cambridge University Press, pp. 31–48. ISSN: 0022-1430, 1727-5652. DOI: 10.3189/172756506781828980. URL: https://www.cambridge.org/core/journals/journal-of-glaciology/article/on-the-instability-of-avalanching-glaciers/CAC101CDF9D5BE5FBF3D5C79526E9502 (visited on 01/05/2023).

Raymond, C. F. and W. D. Harrison (Jan. 1975). "Some Observations on the Behavior of the Liquid and Gas Phases in Temperate Glacier Ice". en. In: *Journal of Glaciology* 14.71. Publisher: Cambridge University Press, pp. 213–233. ISSN: 0022-1430, 1727-5652. DOI: 10.3189/S0022143000021717. URL: https://www.cambridge.org/core/journals/journal-of-glaciology/article/some-observations-on-the-behavior-of-the-liquid-and-gas-phases-in-temperate-glacier-ice/6DF08AAD0B4EC04B2462B3C395E677AC (visited on 20/11/2023).

Raymond, M., M. Wegmann and M. Funk (May 2003). "Inventar gefährlicher Gletscher in der Schweiz". de. In.

Röthlisberger, H. (1981). "Eislawinen u.nd Ausbriiche von Gletscherseen". de. In.

Signer, N. (2014). "Analysis of ice temperatures of four selected very small glaciers in the Swiss Alps by means of modelling and ground penetrating radar". en. In.

Swisstopo (Oct. 2023). Kartenprodukt. URL: geo.admin.ch (visited on 16/10/2023).

Vincent, C. et al. (2012). "Detection of a subglacial lake in Glacier de Tête Rousse (Mont Blanc area, France)". en. In: *Journal of Glaciology* 58.211. Publisher: Cambridge University Press, pp. 866–878. ISSN: 0022-1430, 1727-5652. DOI: 10.3189/2012JoG11J179. URL: https://www.cambridge.org/core/journals/journal-of-glaciology/article/detection-of-a-subglacial-lake-in-glacier-de-tete-rousse-mont-blanc-area-france/9368B303B61028C2E5039574FC61BB22 (visited on 14/11/2022).

Zryd, A. (1991). "Conditions dans la couche basale tempérés: Contraintes, teneur en eau et frottmenet intérieur". PhD Thesis. Ph. D. thesis, Versuchsanst. für Wasserbrau Hydrol. und Glaziol., Eidg. Tech

Declaration of academic integrity

Hereby I declare that I have composed the presented master thesis independently on my own and without any other ressources than the ones indicated. All thoughts taken directly or indirectly from external ressources are properly denoted as such.

Date: 22.12.2023 Signature: